Heat Transfer and Latent Heat Storage in Inorganic Molten Salts for Concentrating Solar Power Plants

Final Report

Report Number: DOE-GO18148

Phase I & 2

Prepared by

Anoop Mathur (Terrafore Inc.)
Rajan Kasetty (Terrafore Inc.)
Prof. Javier Garay (UCR)
Prof. Chris Dames (UCR)
Corey Hardin (UCR)
Mehrnoush Zare (UCR)
Mike McDowell (PWR)
Gyan Hajela (PWR)
Dr. Subbarao Surampudi (JPL)
Dr. Andrew Kindler (JPL)
Dr. Parthasarathy Shakkottai (JPL)
Dr. H. Venkatasetty (Setty Enterprises)

May 14, 2012

Submitted to
U.S. Department Of Energy
Contract: DE-FG36-08GO18148

Contact:
Anoop Mathur
Terrafore, Inc.
100 South 5th St, Suite 1900, Minneapolis, MN 55402
anoop.mathur@terrafore.com

.

Table of Contents

Section 1
Project Executive Summary

Motivation for Research

A major issue preventing the commercial use of Phase Change Material (PCM)-based Thermal Energy Storage (TES) is the difficulty of discharging the latent heat stored in the PCM melt. This is because when heat is extracted, the melt solidifies onto heat exchanger surface decreasing the heat transfer. Thus, to obtain consistently high heat rates salt must be removed continuously from heat exchanger surface to improve the heat transfer coefficient and reduce heat exchanger size to obtain the required high and on-demand heat rates in a solar power plant.

Proposed Technical Innovation

Our innovative approach to solve this problem is to use inorganic salt mixtures that have a *simple* phase diagram and a mixture with a *dilute eutectic* composition[1]. A property of dilute eutectic is that when it freezes, it has an equilibrium liquid associated with it. This solid with the associated liquid has the consistency of *a slurry*, which can be pumped to an external heat exchanger, thus forcing the molten salt over the heat exchanger tubes and causing the freezing solid particles to remain in the molten slurry. The forced convection heat transfer due to flow velocity is significantly larger than conduction through solid. In addition to this, a 'salt-phobic' coating on the heat exchanger surface can further prevent the salt from sticking to the tubes and a nucleating agent and chemical added to the salt mixture that can help with the flow and heat transfer properties.

Objective & Technical Approach

A few of the key tasks conducted for this research included:

- Identify economical salt mixtures for use with CSP plants – Power Towers, Linear Fresnel Reflectors and Parabolic Troughs
- Experiment with several different salt-phobic coating candidates
- Understand the morphology of the freezing dilute eutectic salt consisting of 98% NaNO3 and 2% NaOH. Other salt compositions were studied as well.
- TerrDesign a laboratory scale flow loop experiment using a heat exchanger with coated-tubes with salt flowing on the coated tube side and a coolant inside the tubes.
- Demonstrate
    - Improved heat transfer by using a special salt mixture composition called *dilute eutectic* and by coating heat transfer tubes with material that inhibits sticking.
    - A freezing slurry of salt can be pumped over coated tubes without the salt sticking to the tubes. The goal is to freeze 30% to 40% PCM.

[1] Concept of simple phase diagram and dilute eutectic is explained in Section 3

Expected Benefits

The following benefits are expected from using PCM TES, if at least 40% solidification can be achieved with proposed active heat exchanger concept:

- About 20% reduction in amount of salt and 50% reduction in container size compared to equivalent two-tank sensible heat TES.
- Improved overall CSP system efficiency by 1% to 2%
- Reduced TES costs by 30% over conventional two- tank sensible heat TES resulting in a potential reduction in life cycle cost of electricity (LCOE) costs by about 6%.

Accomplishments

The accomplishments for Phase 1 and Phase 2 projects conducted during 2009, 2010 and 2011, included the following:

- Selected salt mixtures suitable for commonly used steam cycles (6 MPa to 13 MPa steam pressures and steam temperatures to 560 degree Celcius) with various CSP plants
- Identified and characterized two candidate coating technologies for use with heat exchanger.
- Developed an experiment setup for qualifying coatings as 'anti-stick' to selected salt mixture. In the experiment rig the salt mixture is pumped through an external heat exchanger with partial frozen salt slurry returning to tank.
- Developed a mathematical model of the PCM storage system and integrated with power tower CSP plant simulation model
- Designed a shell and heat exchanger with coated tubes and integrated it with molten salt flow loop experiment setup. The laboratory prototype used 12000 lbs of dilute eutectic NaNO3-NaOH salt mixture with a storage capacity of about 150 kWh(t) to deliver heat rate up to 30 kWt
- Demonstrated 15% solidification with actively pumping freezing salt over the coated heat exchanger tubes.
- Conducted tests by pumping salt over a coated heat exchanger and collected data to quantify heat transfer coefficient. The results compared well with the model.
- Estimated heat transfer coefficient of 600 W/m2-K with active pumping of freezing salt.

Key Findings

- Dilute eutectic (hyper-eutectic) mixtures of inorganic salts that form a simple eutectic phase diagram exhibit slurry like properties. This property can be taken advantage of to pump salt mixtures over coated heat exchanger tubes and improve heat transfer when PCM is used for storing thermal energy
- Successfully pumped a dilute eutectic molten salt mixture near its freezing point over the specially coated heat exchanger tubes and achieved partial solidification demonstrating use of latent heat of fusion while increasing the heat transfer coefficient. The heat transfer coefficient increased by ten-fold over a passive PCM-TES. However, the solidification achieved was only 15% which is lower than the project milestone of 40%.
- Simulations show that the PCM-TES system can improve the overall system efficiency of the CSP plant by 0.8%, thus requiring about 8% less storage for same capacity factor. This is because for a short period of time, the receiver can be operated to collect energy at lower

temperature to melt the salt, which reduces radiation losses from the solar receiver and increases the collection efficiency. This in turn also allows useful energy to be collected during periods of low insolation by running the receiver at lower temperatures.

- With the use of only 15% latent heat in PCM salt, the net specific cost of PCM-TES using the active heat exchanger described in this document is projected to be only 9% when compared to a two-tank conventional sensible storage system. If credit is taken for the improvement in the overall system efficiency, then these savings increase to 17%. The project goal for cost reduction was 30%.
- Even though, these savings are after paying for the added cost of coated tube heat exchanger, there is uncertainty in our estimate of the cost of the parasitic energy for pumping. In addition, since we are pumping molten salt at freezing point, we expect significant issues with designing and operating with heat tracing system to prevent freezing inside piping. Any incident with freeze-up during operation will reduce the savings.
- Significant lessons were learnt when pumping salt mixtures near freezing temperatures through pipe fittings, valves, bends, and pumps. Heat tracing, location and prevention of solidification and high pressures in unwanted areas require special engineering design and care. The failure mode effect analysis, the experienced gained and the designs developed can be used for any sensible or latent heat system where high temperature molten salt is pumped.

Project Team

US Department of Energy Project Officers – Brian Hunter, Joe Stekli, Tommy Rueckert
Terrafore Inc., MN (Lead)
University of California at Riverside, CA (UCR)
Pratt & Whitney Rocketdyne, CA (PWR)
Jet Propulsion Labs, CA (JPL)
H.V. Setty Enterprises, MN

Report

The report documents the specialty coatings, the composition and morphology of hypereutectic salt mixtures and the results from the experiment conducted with the active heat exchanger along with the lessons learnt during experimentation.

Section 2
Background and Introduction

A key technological issue facing the success of future Concentrating Solar Thermal Power (CSP) plants is creating an economical Thermal Energy Storage (TES) system. Current TES systems use either sensible heat in fluids such as oil, or molten salts, or use thermal stratification in a dual-media consisting of a solid and a heat-transfer fluid. However, utilizing the heat of fusion in inorganic molten salt mixtures in addition to sensible heat , as in a PCM-based TES, can significantly increase the energy density of storage (by about 45%) requiring less salt and smaller containers.

A major issue that is preventing the commercial use of PCM-based TES is that it is difficult to discharge the latent heat stored in the PCM melt. This is because when heat is extracted, the melt solidifies onto the heat exchanger surface decreasing the heat transfer. Even a few millimeters of thickness of solid material on heat transfer surface results in a large drop in heat transfer due to the low thermal conductivity of solid PCM. Thus, to maintain the desired heat rate, the heat exchange area must be large which increases cost. Another issue is finding low cost salt mixtures with good thermal properties and high heat of fusion.

Our innovative approach to solve this is to use inorganic salt mixtures that have a *simple phase diagram* and the mixture is a *dilute eutectic composition*. These two new terms – *dilute eutectic and simple phase diagram* – are explained later. A property of dilute eutectic is that when it freezes, it has an equilibrium liquid associated with it. This solid with the associated liquid has the consistency of a slurry, which can be pumped to an external heat exchanger, thus forcing the molten salt over the coated heat exchanger tubes and causing the freezing solid particles to remain in the molten slurry. The forced convection heat transfer due to flow velocity is significantly larger than conduction through solid. In addition to this, *a 'salt-phobic' coating* on the heat exchanger surface can cause the salt to adhere to the tubes lightly, so that it can be easily removed by the flowing salt.

Thus, two key considerations for designing a successful PCM storage system would be:

- Selecting a storage media in the approximate temperature range of 275 C to 350 C with the following desired properties :
    - High energy density. This requires less TES material and hence smaller tanks, lower cost, and lower thermal loss during storage.
    - High chemical and thermal cycling stability
    - Complete reversibility for a large number of charge and discharge cycles
    - Low specific cost
    - Readily available and easy to handle with low toxicity and low corrosivity
- Designing a heat exchange mechanism that minimizes the cost of the heat exchanger. To discharge heat from a PCM-based TES, a good heat exchanger should have the following properties:
    - have a high heat transfer coefficient throughout the discharge
    - use low parasitic power for pumping, if using an active heat exchanger
    - use common heat exchanger designs, such as shell and tube, that can be manufactured using state-of-the-art techniques

In the following sections we describe a baseline CSP plant, prior art in designing active heat exchangers for PCM-TES and our approach of a shell and coated tube heat exchanger.

Baseline CSP Plant with PCM-TES

Te

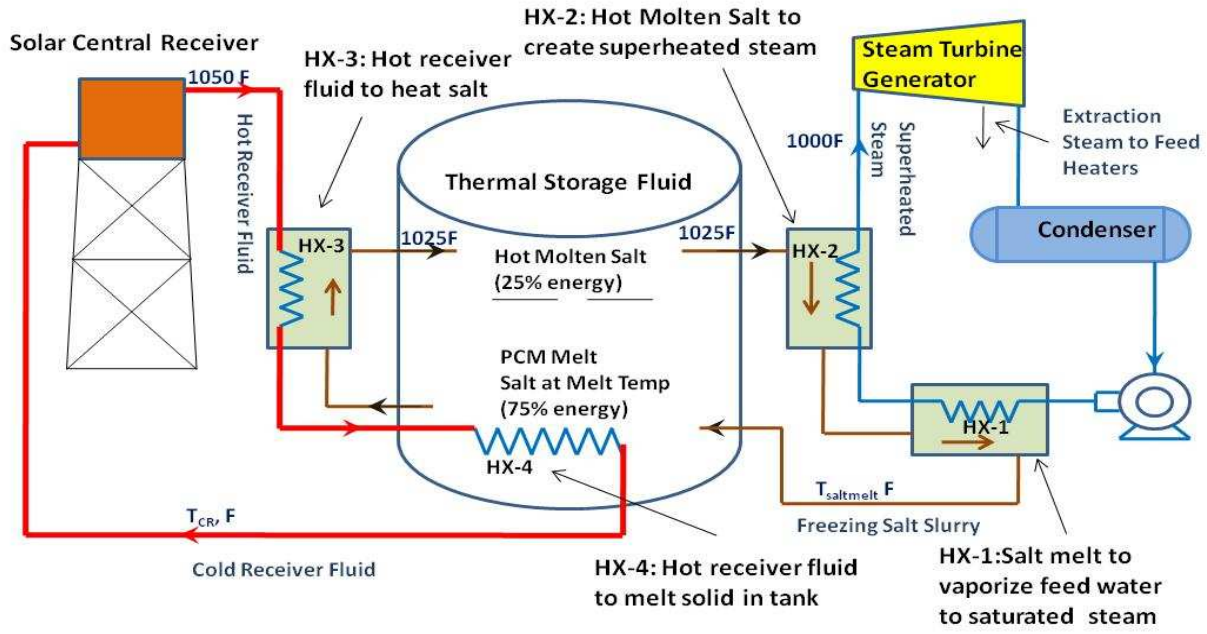

Figure 1.1. PCM-based TES design offers a low cost approach by reducing the TES system size by 37% to 56%

A baseline system using power tower is shown in Figure 1.1. This figure shows a PCM-based TES system with a single tank, in a power-tower configuration. In this configuration, thermal energy is stored as a combination of latent heat and sensible heat in an inorganic molten salt mixture. In the figure, the fluid at the bottom of the tank labeled- *PCM Melt*– stores up to 75% of the total heat at a constant melt temperature of 310^{o}C (590 F) as heat of fusion in an inorganic salt mixture consisting of a large percentage by weight of sodium nitrate and a small amount of sodium hydroxide (this proprietary composition is described later as the *dilute eutectic*). The fluid labeled – *Hot Molten Salt* – stores the remainder 30% of heat as sensible heat in salt temperatures between the melt temperature and up to 565^{o}C (1025 F). The ratio of latent heat stored to sensible heat depends on the latent heat of fusion of selected salt mixture and the high and the low operating temperatures (the low operating temperature is typically the melting point of the salt.)

Starting from the right of the tank in Figure 1, high pressure 8.6 MPa (1250 psia) feed water from the condenser is vaporized into a saturated steam at 300^{o}C in a steam generator heat exchanger *HX*-1. Superheat is added to the saturated steam in the superheat heat exchanger *HX-2*. This superheated steam at 540^{o}C (1000 F) is delivered to the Steam Turbine Generator. The heat for superheating steam and vaporizing feed water is provided by pumping the hot molten salt from top of tank, first to *HX-2* and then to *HX-1* as shown in the figure. The salt is cooled to the freezing or melting point of salt in HX-1 causing some salt to solidify. The partially-frozen salt-slurry from *HX-1* is returned to the tank.

On the left of the tank in Figure 1, the hot receiver fluid from the Solar Central Receiver (power tower) transfers heat to the molten salt in the tank in a heat exchanger labeled *HX-3*. Then the fluid is directed to the heat exchangers labeled *HX-4* to melt the salt in the tank. The cold receiver fluid from *HX-4* is returned to the Solar Central Receiver to collect solar heat. (The return temperature of the cold receiver fluid is at 315^{o}C (600 F) slightly higher than the melt temperature of 310^{o}C . The heat transfer fluid (HTF) in the receiver can be any advanced heat transfer fluid such as another thermally-stable molten salt mixture or liquid sodium or oil.

In state-of-the-art CSP systems which use a two-tank sensible TES, the HTF is same as the storage fluid and since large volumes of this fluid are required, the HTF selected must be economical. However, with PCM-TES shown, an HTF can be chosen independent of the TES storage salt. Since the fluid required to collect energy in the receiver fluid is independent of TES salt, an efficient HTF which can operate at higher temperatures can be selected. For example, if this temperature can be increased to 600^{o}C (1110F), then the hot molten salt temperature in the TES tank can be raised to 580^{o}C (1075F) instead of the 1025F and the steam delivered to turbine can be raised to a higher temperature which will increase the heat to electrical conversion efficiency in the turbine generator.

Designing an Active Heat Exchanger

There are many types of heat exchangers used in the industry for transferring heat during phase change from liquid to solid. Some of the active (not passive) heat exchange designs include shell and coated tubes; others use mechanical scrapers, ultrasonic vibrations or flexing to free the tubes of freezing salts. Other active heat exchanger designs include microencapsulating the salt and pumping it by carrier fluid or by simply having water in direct contact with the molten salt to generate steam. Some of these designs were built and tested for PCM-TES systems in the early 1980s. However, the research was incomplete due to change in US DOE energy focus in 1981.

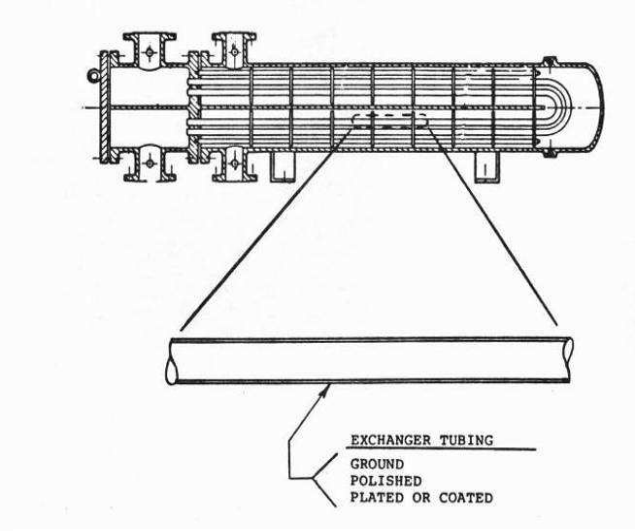

Figure 2.Low adhesion surfaces and shell and tube heat exchangers offer economical design options

Our preliminary analysis and experience, based on this past research, indicated that a shell and tube type of heat exchangers, with the salt on the shell side and the two-phase steam water inside the tube (Figure 1.2), can potentially be successful when discharging heat from the PCM melt. Furthermore, since this is a commonly used design in the industry it is also the most economical to use.

Our baseline approach was to simulate and test various configurations of the shell-and-tube exchanger and by coating the tubes with a material to render it smooth to prevent freezing PCM solids from adhering to it during heat transfer through the tube surface.

Research on Additives and Coatings

A major drawback of using phase change molten salt materials is their poor thermal conductivity and the fact that clumping occurs during freezing that sticks to the walls of the storage tank and heat exchanger surfaces. Using our proposed storage media of dilute eutectic would alleviate this problem. To further improve the flow properties and improve the conductivity, we proposed to investigate use of additives such as graphite, nano-carbonaceous materials, and ionic liquids. Since coatings also alleviate the problem of the phase change materials sticking to the walls, we proposed to investigate heat exchanger coating materials such as graphite, metallic nitrides and carbides, and high temperature polymers (such as imides, poly benzo-oxy imidazole). We propose these materials because of their high thermal stability, and chemical stability, good heat transfer properties and good non-wetting characteristics with molten salts.

Research Tasks

The research conducted over the two years included the following and is discussed in sections listed below:

- Selecting a salt mixture for use with various CSP designs (Section 3)
- Conducting research to select a salt-phobic coating for the selected salt mixture (a dilute eutectic of sodium nitrate and sodium hydroxide) (Section 4)
- Characterizing the morphology of dilute eutectic mixture (Section 5)
- Designing a heat exchanger and PCM-TES laboratory prototype(Section 6)
- Conducting experiments by pumping freezing salt mixture using the heat exchanger (Section 7)
- Model and economic analysis (Section 8)
- Lessons learned from the research (Section 9).

Section 3
Selecting Salt Mixtures for Latent Heat Thermal Energy Storage for Concentrating Solar Power Plant (CSP)

Focus of this Section

This section discusses the selection of salt mixtures for storing thermal energy as latent heat of fusion in mixtures of inorganic salts that melt in the range of 275 ^{o}C to 350 ^{o}C.

This melting temperature range is chosen to match the steam vaporization temperatures that are typically used in power generation cycles using Rankine Turbines. The concentrating solar thermal power (CSTP or CSP) plants are being designed to heat fluid from 400 ^{o}C to 565 ^{o}C to provide heat for vaporizing and superheating steam at steam pressure from 5.9 MPa (850 psia, saturated steam temperature of 274 ^{o}C) to 12.4 Mpa (1800 psia , saturated steam temperature of 327 ^{o}C). The salt melting point should be a little higher than the selected saturated steam temperature. Future systems can go up in steam pressures to 16.5 MPa (2400 psia, 350 ^{o}C saturated steam temperature) or even supercritical range (>22.1MPa or >3207 psia).

Melting Point of Salts Required for CSP

The melting point of salt should be higher than the vaporization temperature of steam at the selected steam conditions for the Rankine power cycle. The temperature difference is determined by the optimum approach temperature for heat transfer from freezing salt to boil steam. Typically this is between 15 C to 25 C depending on the cost of the coated tube boiler (heat exchanger).

The following Table 2.1 gives the required melting points of salts for Concentrating Solar Thermal Power (CSP) systems which include: Solar Central Receiver (Power Tower), Parabolic Trough, and Linear Fresnel Reflectors. For utility scale power generation generating electrical power between 50 MW(e) to 100 MW(e), these use Rankine steam turbines. The steam pressures and temperatures to these turbine range from 5.9 MPa to 22.1 MPa with superheated steam of 400 ^{o}C to 565 ^{o}C. Table 1 shows the typical steam conditions for the various CSP technologies. A large of the heat is required to vaporize steam at constant saturated steam temperature shown in the table. Thus for generating power through storage, a large fraction of heat must be stored above the saturation steam temperatures (for example at 8.6 MPa and 565 ^{o}C turbine conditions, the heat of vaporization at 300 ^{o}C is 70% and the sensible heat between saturated temperature of 300C and superheated temperature of 565 ^{o}C is 30%). The desired salt melting temperature should be 5 C to 10 C higher than the saturated steam temperature, as shown in Table-1. Next generation power tower systems are expected to use supercritical pressures of 22.1 MPa. The higher pressure steam turbine cycles are more efficient and will significantly improve the overall plant efficiency and hence the economics. Therefore, in this report we considered salts for steam cycles up to 16.5 MPa.

Table 1 Salt Melting Temperatures Required for Various Power Plant Cycles

CSP Technology vs. Steam Conditions	Next generation Power Tower CSP					
	Next generation Troughs & Fresnel CSP					
	SOA Power Tower CSP					
	SOA Fresnel CSP					
	SOA Parabolic Trough CSP					
Steam Pressure, MPa (psia)	5.9 (850)	8.6 (1250)	10.0 (1450)	12.4 (1800)	16.5 (2400)	22.1 (3200)
Saturated Steam Temperature, deg C (deg F)	274 (527)	300 (572)	311 (599)	327 (617)	350 (662)	373 (705)
Desired Salt Melting Point, deg C (deg F)	285 (545)	310 (590)	320 (608)	340 (644)	360 (680)	400 (752)

Concept of *Simple Phase Diagram and Dilute Eutectic*

In a *dilute eutectic* mixture 96% to 98% by weight is of the major component of the salt mixture and remainder is a selected minor component salt mixture. The salts in Table 3 can be used as a major component in combination with a salt that can form a eutectic with a minor component (2% to 4% of the mixture weight). For example, there are 29 different salt systems with NaOH, 123 salt systems with KNO3, 117 salt systems with NaNO3 and so on. Our approach requires us to select the minor component that forms a *simple phase diagram* or no solid solutions as the mixture solidifies. This is because we require the solid that crystallizes out during solidification should be in equilibrium with a liquid. In the phase diagram, shown in Figure 3 and discussed below this is the region between the melting point of major component and the eutectic point of the mixture.

An example of a simple phase diagram and dilute eutectic composition is described below using a NaNO3-NaOH system.

Figure 1 shows a *simple phase diagram* of a NaNO3-NaOH system. In a *simple phase diagram* there are no solid solutions as is shown on the right or the NaNO3 side of the figure. The eutectic composition is 83.2% NaNO3 and 16.8% NaOH and eutectic temperature is 246 ^{o}C. The selected composition of 97% NaNO3 and 3% NaOH for TES has much larger percentage of NaNO3 than the eutectic composition and hence the term *dilute eutectic composition* in NaNO3. The storage temperature at the start of a discharge cycle is closer to the melting point of NaNO3 which is 310 ^{o}C. As heat is extracted, only NaNO3 component crystallizes out (since there are no solid solutions on this side) leaving an equilibrium liquid composition along the liquidus curve.

For example, for the selected dilute eutectic after 50% of the NaNO3 freezes out, the equilibrium liquid will contain 47 units of NaNO3 and the original 3 unit of NaOH. This calculates to a liquidus of 94%

NaNO3 and 6% of NaOH. From the curve we can see that the freezing temperature for 94% NaNO3 and 6% NaOH is 305 ^{o}C. Thus, after 50% of heat is removed from the melt, the temperature only drops from the initial 310 ^{o}C to 305 ^{o}C, which is not a significant drop in temperature while the latent heat is stored at near constant temperature. This is the reason to use a dilute eutectic as a starting mixture. We must ensure that the heat exchanger tube temperature is kept above the eutectic temperature of 246 ^{o}C so that the solid on the tubes has a liquid in equilibrium with it. To ensure this we require that the salt system should not have any solid solutions between its initial melting temperature and eutectic point.

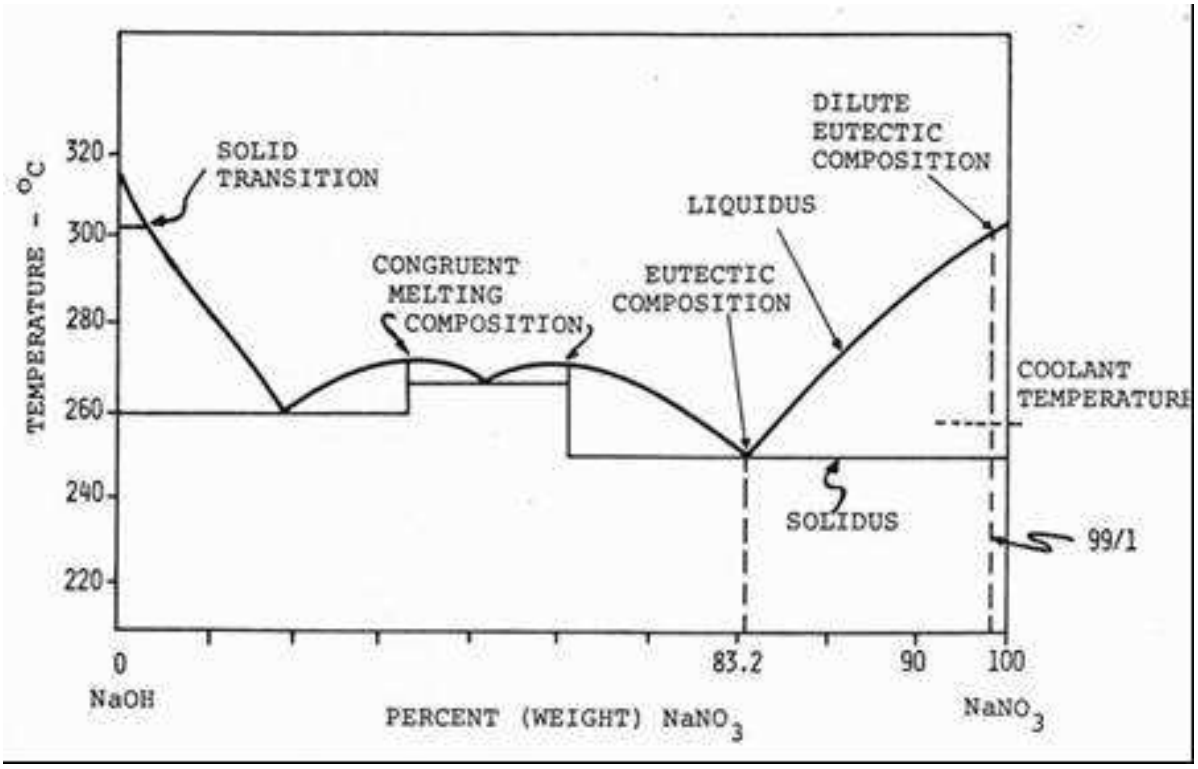

Figure 1: Phase Diagram of NaNO3-NaOH system

There are numerous salts and salt mixtures that have melting points within the range of the CSP application. In addition to melting point and low cost per unit weight the selected salt must have several desirable properties. Figure 2.1 shows a process for selecting salts.

Ideally the selected salt must:

- be easily available
  be thermally stable and withstand multiple freeze-thaw (>5000) cycles
- have high specific heat of fusion (kJ per kg and kJ per m^3),
- should be less corrosive to commonly used containers (eg, steels). Since the salts will be of commercial grade, the levels of impurities, particularly such as chloride and moisture are important as they affect corrosion to container materials
- have a low vapor pressure at temperature (up to 550 ^{o}C),
- be non-hygroscopic, reactive or non-toxic so it can be handled and stored easily,
- has good thermal properties such as thermal conductivity.

Most salts are hygroscopic and in addition to impurities, moisture should be avoided as they affect the corrosion properties as well as heat of fusion of salts (3). During thermal cycling process, there will be interactions between the molten eutectic mixture and the surface of the container, and the resulting impurity is likely to increase and however small amount it may be, compared to the eutectic mixture, and likely to affect the rate of nucleation and crystallization during phase-change.

Appendix 2.1 lists all the salt mixtures that have been studied and have melting points within the range of 275 ^{o}C to 375 ^{o}C. We first screen salt mixtures from the list in Appendix A by using the criteria in Table 2 which is a qualitative evaluation of inorganic salt mixtures by category. In the Terrafore concept for thermal storage, the salt mixture is a 'dilute eutectic' salt mixture consisting of a major component (which is typically much greater than the composition at the eutectic) in the salt mixture and a minor component, which is the remainder. The 'yes' in Table 2.2 indicates the salt is acceptable and 'no' indicates it is not acceptable. Some salts which may not be acceptable as major component may qualify for use as a minor component.

Based on this, salts containing chlorides, nitrates and hydroxides may be selected as a major component. Next, salts that contain exotic or uncommon metals are rejected. For example, salts containing noble metals such gold, silver, platinum, tungsten, cadmium etc are expensive, and are not readily available in very large quantities. These are not selected even as minor components. Since Lithium salts have very high heat of fusion, we kept this in the short list in Table 2.3, which lists the major component of the salt mixture suitable for CSP applications. This (Table 3) is a short list of thirty one salts and salt mixtures that have melting points within the 275 ^{o}C to 375 ^{o}C range, have many desired properties such as thermal stability and availability for use in TES applications. The rightmost column in the table shows the steam cycle for which the salt can be used. Salts such as NaNO3, NaOH, KNO3 and KOH are highlighted as selected major component. Next we use the simple phase diagram criteria (discussed later) with any of these four major components. When alternative salt mixtures that have simple eutectic diagram are available within the steam cycle, we reject salt mixtures that contain component(s) that are either corrosive or are expensive. For example, the fluorides or the chromate or zinc chloride in the Table 2.2 even in small quantities can be problematic. If there is an alternative to any of these we select that salt mixture as the major component

Table 2. Various categories of salts and their characteristics

Salt Category	Qualitative Characteristic of Salt	Major Component	Minor Component
Chlorides	Low cost, good thermal properties, readily available in large quantities. Corrosion is an issue and must be addressed (*)	Yes	Yes
Hydroxides	same as above	Yes (?)	Yes
Nitrates	same as above	Yes	Yes
Nitrites	same as above but oxidizes easily, low vapor pressure, not very stable	No	Maybe
Carbonates	applicable temperature range high; good additives	No	Yes
Sulfates	Corrosive	No	Yes
Oxides	Corrosive	No	No
Fluorides	Fluorides not available in large quantities. Most Flouride salts that melt below desired temperature range contain expensive Li or alkali metal	No	Yes

(*) Chlorides, sulfates, phosphates are present in smaller quantities in most salts obtained in bulk and corrosion has to be addressed in selecting any salt mixture.

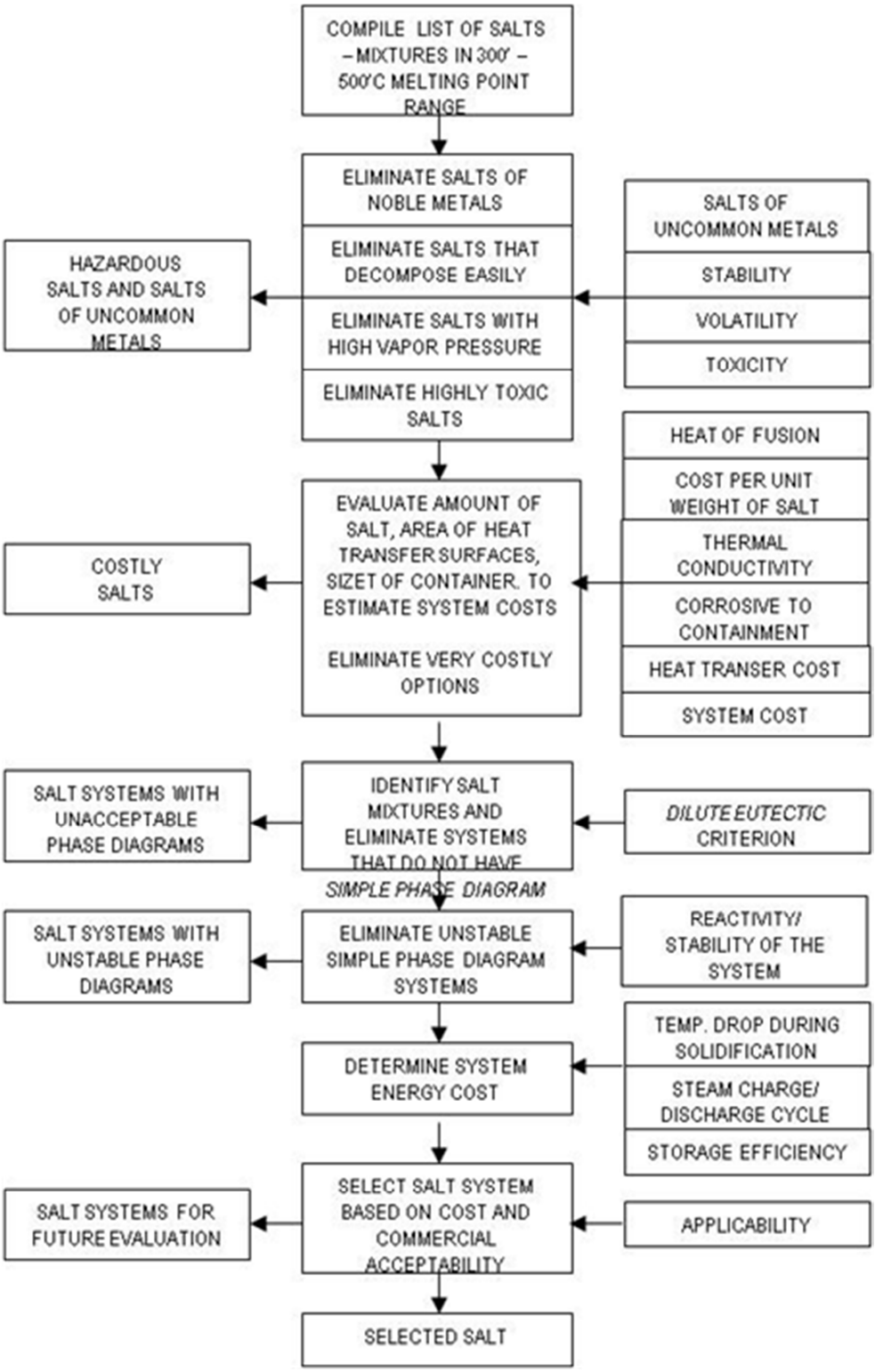

Figure 2. Method for Selecting Salt Mixtures for CSP Application

Table 3. Candidate Salt & Salt Mixtures for use with CSP- TES as a Major Component

	System	Eutectic Temp, deg C	Composition (mole percent)	Formula Wt	kJ/kg	Steam Cycle
1	NaNO3-NaCl-Na2SO4	278 C	86.3-8.4-5.3	85.79	190.22	1
2	LiCl-LiOH-KCl	280 C	45-43.5-11.5	27.66	763.33	1
3	NaNO3-NaCl-Ba(NO3)2	280 C	86.2 -7.9-5.8	93.02	175.90	1
4	NaNO3-NaCl	281 C	98.9-1.1	84.71	175.59	1
5	NaOH-NaCl-Na2CO3	282 C	85.8-7.8-6.4	45.66	206.62	1
6	ZnCl2 (**)	283 C	100	136.00	75.37	1
7	NaOH-Na2CO3	283 C	92.8-7.2	45.42	199.95	1
8	NaOH-NaCl-Na2CO3	291 C	87.3-6-6.6	45.42	199.95	1
9	NaNO3-NaBr (**)	293 C	90.5-9.5	86.71	182.32	1
10	NaOH-Na2SO4	293 C	95.3-4.7	44.79	160.19	1
11	NaNO3-Ba(NO3)2 (**)	294 C	93.6-6.4	96.26	159.89	1
12	KCl-ZnSO4 (**)	295 C	66.6-33.4	103.46	203.86	1
13	NaNO3-NaCl	297 C	93.5-6.5	83.27	187.22	1
14	KNO3-KF	298 C	91-9	97.13	135.93	1
15	NaNO3 - NaCl	298 C	95-5	83.67	183.95	1
16	NaNO3-Na2SO4	300 C	95.5-4.5	87.57	172.81	1
17	NaNO3-NaF	304 C	96.5-3.5	83.50	184.30	1
18	NaNO3	310 C	100	85.00	173.27	1,2
19	NaOH - NaCl	314 C	93.7 -6.3	41.16	187.62	2
20	NaOH	318 C	100	40.00	158.99	2,3
	Salt System	Deg C	Mole%	Formula Wt	kJ/kg	Cycle

21	KNO3-Ca(NO3)2-K2CRO4 (**)	319 C	99.18-0.12-0.70	100.37	118.59	2,3
22	KNO3 - KCl	320 C	94-6	99.42	126.78	2,3
23	Na2CO3-Na2SO4	330 C	66.5-33.5	56.00	474.81	3
24	KNO3-K2SO4	334 C	98.8-1.2	99.79	120.55	3
25	KNO3 – KBr (**)	336 C	99-1	101.18	117.15	3
26	KNO3	337 C	100	101.00	115.99	3
27	LiCl-KCl-LiF	346 C	56-40.5-3.5	56.16	408.93	4
28	LiCl-KCl-NaCl	346 C	55-36-9	55.43	415.33	4
29	LiCl-KCl	348 C	58-42	55.92	405.77	4
30	LiOH-K2CO3-Li2CO3	350 C	59.1-28.2-12.7	48.31	534.76	4
31	KOH	360 C	100	56.00	167.36	5
Notes	Steam Cycle: 1=5.9 MPa, 2=8.8 MPa, 3=10.0 MPa, 4= 12.4 MPa, 5=16.5 MPa ** Avoid if alternate salts are available. Bromides and chromates are toxic and for large scale systems cannot be used even in small quantities. Lithium salts are included because of their high heat of fusion. Lithium salts are expensive and hygroscopic and require special handling. LiNO3 is perhaps the only exception that may be used in small quantities. Thus from practical standpoint there are very few salts that qualify for use as PCM for TES application.					

Recommended Salts for CSP Applications

We studied phase diagrams for several mixtures with the salts listed in Table 3 and used a combination of criteria discussed earlier (see Figure 2) in the salt selection method such as the simple phase diagram, low cost, low corrosivity, high heat fusion, availability, and experience. Based on this, we selected the salts listed in Table 5 as recommended salt mixtures for the different steam cycles. The percentage by weight of the major component is much higher than that of the composition of this component at the eutectic point. In case of three salt mixtures, the minor component may be a eutectic of two components and the major component is the third salt. Alternatively, the major component may be a eutectic of two components (example, NaNO3-NaCl in the table) and the minor is the third component.

Nitrate salts have been used extensively in the industry and are readily available in large quantities. Stainless steel is preferred as containment material. Even though mild steel can be used, the incremental cost of stainless steel over mild steel relative to the overall cost of system is small and stainless steel has better corrosion resistance to most salts and impurities. The impurities alter the system properties and the

corrosion properties of the mixture. An assay and thorough analysis of the effect of these impurities is required before specifying and procuring salt mixtures.

For experiments in Phase 2 and Phase 3 of the program we selected a *dilute eutectic* mixture of NaNO3 as the major component and NaOH as the minor component.

Table 4. Selected Salts for Typical Steam Power Plant Cycles

Major Component (Initial Melting Point)	Minor Component	Steam Pressure for CSP / Rankine cycle
NaNO3-NaCl eutectic (294 C)	NaOH	5.9 MPa
NaNO3 (310 C)	NaOH	8.8 MPa
NaOH (318 C)	NaNO3	10 MPa
KNO3 (337 C)	KOH	12.4 MPa
KOH (360 C)	KNO3	16.5 MPa

Section 4
Characterization of Anti-stick Coating using Differential Scanning Calorimeter

Differential scanning calorimeter (DSC) measurements were used to examine the effects of 1)composition, 2) surface roughness, and 3) coating layer, on the solidification temperature of the salts. The cooling rate was also varied (10, 50, 100^{o}C/min). A TA instruments DSC was used in this study.

Effects of salt composition

In order to examine the dependence of the melting and solidification events on of salt composition, different compositions of salt (NaOH/NaNO3) ratios were weighed and mixed for DSC analysis. The salts were transferred to as-received stainless steel DSC pans. In the course of our experiments, the solid salts were heated from room temperature to 350°C and subsequently cooled and repeated; each run comprised 10 different heating-cooling cycles. Figure 1 has the DSC results showing the heat flow vs. temperature for varying compositions of salt. The downward trend of the curve corresponds to the salt melting and the upward trend (peak) corresponds to the solidification event. The results demonstrate that both the melting and solidification temperatures are composition dependent. We also see that for some compositions the curves (different heating-cooling cycles) do not overlap. This is an indication of the lack of repeatability of the melting/cooling. The only composition for which the curves overlap is the 100% NaNO3 sample.

We attribute the lack of repeatability of the samples containing NaOH to corrosion of the stainless steel by NaOH. Corrosion changes the SS surface and also the global composition of the salts and thus the solidification/melting temperatures. These findings show that identifying a coating that minimizes corrosion is crucial.

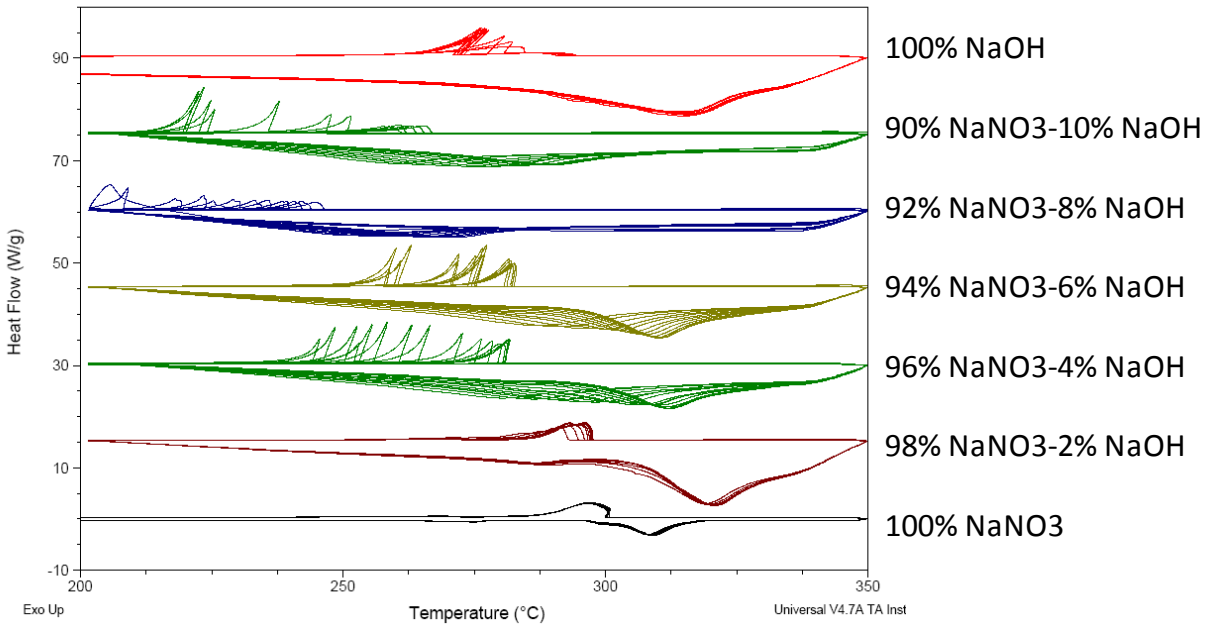

Effects of surface roughness

In order to examine the effects of surface roughness on the solidification event, we systematically varied the surface roughness of the DSC pans by electro-polishing. Figure 2 a and 2 b are pictures of the surface of DSC pans before and after polishing.

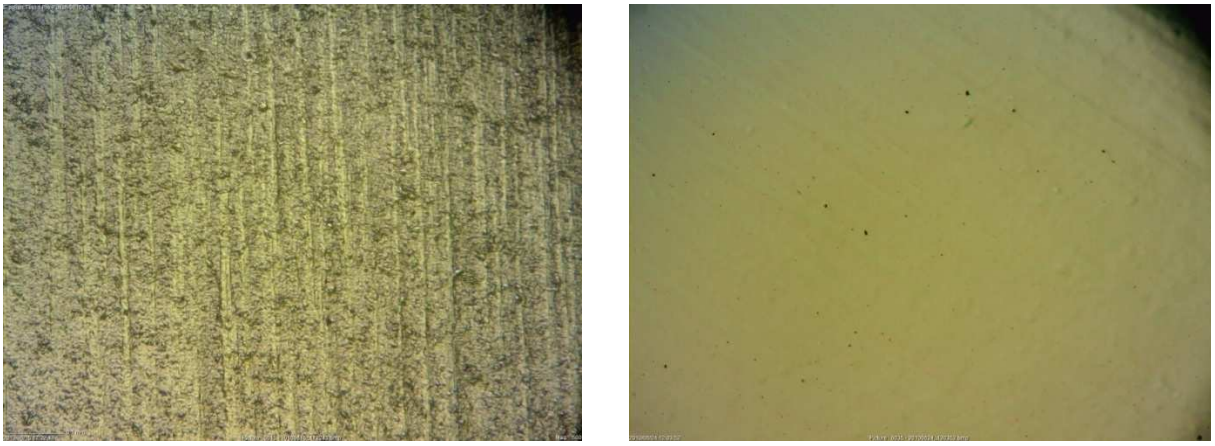

Fig. 2 a) Optical microscope picture of DSC pan before a) and after b) electro-polishing

DSC heating/cooling runs were conducted using DSC pans with various surface roughness using pure NaNO3. Figures 3,4,5 show the results of the tests for varying root means square (RMS) surface roughness with a cooling rate of 10, 50 and 100°C/min respectively.

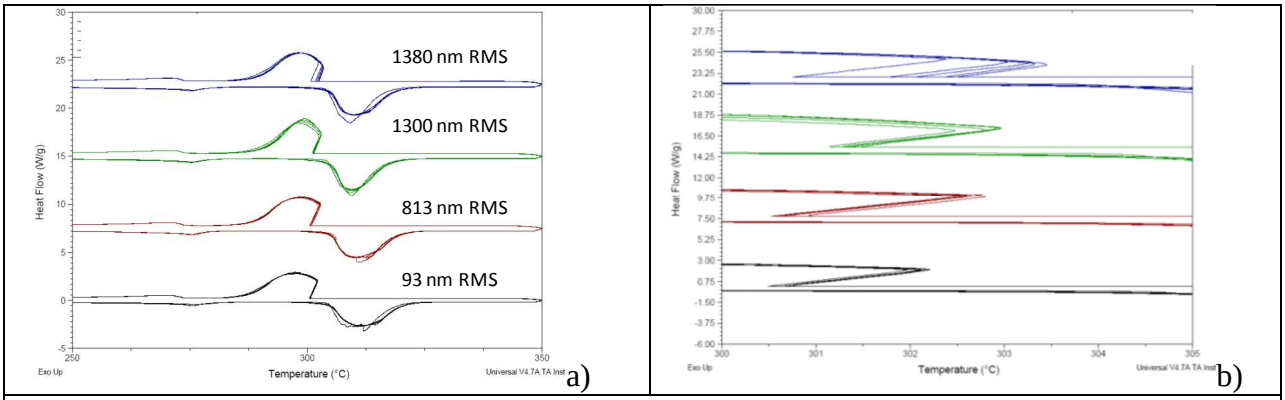

Fig. 3 DSC results for NaNO3 samples with varying surface roughness using 10 ^{o}C/min cooling rate. a) entire temperature range b) narrow temperature range emphasizing solidification event.

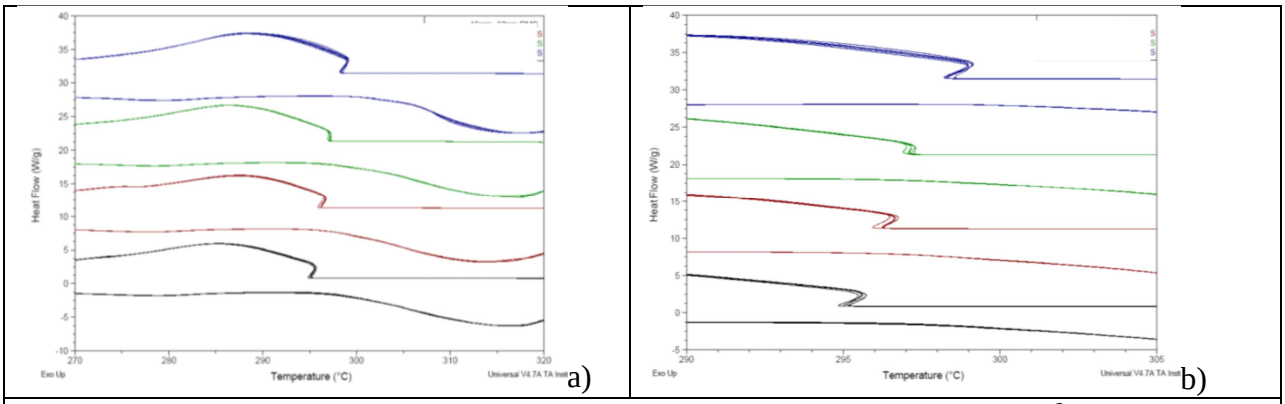

Fig. 4 DSC results for NaNO3 samples with varying surface roughness using 50 ^{o}C/min cooling rate. a) entire temperature range b) narrow temperature range emphasizing solidification event

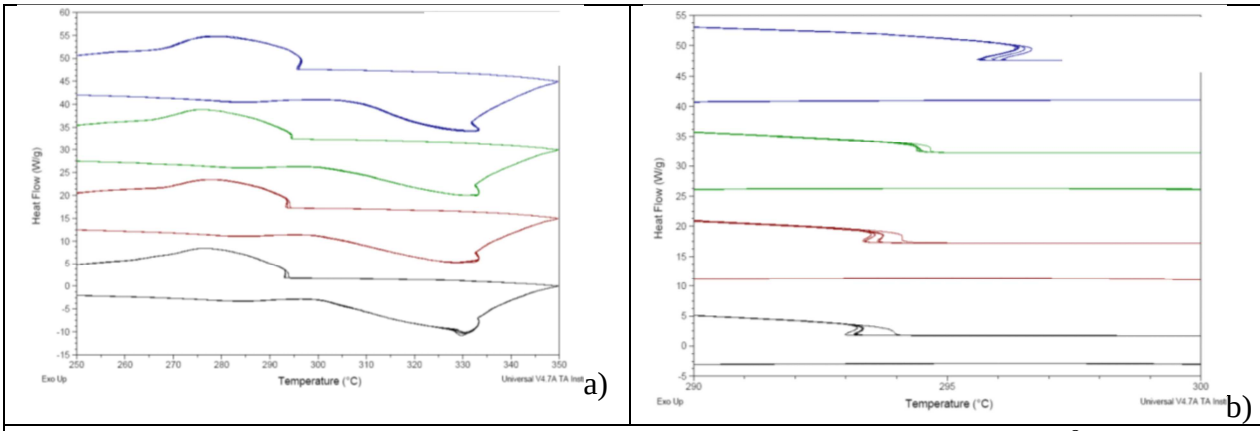

Fig. 5 DSC results for NaNO3 samples with varying surface roughness using 100 ^{o}C/min cooling rate. a) entire temperature range b) narrow temperature range emphasizing solidification event

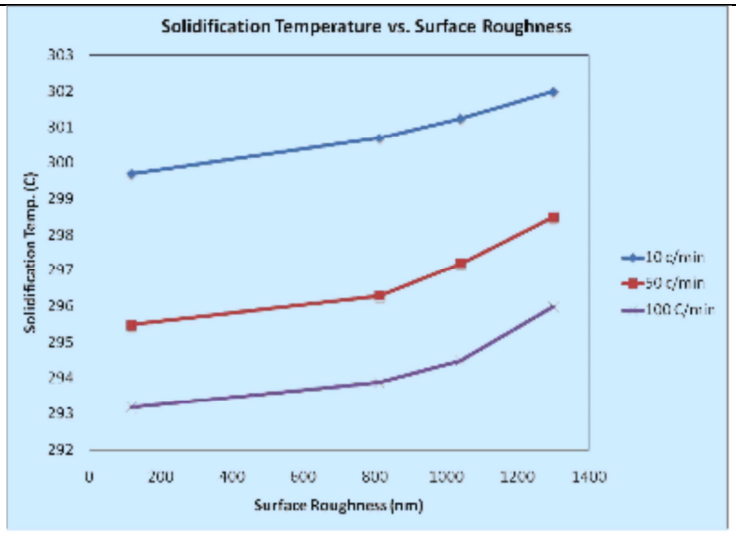

Figure 6 Effect of surface roughness on Solidification temperature for 3 different heating rates.

The results show that decreased surface roughness causes a significant shift of solidification toward lower temperatures for all of the heating rates. The shift is more pronounced at higher heating rates. The shift caused by surface roughness is more appreciable in Figure 6.

Effects of surface composition (coating material)

In order to examine the effects of surface coating on the solidification event, we coated the DSC pan with different materials: Cu, Ag, Ni, Cr, and TiN. Figure 7 are the results of the DSC tests.

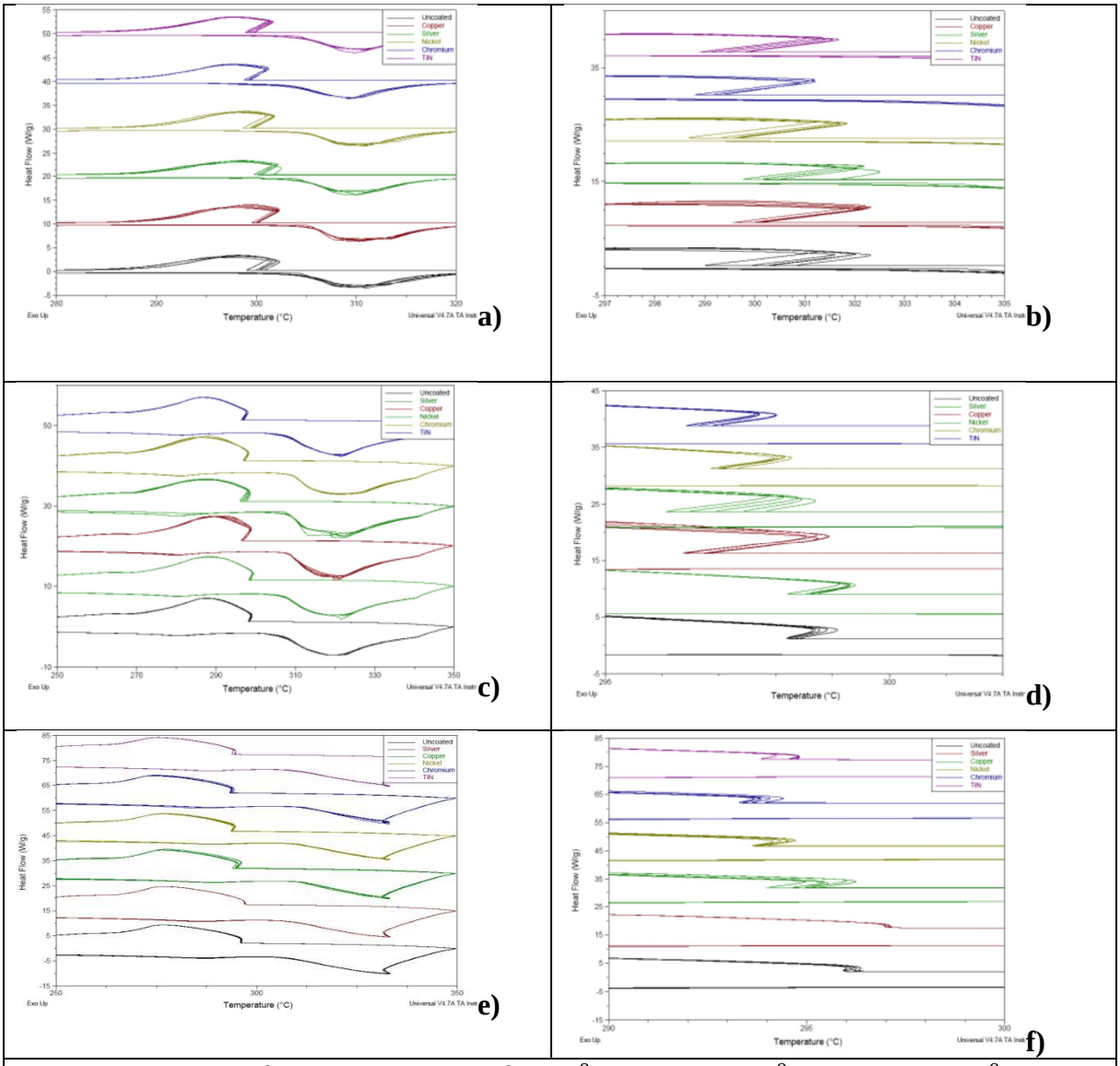

Figure 7 DSC plots for various coatings for 10 ^{o}C/min (a,b), 50 ^{o}C/min (c,d), 100 ^{o}C/min (e,f).

The results show that all of the coating materials cause a shift in the solidification temperature. Ag actually has a negative effect (shifts the solidification temperature to higher temperatures). The rest of the materials decreases the solidification temperature. The shift is largest for the Cr coating.

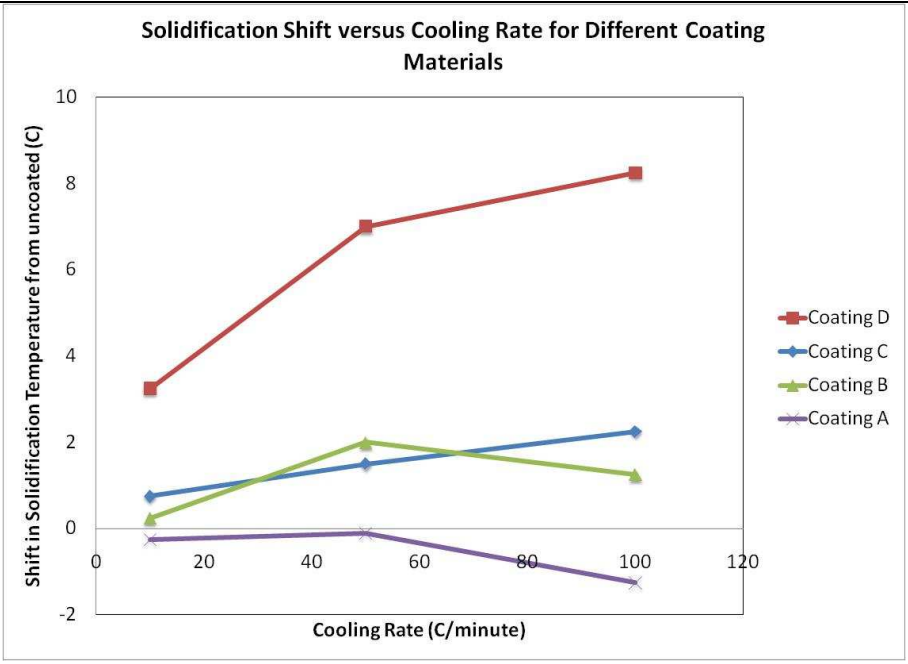

Figure 8 Shift of solidification temperature for different coatings at 3 different cooling rates.

Selected Coating for Experiments with the NaNO3-NaOH Dilute Eutectic Mixture

Seamless heat exchanger tubes were first electropolished and then coated with chromium. The electropolishing solution and method is described in Appendix 2. The morphology of the chrome coating is important.

Section 5
Morphology of Freezing Salt Mixture

According to previous studies, the best binary salt system is NaOH-NaNO3. Fig 1 shows the binary phase diagram for this system. Three different binary compositions were selected for the primary studies in this system. These three compositions are as below:

1- NaNO3 (100%)

2- NaOH (10wt%) – NaNO3 (90wt%)

3- Eutectic composition of: 15.8wt% NaOH-84.2wt%NaNO3

Fig 2 shows the cooling curves for pure sodium nitrate with different amount of purity. In fig 2A, B and C cooling curves are related to sodium nitrate with 98% purity and in all of them transformation temperature is about 300°C with 0.5C accuracy (table 1). Supercooling however varies from 0.1C to 0.4 C. For the 99.999% grade sodium nitrate the freezing point is accurately 308C due to the phase diagram (fig 1). The supercooling however is 0.8C, which is the highest supercooling obtained among all. This can be due to the high purity of NaNO3 and also higher cooling rate. Note that the temperature accuracy is less than 0.07C with the instruments used.

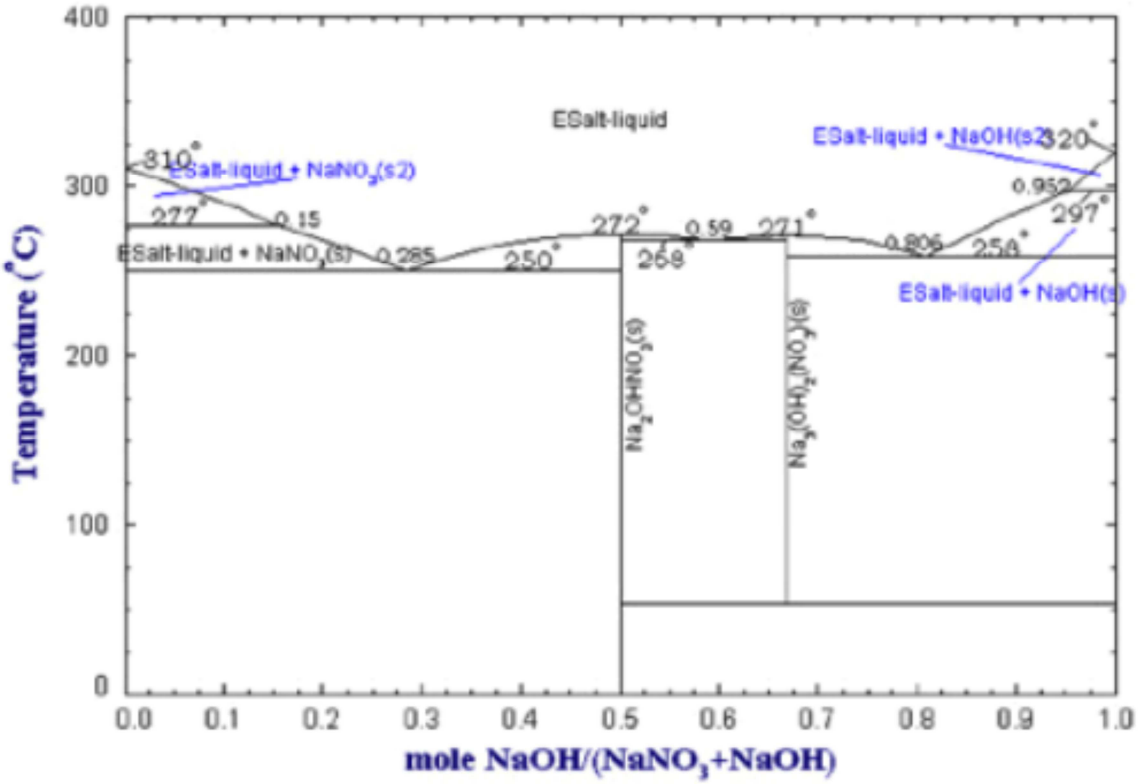

Fig 1 NaOH-NaNO3 binary system phase diagram [1]

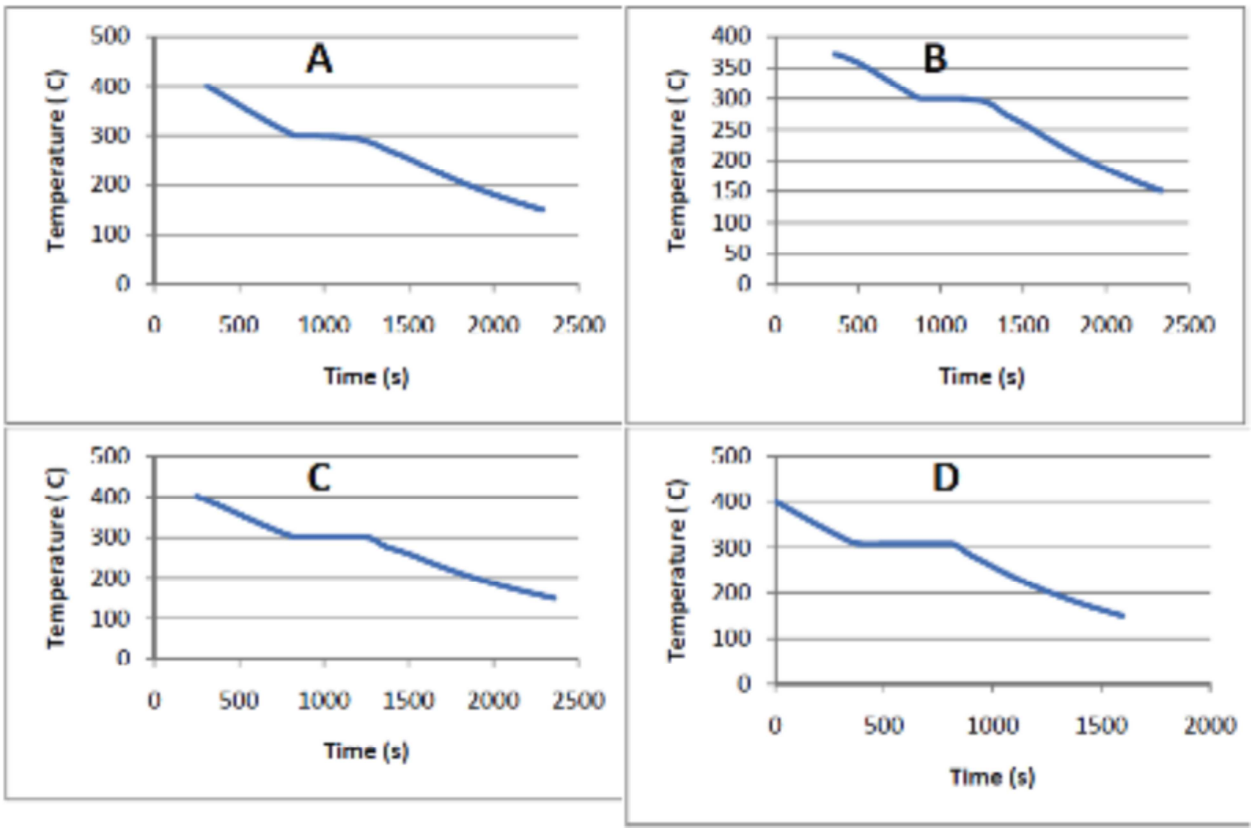

Fig 2 Cooling curves A, B and C: NaNO3(98%), D: NaNO3 (99.999%)
Table 1 Data extracted from fig 2 {A, B and C: NaNO3(98%), D: NaNO3 (99.999%)}

Fig 3A shows the as cast patterns of ingot for general metals and alloys. Grains in the as cast ingots are generally 3 types: equiaxed, columnar and zones in the chill zone which are forming first on the mold's wall. In each metal and alloy depending on the solidification condition and also the composition and type of metal or alloy each zone can be changes or disappears. Our observations on the selected salt system using different ingots such as aluminum, steel, alumina, quartz, and pyrex shows the model in fig. 3B, which means the equiaxed and chill zone are not appearing in the as cast ingot microstructure. However structure of the as cast salt can be dendritic as fig 4 shows, in the as cast sodium nitrate with 98% purity.

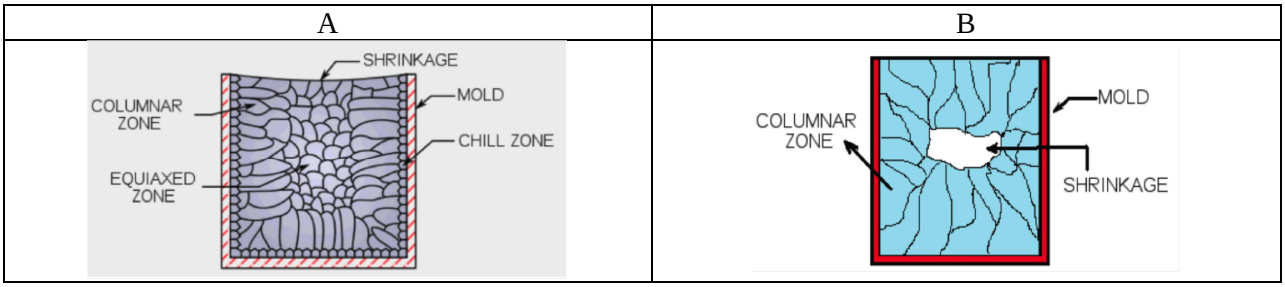

Fig 3 A: General Ingot as cast pattern, B: Salts as cast pattern

Composition	Cooling rate (^{o}C/min)	Transformation Temperature (^{o}C)	Super cooling (C)
NaNO3 (A)	7.6	299.9	0.16
NaNO3 (B)	6.7	299.6	0.103
NaNO3 (C)	7.1	300.6	0.4
NaNO3 (D)	9.4	308	0.84

Fig 4 Ingot as cast pattern for $NaNO_3$ with 98% purity

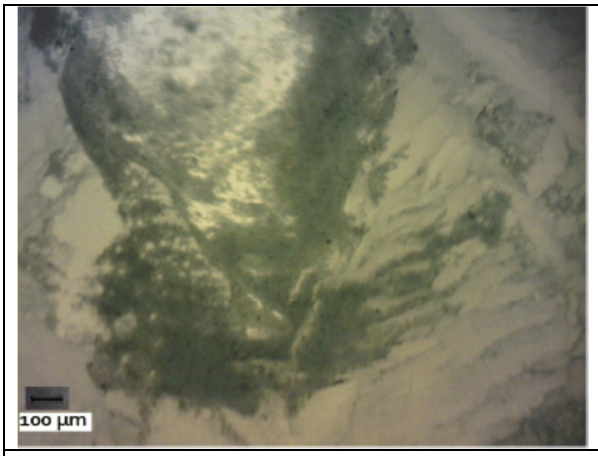

A

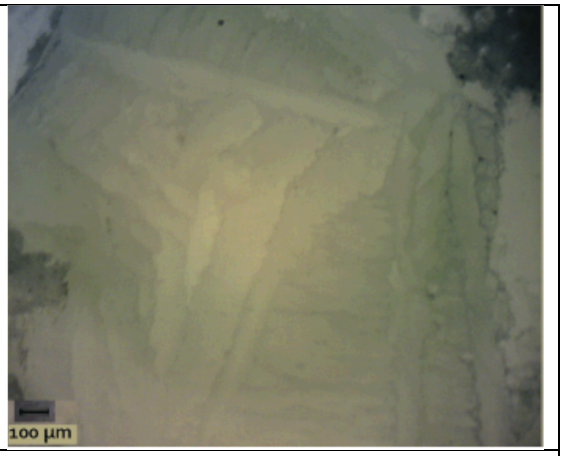

B

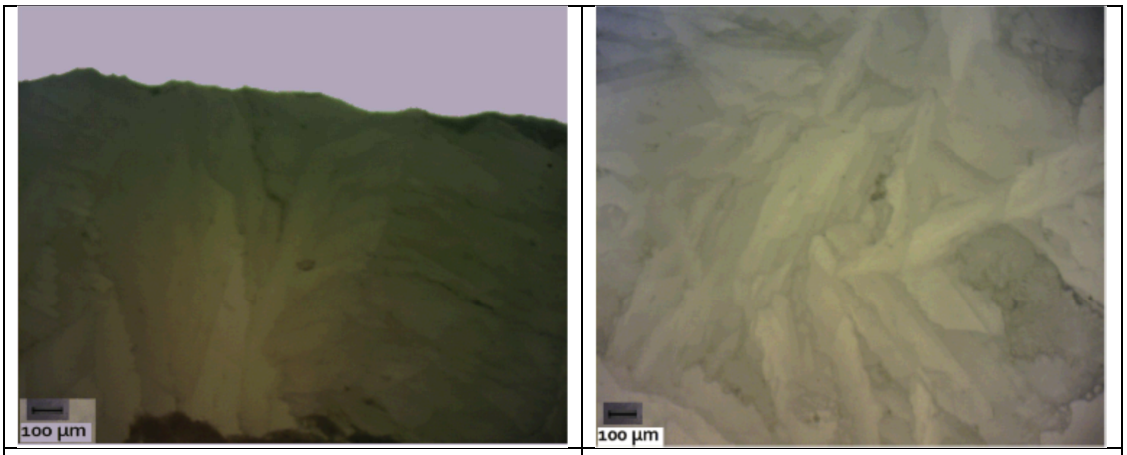

Fig 5 Magnified images of as cast NaNO3 ingot, A: center of the ingot with cavity, B: bottom left of the ingot, C:Top of the ingot, D: Top right of the ingot

Fig 5 shows the magnified cross section of as cast NaNO3 with 98% purity. As it can be seen the columnar zone has occupied the microstructure, with the primary columns elongated from wall to the center and secondary dendritic arms. This dendritic microstructure is because of the presence of 2% impurities. Fig 6 shows the same microstructure but polished from the top of the ingot. In this image different dendritic colonies can be observed with a better contrast.

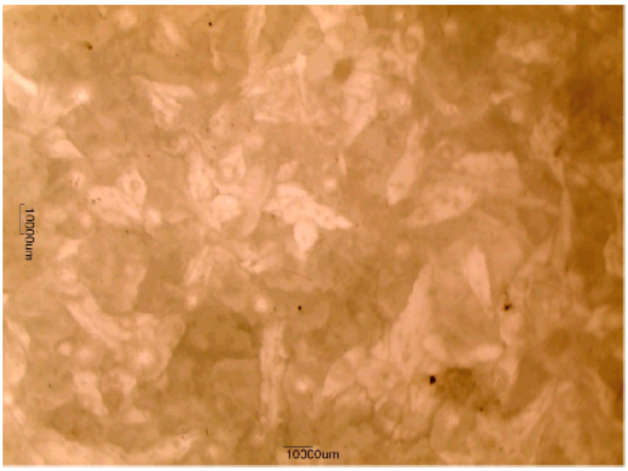

Fig 6 Microstructure of NaNO3 from top of the ingot (Polished structure)

Fig 7 shows the cooling curves for eutectic composition of NaNO3-NaOH with different amount of purity. In fig 7A, B and C cooling curves are related to sodium nitrate and sodium hydroxide with 98% purity and as indicated in table 2, the transformation temperature for these curves is less than the actual eutectic temperature according to fig 1 because of the impurities. In fig 7 D the cooling curve is related to the eutectic composition using sodium nitrate and sodium hydroxide with 99.999% purity, and as table 2 shows the transformation temperature is about 247, which is near to the reported eutectic temperature in fig 1 (250 ^{o}C). Table 2 shows good supercooling temperatures for the C and D compositions. However the amount of supercooling for the A and B compositions is relatively low, and based on the cooling rate it should be higher. The reason can be a non-accurate experiment or problem with thermocouple and those experiments should be repeated.

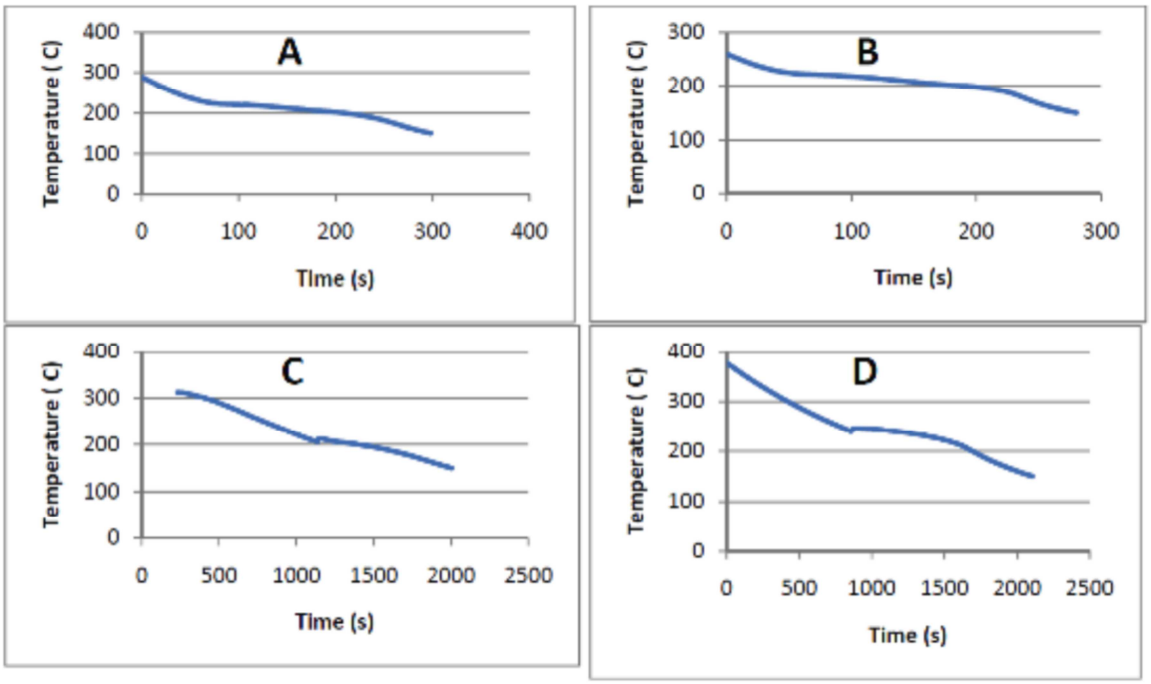

Fig 7 Cooling curves for Eutectic composition of NaNO3-NaOH A, B and C: NaNO3 and NaOH with 98% purity D: NaNO3 and NaOH with 99.999% purity

Composition	Cooling rate (^{o}C/min)	Transformation Temperature (^{o}C)	Super cooling (C)
NaNO3-NaOH (15.6%) (A)	27.8	219.5	1.2
NaNO3-NaOH (15.6%) (B)	23.4	219	0
NaNO3-NaOH (15.6%) (C)	5.5	207	6.8
NaNO3-NaOH (15.6%) (D)	6.5	247	5.9

Table 2 Data extracted from fig 7 {NaNO3-NaOH A, B and C: NaNO3 and NaOH with 98% purity D: NaNO3 and NaOH with 99.999% purity}

Fig 8 shows the cooling curves for hypo eutectic composition of NaNO3- 10wt%NaOH with different amounts of purity. In fig 8A, B and C cooling curves are related to sodium nitrate and sodium hydroxide with 98% purity and the transformation temperatures for these curves are shown in table 3. It is expected for this composition to have two transformation temperatures.
The first transformation happens when the first sodium nitrate solidifies and the second transformation is when the eutectic transformation happens. As it can be seen in the cooling curves, eutectic transformation for all cooling curves A,B and C cooling curves at less than 250 ^{o}C between 230-235 ^{o}C and this temperature off-set is due to the impurities. However the primary solidification of sodium nitrate cannot be detected in these curves. The reason can be the small amount of latent heat of fusion release, which is not sufficient to make a change on temperature or create supercool. In fig 8 D the cooling curve is related

to the hypo eutectic composition using sodium nitrate and sodium hydroxide with 99.999% purity, and as table 3 shows the transformation temperature of 250°C, which is exact reported eutectic temperature in fig 1. Also table 2 shows supercooling temperatures for the A and B compositions more than C and D and the reason is because of the higher cooling rate.

Fig 9 A, B and C: Dendritic structure of $NaNO_3$-10wt%NaOH, D: microstructure change from sharp dendrites to fine rounded dendrites when $NaNO_3$ and NaOH used in the NaNO3-10%NaOH composition are pure (99.999%)

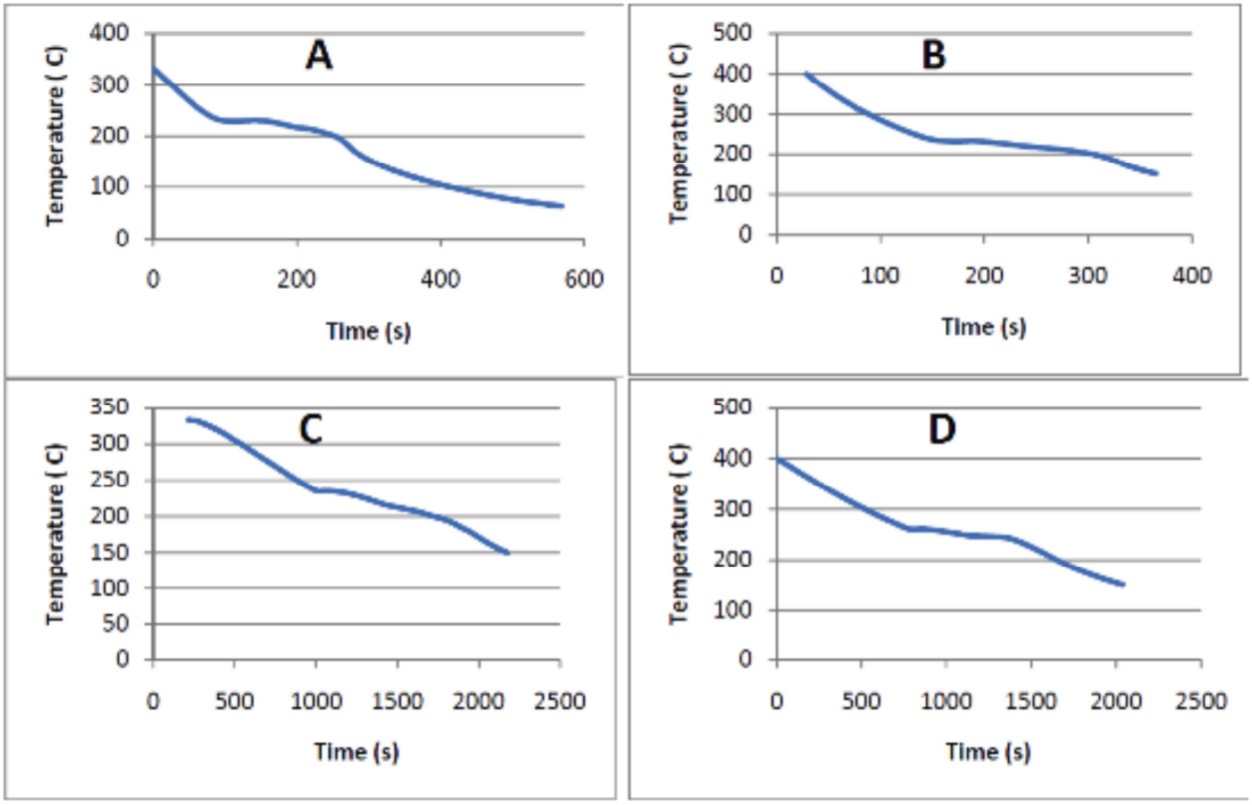

Fig 8 Cooling curves for NaNO3-10wt%NaOH composition of NaNO3-NaOH A, B and C: NaNO3 and NaOH with 98% purity D: NaNO3 and NaOH with 99.999% purity

Composition	Cooling rate (°C/min)	Transformation Temperature (°C)	Super cooling (C)
NaNO3-NaOH (10%) (A)	35.9	230	1.6
NaNO3-NaOH (10%) (B)	44.5	233	1.5
NaNO3-NaOH (10%) (C)	5.6	235	0.6
NaNO3-NaOH (10%) (D)	7.4	250	0.3

Table 3 Data extracted from fig 8 { NaNO3-NaOH A, B and C: NaNO3 and NaOH with 98% purity D: NaNO3 and NaOH with 99.999% purity}

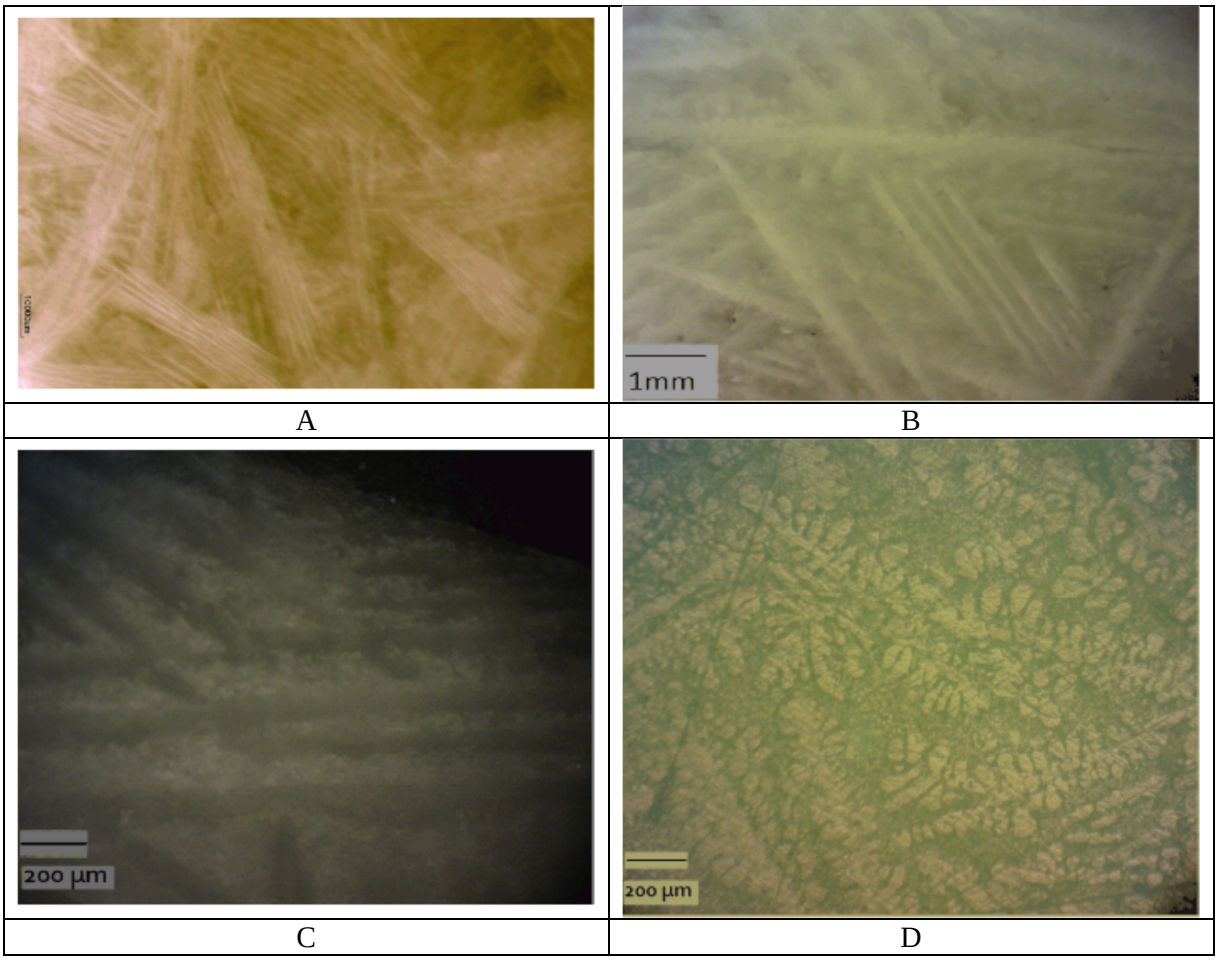

Fig 9 A, B and C: Dendritic structure of $NaNO_3$-10wt%NaOH, D: microstructure change from sharp dendrites to fine rounded dendrites when $NaNO_3$ and NaOH used in the NaNO3-10%NaOH composition are pure (99.999%)

It was pointed out in background studies that if the liquid is at a lower temperature than the interface, dendritic growth is observed. This implies that an initially smooth interface is unstable in the presence of a temperature inversion. In a smooth interface under ordinary growth conditions and supercooled interface a ribbon shaped crystal with its two flat surfaces parallel to a closely packed plane of structure may forms [34]. Fig 9 shows the different structures based on the cooling curves in fig 8. As it can be seen the morphology of the primary dendrites formed in the microstructure of the hypo eutectic composition changes with the amount of impurities in the microstructure. Figure 9 A, B and C show the same needle type dendrites but different sizes, and as purity of the composition increases the morphology of the dendrites totally changes to a more round type dendritic structure in fig 9-D. The supercool temperatures and cooling rates does not have any effect on the shape of primary dendrites but changes the size of the dendrites. As it can be seen in figure 9 the higher the rate, results to a finer dendritic structure. The type of dendrite structure in fig 9 A, B and C can be what reported in aluminum alloys [2-3], called as feather crystals and feather growth. The crystals shown in this figure appear to resemble ribbon crystals in that they always contain twin planes, but it is not obvious why a twin mechanism should come into play in a material in which the interface is believed to be diffuse. It is possible that the feather crystals grow only when the supercooling at the interface is so small that the diffuseness of the interface is insufficient to allow new layers to form. This explanation is not supported by the observation that feather crystals do not occur unless the conditions are such that growth is fast. Although the significance of this research is based on the primary formed dendrites and their morphology, since in solar power plant heat exchanger the solidification only happens partially and never reaches to the eutectic point, recognition of

the eutectic structure is important in order to understand the difference between the primary dendrites and dendrites lie in the eutectic structure. As discussed before the smooth interface is caused because of the completion of the atomic layers, and in this type of structure eutectic structure is irregular and hard to detect. Also because of the supercooling formation of divorced eutectic happens as it is indicated in fig 10.

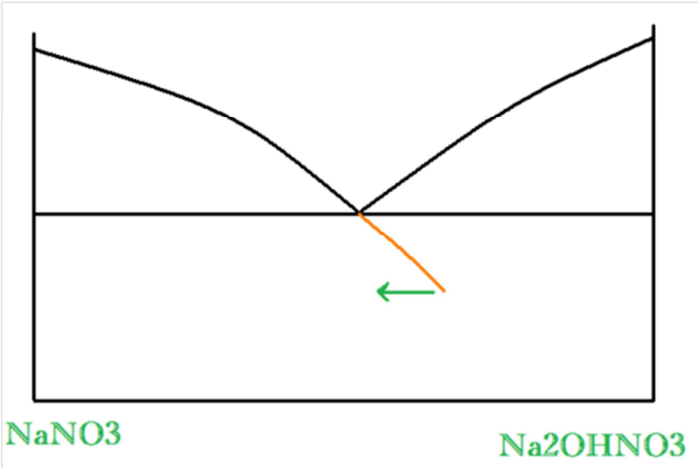

Fig 10. NaNO3-NaOH Phase Diagram

Fig 11 shows a microstructure of a divorce eutectic in the composition of NaNO3-10%NaOH with purity of 99.999%. The dark parts are sodium hydroxide and it can be seen they have absorbed some moisture due to the nature of being so hygroscopic.

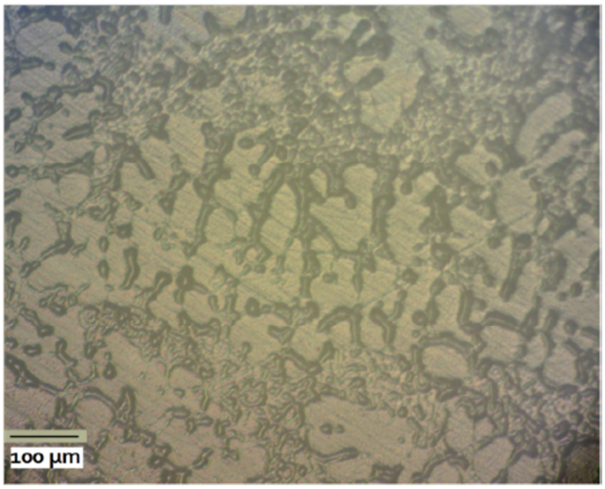

Fig 11 Divorced Eutectic structure in the composition of NaNO3-10wt%NaOH with purity of 99.999%

Appendix 1 discusses viscosity of salt mixture at near freezing temperature. There is very scant data on viscosity of salt near melting and freezing, because it is difficult to measure. Fig 12 and 13 show our initial attempt to measure viscosity of a eutectic and a hypo eutectic composition of NaNO3-10wt%NaOH. In fig 12 viscosity has been measured in the temperature range right above the freezing point. The freezing point for the first solidified eutectic is 260C according to phase diagram in fig 1 but because of the supercooling and also temperature reading off-set in this chart no solidification has occurred. The tread line shows the linear viscosity change with temperature change. As it can be seen viscosity of the molten salt changes between 1-2 cp. By increasing the temperature the viscosity decreases as in fig 13 and gets more near to 1 cp. The behavior of molten salt's viscosity is what expected according to [4](see Appendix 1) .

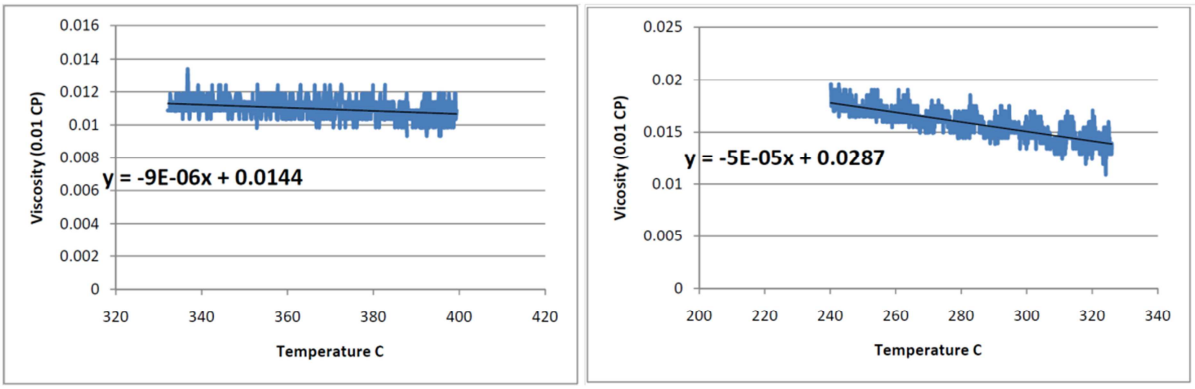

Fig 12 and 13 Viscosity-Temperature chart of the eutectic and hypo eutectic composition of NaNO3-10wt%NaOH in the temperature range of right above the freezing point

Measuring viscosity at or near freezing or melting temperature is challenging. Figure 14 shows the viscosity of sodium nitrate salt near melting temperatures (300 to 308 C). These measurements were at conducted at NREL by Dr. Anne Starace.

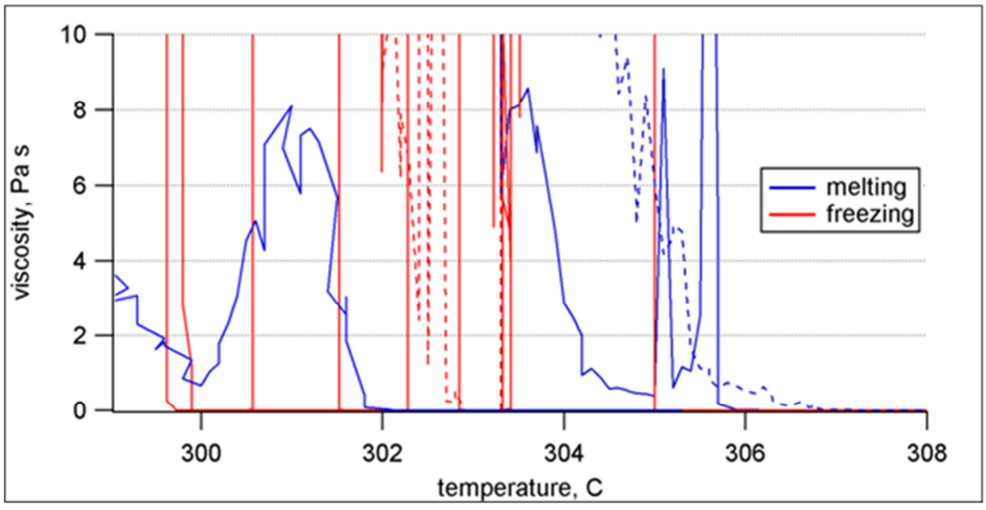

Figure 14. Measurement of viscosity near freezing and melting temperatures for NaNO3

Section 6
Design of Laboratory Scale Prototype

Focus of this Section

This section focuses on the design of the experiment apparatus for studying the heat transfer performance in latent heat storage systems. The report begins with a baseline analysis balancing predicted overall heat transfer coefficient and solidification with heat exchanger area. After this, more detailed analysis is presented to analyze the effects of tube size on Reynolds number, pressure drop, % solidification, etc. The purpose of this is to establish a baseline of calculations for further detailed design to follow. The analysis assumes cross flow, which should be analogous to a baffled shell and tube heat exchanger.

Introductory Analysis

To begin our analysis we will present a baseline energy balance calculation. We balance the overall heat transfer rate with the energy it takes to bring the salt down to melting temperature and achieve a solid fraction of 20%. For the purposes of this calculation we assume tubes of 0.375" OD, and a channel cross section of 10 diameters square (i.e., 3.75" x 3.75"). We account for 50% of this area being blocked by tubes giving us a cross sectional area, A_c, of .009 m^2*50%. We also assume an overall ΔT of 15 degrees Celsius between salt and tube walls, and an inlet superheat of 5 degrees Celsius.

$$\dot{Q} = hA_s\Delta T = \dot{m}\left(C_pT_{superheat} + H_f\varphi\right) = \left(\rho A_c V\right)\left(C_pT_{superheat} + H_f\varphi\right)$$

h (W/m^2K)	500
ΔT (C)	15
C_p (kJ/kgK)	1.821
$T_{superheat}$ (C)	5
H_f (kJ/kg)	174
ϕ (% Solid)	20%
ρ (kg/m^3)	2260
A_c (m^2)	.009*50%

From this we are left two independent variables: heat exchanger surface area A_s and salt velocity V. If we assume a velocity of 1 m/s (Re_D=8300), Q works out to 450 kW, which leads us to a heat exchanger area of 60 m^2. This means for an array of 40 cooled tubes we would need over 525 passes to achieve the desired solid fraction. Alternatively, we could achieve the desired 20% solid fraction at only 14 kW if we decreased the salt velocity to 0.03 m/s; however in this case the salt-side Reynolds number would be only 250.

Importance of Reynolds Number

The capability of operating at high Reynolds number is an important functionality for this apparatus for two major reasons:

(i) To ensure that we can produce the hydrodynamic forces that will be necessary to achieve "flaking" of the salt off of the tube. The larger the range of Reynolds numbers we can test, the larger the range of coatings we will be able to test. Even if our coatings fail to flake at industrially viable Reynolds numbers, if we can prove that flaking will occur at higher Reynolds numbers this will be proof that our concept is viable. From a scientific perspective if we could hit a high enough Reynolds number to flake off of a plain or coated steel tube, we could begin to perform a thorough study in which we could possibly come up a with a formula to relate coating surface energy to Reynolds number necessary for flaking. This would make heat exchanger design for the full scale system very simple. On the other end, if we don't give ourselves the capability of high Reynolds numbers we may fail to create the flaking phenomenon at all.

(ii) Scaling to match full-size heat exchangers: Based on initial familiarity with typical full-scale heat exchangers involving molten salt, we expect that a typical Reynolds number is in the range of 20,000. Also, typical convection design curves for staggered tube banks and shell & tube heat exchangers show a transition in behavior at around $Re_D \approx 1{,}000$, in terms of both pressure drop and heat transfer [ref. *Perry's ChemE Handbook*; Zukauskas in Hartnett & Irvine *Adv. Heat Transf*]. Therefore, to be able to match the approximate operating conditions of a full-scale heat exchanger, it is important for this apparatus to be capable of operating in the ReD range of several 1,000 at the very least, and with a strong preference to reach the range of 20,000+.

Heat Exchanger Design

The main goal of the system is to determine the salt side convection coefficient. Figure 1 shows a schematic of the thermal resistance network of the heat exchanger during solidification. The salt side convection coefficient contains two terms, the external convection as well as conduction through any solid salt on the surface. As shown in equation 2, we assume the contribution of the solid salt conduction is negligible, as well as conduction through the thin stainless steel tube. Effects of any solid salt layers forming will be captured in the h_{salt} measured and the stainless steel tube is too thin to play a significant role in the measurement. That leaves only $h_{coolant}$ and h_{salt} as contributors to the overall heat transfer coefficient. Assuming we can make $h_{coolant} >> h_{salt}$, a measurement of the overall heat transfer coefficient will give us a measure of how effectively the salt can transfer heat under real heat exchanger conditions. By measuring the flow rates and inlet and outlet temperatures of each system, we can determine the Log Mean Temperature Difference and calculate the overall heat transfer coefficient.

To determine how to scale the system down, we must first look at the configuration of the full scale system. In the full scale system hot salt will come from the superheat heat exchanger slightly above the melting point of the salt. This salt will be pumped through a shell and tube heat exchanger where the heat from the salt will boil steam on the inside of the tubes. This steam will be diverted to a turbine, which will then produce electrical power. System calculations performed by Anoop Mathur show that a potential heat exchanger design would utilize 1" diameter tubes, with a salt velocity of approximately 3 feet per second. We scaled these conditions to dimensionless Reynolds and Nusselt numbers to help determine the sizing requirements for our scaled system.

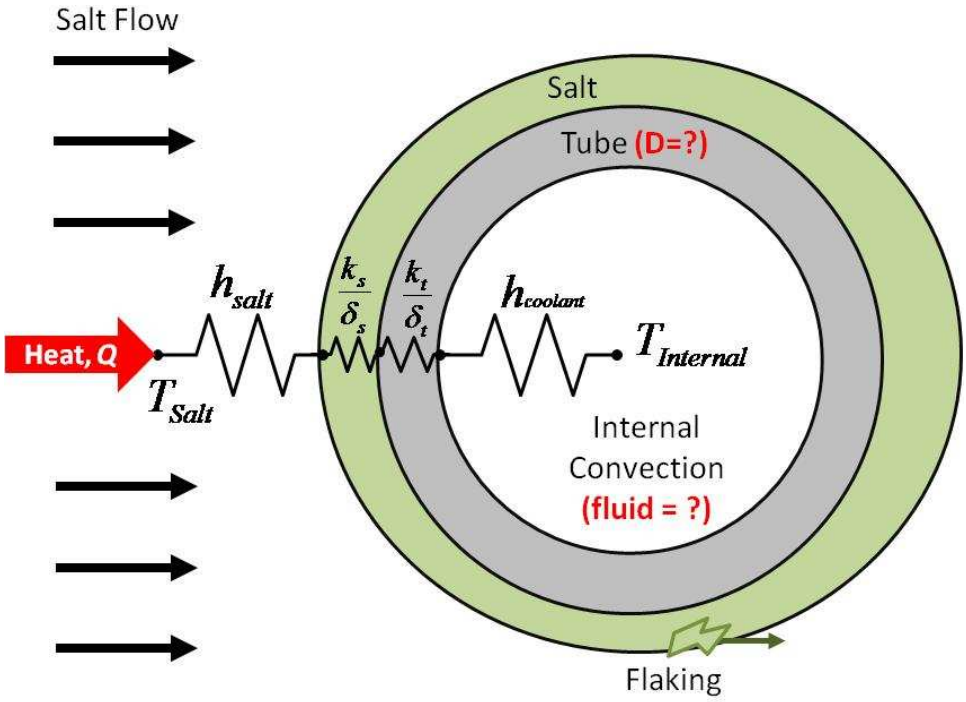

Figure 1: Schematic of Heat Transfer during Solidification on Heat Exchanger Tube

$$\frac{1}{U} = \frac{1}{h_{Salt}} + \frac{\delta_s}{k_s} + \frac{\delta_t}{k_t} + \frac{1}{h_{coolant}} \qquad (2)$$

Best Case, $\delta_s \to 0$ — Thin SS Tube

In the scaled system, it is highly beneficial to avoid steam generation as the pressure of saturated steam at the melting point of the salt is approximately 1250 psi. This creates a highly hazardous situation as the system would have be extremely meticulously designed in order to avoid a high pressure leak of steam that could create extreme hazards when combined with the molten salt. Therefore it is highly preferential to find another heat transfer fluid that will provide effective heat transfer under safer conditions.

Heat Transfer Fluid Selection

Five different heat transfer fluids were analyzed under sample conditions to analyze their effectiveness as a heat transfer medium. A ¼" tube with an L/D ratio of 30 was utilized for this analysis. Compressed air and helium were analyzed at a pressure of 60 psi. Figure 2 shows the pressure drop versus convection coefficient for each fluid and Figure 3 shows the flow rate versus convection coefficient for each fluid. From these graphs it was determined that Therminol© and compressed helium were the most effective solutions.

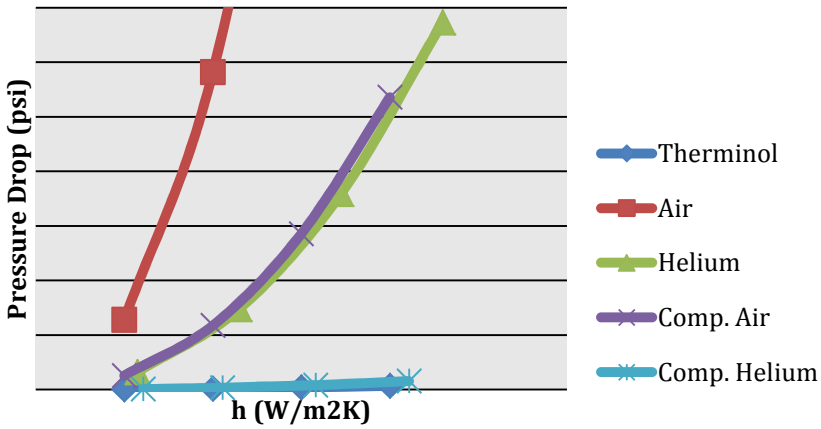

Figure 2: Sample System Pressure Drop vs. Convection Coefficient for Different Heat Transfer Fluids

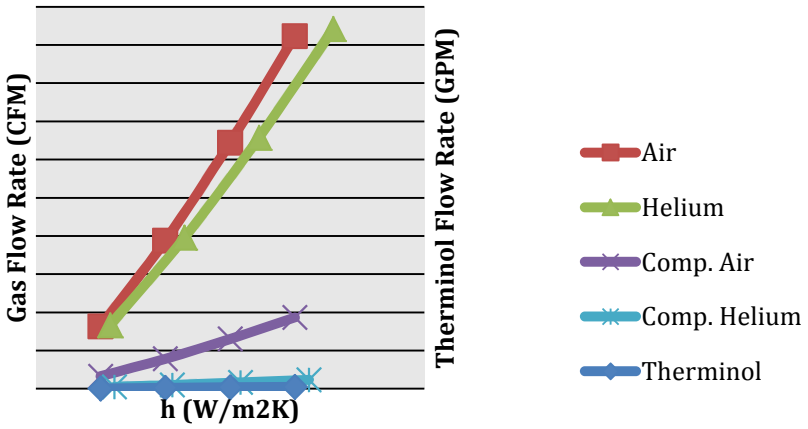

Figure 3: Sample System Flow Rate vs. Convection Coefficient for Different Heat Transfer Fluids

From here, a basic design for each system was laid out and the pros and cons of each system analyzed. Compressed helium is good because it is easy to work with, simple to implement (no special research required), leaks are easy to deal with and tolerate, and the overall system complexity is reduced. However, it is not normally used in industry, is more expensive, and is still a pressurized system. Therminol is beneficial due to fact that the system does not have to be pressurized, higher heat transfer rates are more easily achievable, it is less expensive, and it is widely accepted in industry. The Therminol system is much more complicated though, more safety issues are involved in the design, leaks are more difficult to tolerate, and a good amount of research is necessary to ensure proper implementation. In the end Therminol was chosen because of its acceptance in industry, and how much cheaper the system is.

Figure 4 shows the pump work required versus heat transfer coefficient for each fluid. The helium compressor requires significantly more power and therefore the ratio of helium compressor to Therminol pump cost is approximately 8:1 ($10,000 vs. $80,000).

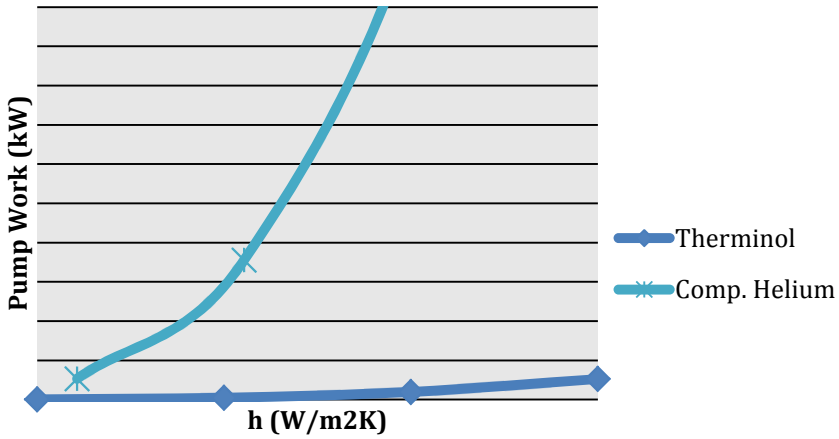

Figure 4: Pump Work vs. Convection Coefficient for Therminol and Compressed Helium

Heat Exchanger Design

Once a heat transfer fluid was selected, it was necessary to perform detailed scaling calculations to maximize the effectiveness of the system while utilizing as small a scale as possible. In order for the system to perform effectively there are a number of factors that must be carefully balanced. The first is high oil heat transfer. The higher this is, the easier it will be to isolate the actual salt heat transfer coefficient. Next is a low pressure drop, which allows us to utilize smaller pumps. A high Reynolds number on the salt side is beneficial as it will produce larger hydrodynamic forces that may help flake salt off of the tube. Another very important factor is the change in solid fraction that can be achieved through the heat exchanger. The higher the change in solid fraction that we can achieve, the better the industrial readiness of the system being tested.

A staggered tube bank was chosen as the best physical design due to the fact that the geometry is well understood, and heat transfer modeling becomes very simple. This geometry is very true to industry practice and also maintains the external cross-flow orientation that an industrial shell and tube heat exchanger would have. All calculations assume a 4x10 staggered tube bank. Equations 2-4 show some of the general equations used in these calculations. Any other equations used can be found in Incropera and Dewitt's Introduction to Heat Transfer [6].

$$Re_{D,max} = \frac{\rho V_{max} D}{\mu} \quad (3)$$

Where $Re_{D,max}$ is the maximum Reynolds number through the tube bank, ρ is the density of the fluid, V_{max} is the maximum velocity through the tube bank, D is the diameter of the tubes, and μ is the dynamic viscosity of the fluid.

$$\overline{Nu_d} = 1.13 C_1 Re_{d,max}^{m} Pr^{\frac{1}{3}} \quad (4)$$

$$\begin{bmatrix} N_l \geq 10 \\ 2000 \leq Re_{D,max} \leq 40{,}000 \\ Pr \geq .7 \end{bmatrix}$$

$$\Delta p = N_L \chi \left(\frac{\rho V_{max}^2}{2}\right) f \quad (5)$$

The length of tube to tube diameter ratio was held to a constant value of 10. Pitch between the tubes in both the longitudinal and transverse direction was twice the diameter. All values shown are on a per pass basis, once calculations were finalized, passes were added where necessary to generate the desired results.

A series of figures is presented, followed by a table summarizing the calculations. The salt side of the loop was analyzed first. Figure 5 shows the pressure drop through the heat exchanger on the salt side. As the tube size decreases, the pressure drop increases significantly. Figure 6 shows the maximum Reynolds number achievable at 140 GPM (this was used as a design point because it is the maximum achievable flow rate achievable by an older pump that we had.) Figure 7 shows the salt solid fraction achievable per pass versus flow rate in GPM. Figure 8 shows the cooling rate required to balance the solidification and cooling versus tube diameter. This was an extremely important design point as it plays a large role in determining the steady-state load on the heating system.

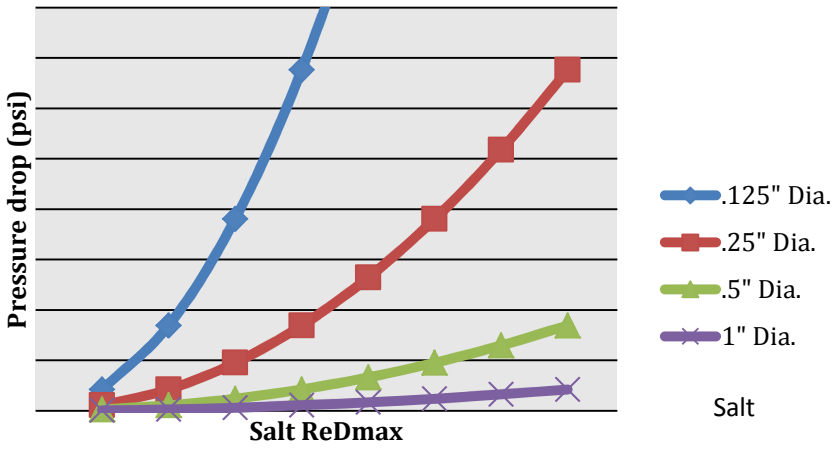

Figure 5: Salt Pressure Drop vs. ReDmax for Different Tube Sizes

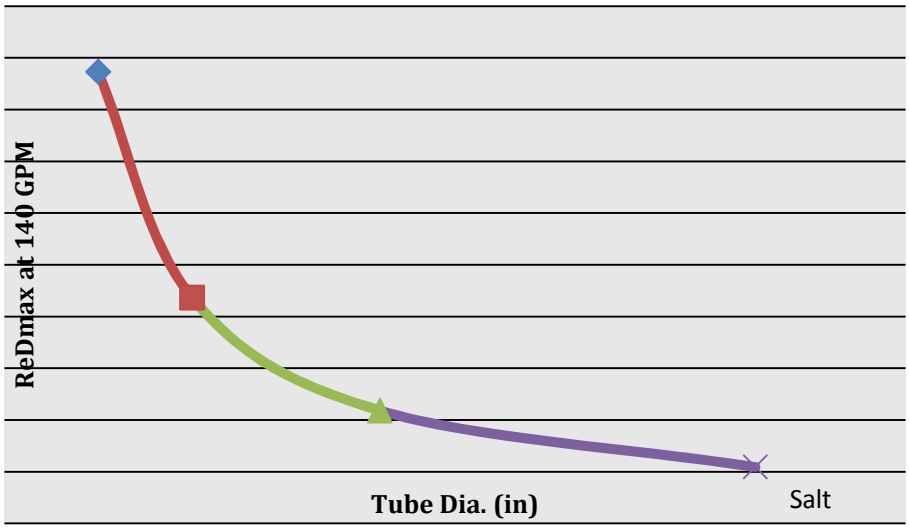

Figure 6: Salt ReDmax at 140 GPM Flow Rate vs. Tube Diameter

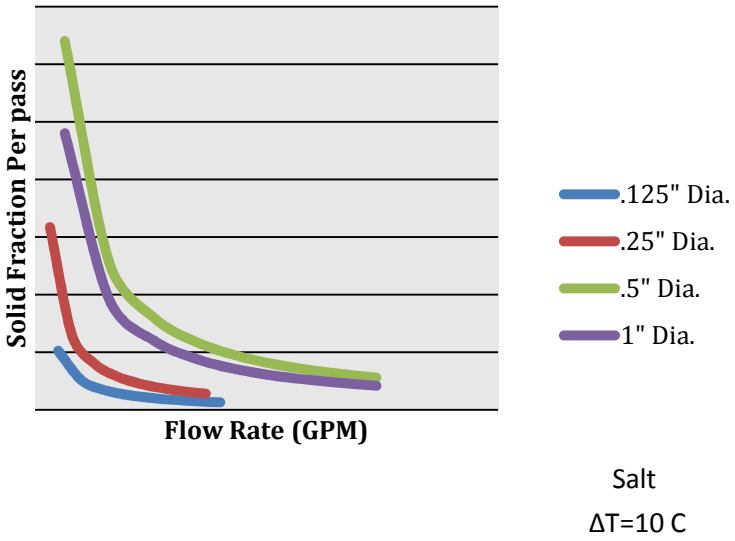

Figure 7: Salt Solid Fraction per Pass vs. Flow Rate

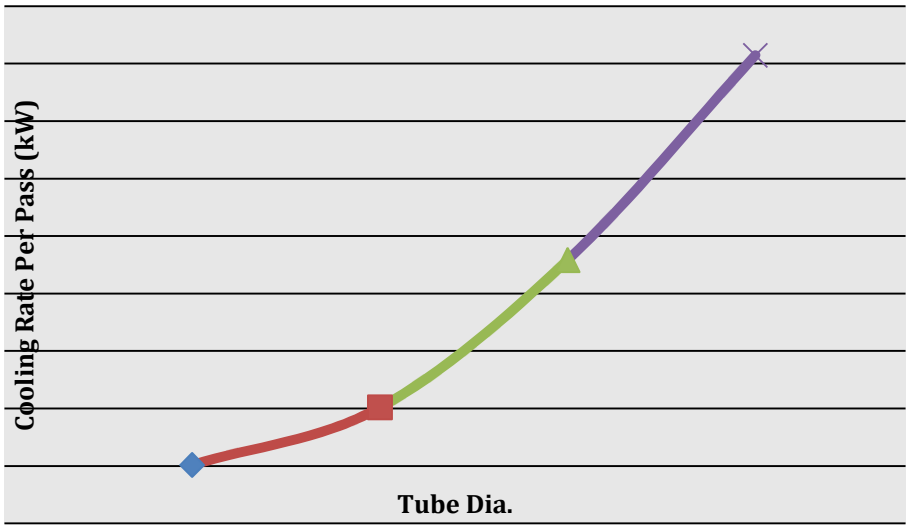

Figure 8: Cooling Rate Required Per Pass vs. Tube Dia.

The Therminol Side shows similar trends. Figure 9 shows the Therminol pressure drop per pass versus Reynolds number for various tube sizes. The pressure drop increases with decreasing tube size at equivalent Reynolds Numbers. Figure 10 shows flow rate vs. Reynolds number for various tube sizes. Lower Reynolds numbers are associated with the same flow rate as tube diameter increases. Figure 11 shows the oil temperature rise versus Reynolds number for various tube sizes. The differences here are minor, but smaller tube sizes will develop larger temperature gradients and will be more easily measured. Figure 12 shows the heat transfer ratio vs. Reynolds number for various tube sizes. As tube size decreases the heat transfer ratio increases, allowing for a cleaner salt side heat transfer calculation. Figure 13 shows heat transfer ratio vs. flow rate for various tube diameters at maximum power condition from the pump curves for three different prospective pumps. It becomes even more apparent in this figure that it is much easier to achieve high heat transfer ratios with smaller tube diameters than with larger ones. Figure 14 shows the maximum achievable Reynolds number when utilizing the smallest chosen pump vs. tube diameter.

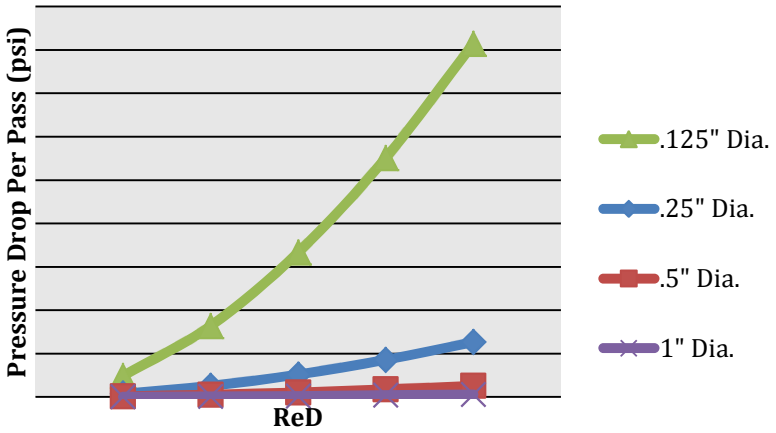

Figure 9: Therminol Pressure Drop per Pass vs. ReD for Different Tube Sizes

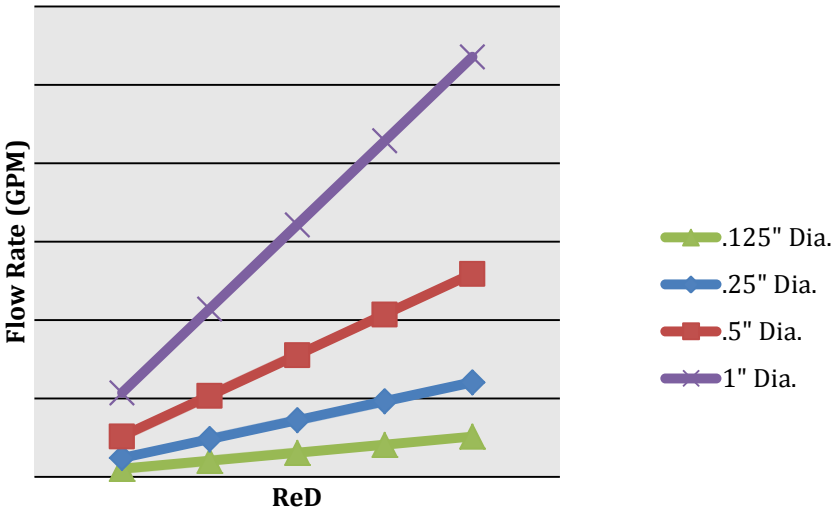

Figure 10: Therminol Flow Rate vs. ReD for Different Tube Diameters

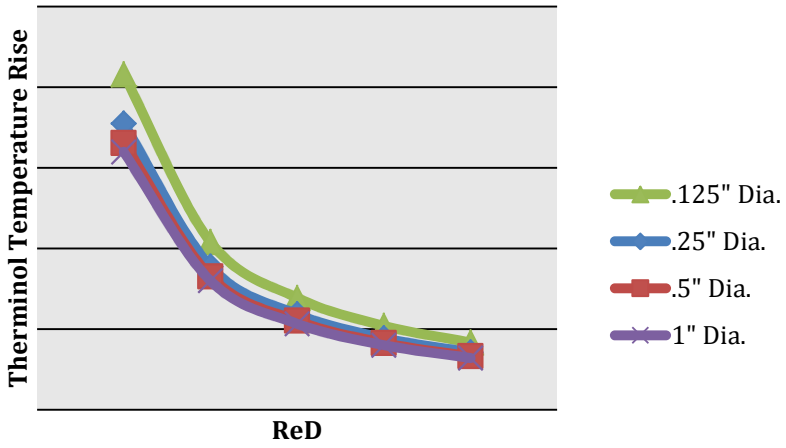

Figure 11: Therminol Temperature Rise vs. ReD for Different Tube Diameters

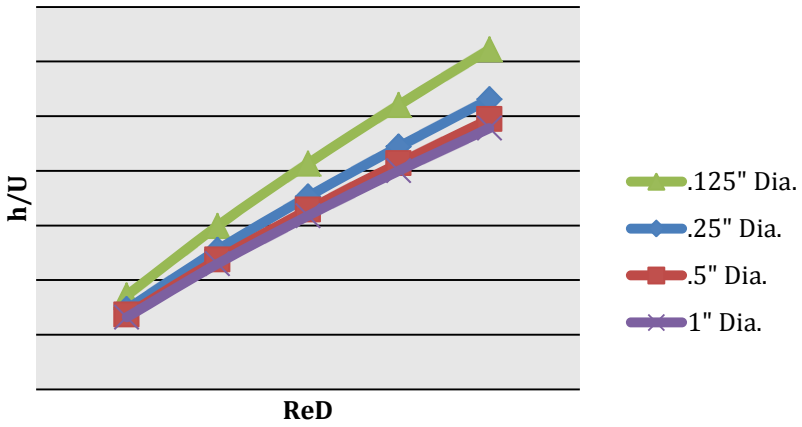

Figure 12: Heat Transfer Ratio vs. ReD for Different Tube Diameters

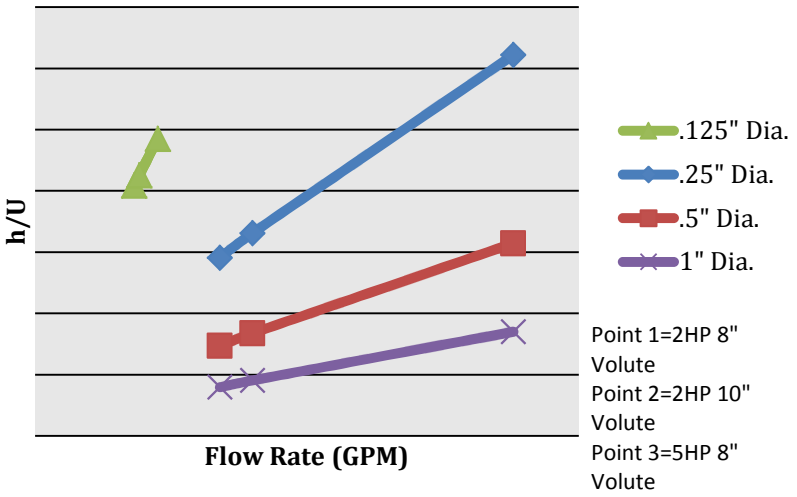

Figure 13: Heat Transfer Ratio vs. Flow Rate for Different Pumps and Different Tube Sizes

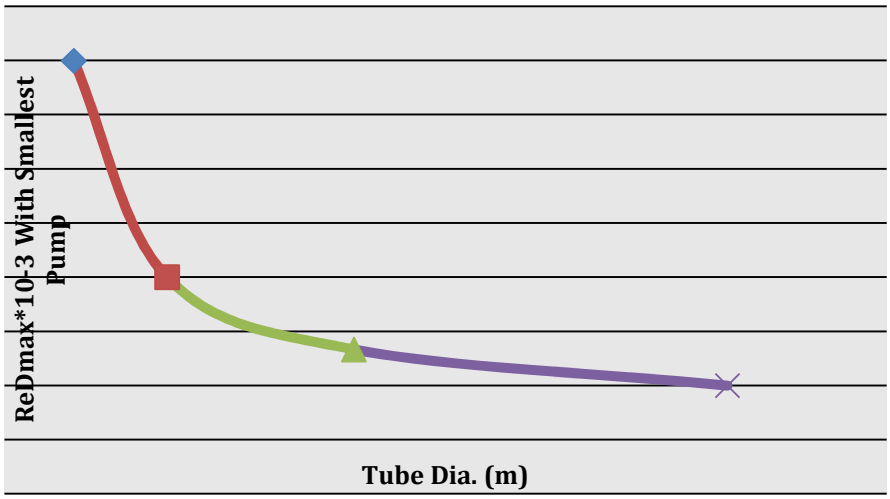

Figure 14: Therminol ReDmax Achievable With Smallest Pump vs. Tube Diameter

Table 1 shows a summary of these calculations for specific design points. The salt calculations show how the properties vary under a constant 140 GPM flow rate through the heat exchanger. For the Therminol calculations the heat transfer ratio was held to a constant of 10, and the other values were analyzed accordingly. Finally, the cooling rate and an overview of the pump calculations are tabulated.

Table 1: Tube Diameter down Selection Table

	Tube Diameter	1/8”	¼”	3/8”	1/2"	1"
Salt (140 GPM)	Pressure Drop Per Pass (psi)	740	18	8	5	2
	ReDmax at 140 GPM	43000	22000	16000	11000	5500
	ΔSolid Fraction Per Pass at 140GPM	0.02	0.04	.06	0.08	0.17
Therminol h/u=10	Pressure Drop Per Pass (psi)	1.2	0.25	.12	0.05	0.01
	GPM	8	20	30	40	80
	ΔT per pass	52	35	34	33	32
Overall	Q (kW)/Pass ΔT=10 (C)	50	100	150	200	400
8" Volute 2HP	h/u Max	40	28	22	15	7
10" Volute 2HP		43	33	25	17	9
8" Volute 5HP		49	62	47	31	17

From this information, it was decided that 3/8” was the optimum diameter to be utilized for this system. Figure 15 shows a CAD rendering of the final design. In order to get high signal to noise ratio as well as allowing for higher solid fractions, a six pass design on the salt side was chosen. A single pass design on the oil side was chosen to simplify design and protect the oil from overheating.

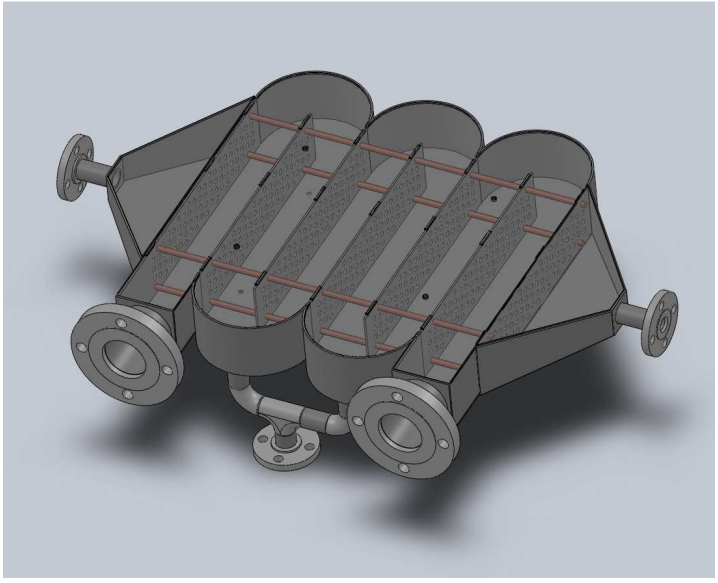

Figure 15: Rendering of Heat Exchanger CAD Design

Once the heat exchanger was designed, the rest of the system was developed to supply it. A 20 horsepower molten salt pump was purchased from Friatec©, a 2 horsepower magnetic drive hot oil pump was purchased from Dickow pumps, and Reflexx Designs was commissioned to oversee the construction of the apparatus. Figure 16 shows a rendering of the CAD model that was developed. Detailed heat loss calculations were performed in order to properly size the heating and cooling systems for the apparatus.. Once the losses were determined, a much larger heating capacity was installed on the system to allow for more dynamic operation. The final system utilizes 22 kW of heaters for the salt tank and 12 kW of heaters for the oil recirculation system. Figure 17 shows a picture of the final assembled system before final wiring and insulation. Much care had to be put in to ensure proper insulation and heating of the salt recirculation system. If the entire system is not maintained above the melting point of the salt the salt can solidify and cause blockages in the pipes. This was a major practical hurdle in the construction of the system and led to many of the delays in system operation. To monitor system readiness for operation as well as to perform the heat transfer measurements, an extensive instrument and control system was developed. Figure 18 shows a schematic of the instrumentation that was installed on the system. Figures 19 and 20 show schematics of the oil and salt systems individually. A pair of RTD's was utilized at each inlet and outlet of both recirculation systems to achieve higher accuracy at these critical measurement points. Where measurements were not as critical thermocouples were utilized due to their lower cost. A total of 19 thermocouples, 8 RTD's, and 2 flow meters were installed on the system to monitor system operation and perform heat transfer measurements. A vortex shedding flow meter from Sierra Instruments was utilized on the salt system due to its high temperature resistance and relative insensitivity to fluid properties. On the oil system a high temperature piston-style flow meter was utilized on the oil side from Lake Flow Meters.

Once the apparatus was finished, the individual system components were tested and optimized to ensure optimum performance during testing. This was an extremely intensive process due to the unpredictable nature of the system as the system undergoes thermal cycling. Many of the initial heaters failed due to warping of the salt tank, and new immersion heaters had to be retrofitted on the system to enhance the heating capacity of the system. Similarly, the Therminol system required much more heat than anticipated and therefore required an additional circulation heater to be retrofitted on the system. Furthermore, the vapor pressure of Therminol is positive at high temperature and created more fumes than anticipated. Therefore a recovery/venting system was implemented to reduce the fumes created and vent any fumes that were generated away from workers.

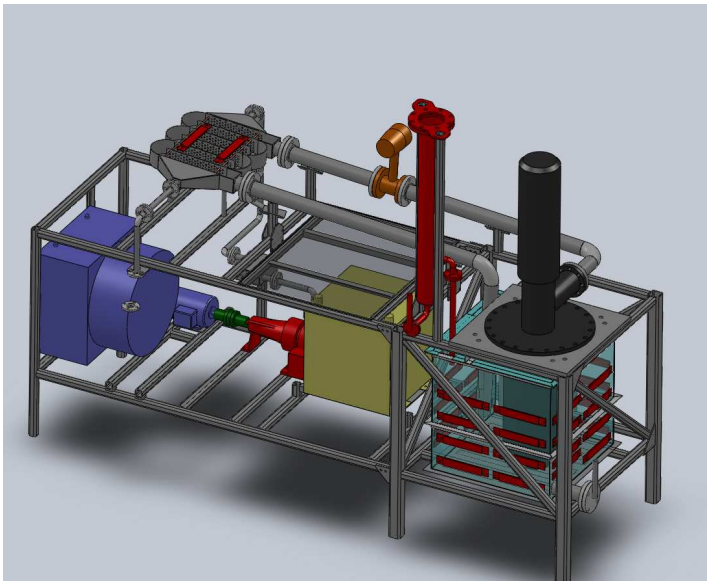

Figure 16: Rendering of Entire System CAD Design

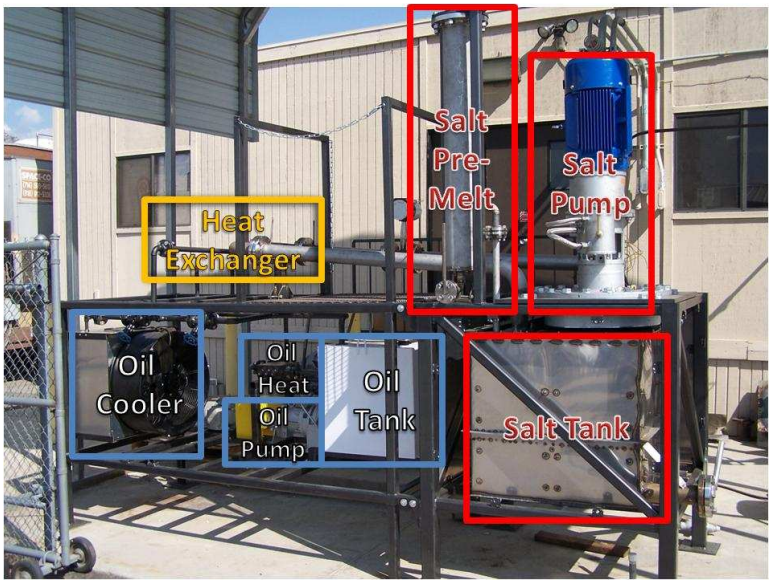

Figure 17: Image of Built System with Components Labeled

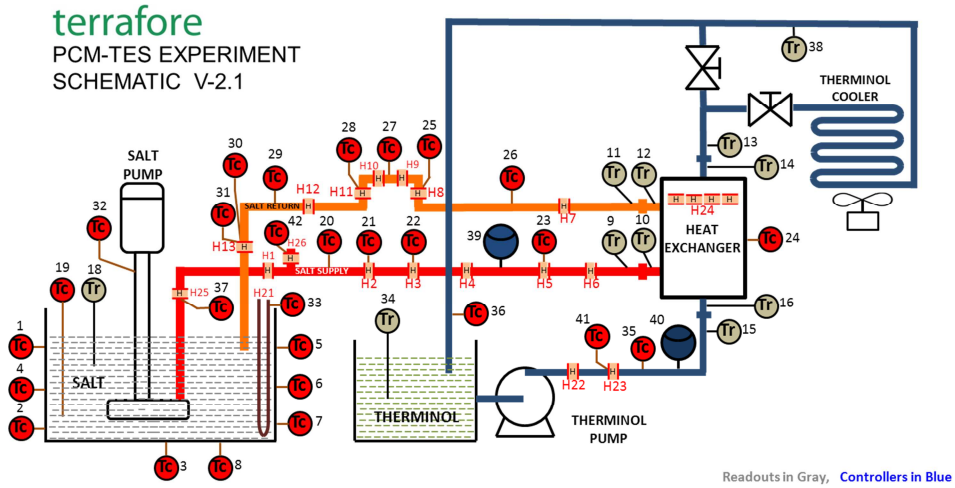

	Tc1	Upper Strip Heater TC		Tr12	HX Salt Return Near Side RTD	19	Tc24	HX Wall TC (H24)	4	Tc35	Therminol Hot TC (H22)
	Tc2	Lower Strip Heater TC		Tr13	HX Therminol Supply Far Side RTD	13	Tc25	Zone-4 TC (H7)		Tc36	Therminol Return TC
	Tc3	Bottom Strip Heater TC		Tr14	HX Therminol Supply Near Side RTD	12	Tc26	Zone-4 TC (H7-H8)	3	Tc37	Zone-1 TC (H25)
	Tc4	Salt Tank Wall TC		Tr15	HX Therminol Return Far Side RTD	14	Tc27	Zone-5 TC (H9,H10,H11)		Tr38	Therminol Cooler Return
	Tc5	Salt Tank Wall TC		Tr16	HX Therminol Return Near Side RTD	15	Tc28	Zone-5 TC (H11)		39	Salt Flow Meter
	Tc6	Salt Tank Wall TC		Tr18	Salt Tank Shallow RTD	16	Tc29	Zone-6 TC (H12-H13)		40	Therminol Flow Meter
	Tc7	Salt Tank Wall TC		Tc19	Salt Tank Deep TC	17	Tc30	Zone-6 TC (H13)	6	Tc41	Therminol Band Heaters (H23)
	Tc8	Salt Tank Bottom TC	8	Tc20	Zone-1 TC (H1-H2)		Tc31	Zone-6 TC (H13)	5	Tc42	Burst Disc Housing (H26)
	Tr9	HX Salt Supply Far Side RTD	9	Tc21	Zone-1 TC (H2)		Tc32	Salt Pump Housing TC			
	Tr10	HX Salt Supply Near Side RTD	10	Tc22	Zone-2 TC (H3)	1	Tc33	Salt Heater TC (H21)			
	Tr11	HX salt Return Far Side RTD	11	Tc23	Zone-3 TC (H5)		Tr34	Therminol Tank RTD			

Figure 18: Instrumentation Schematic for Flow Loop

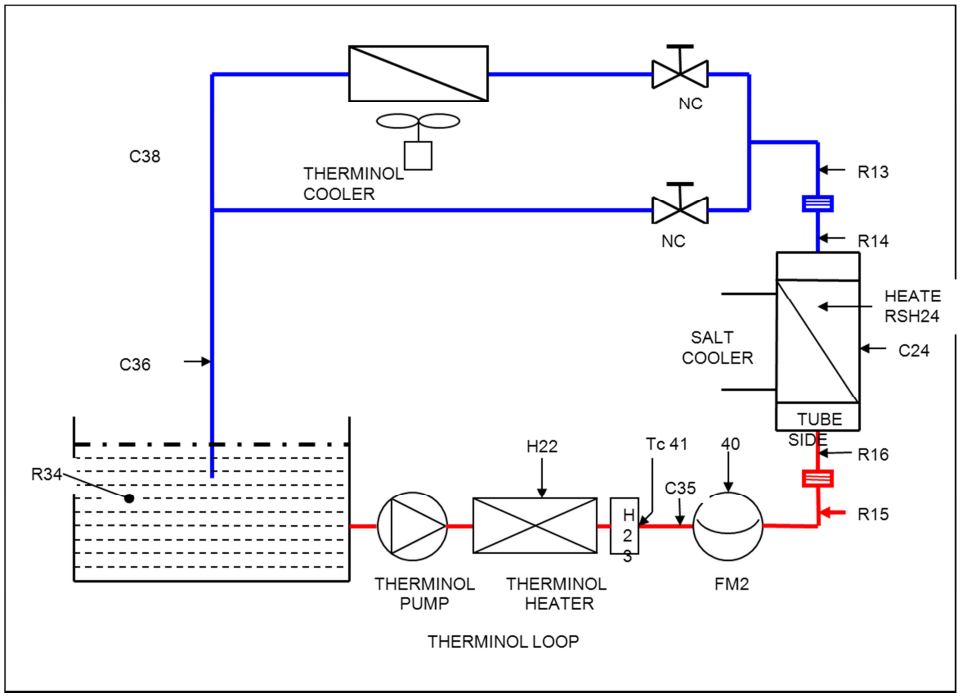

Figure 19: Therminol Loop Schematic

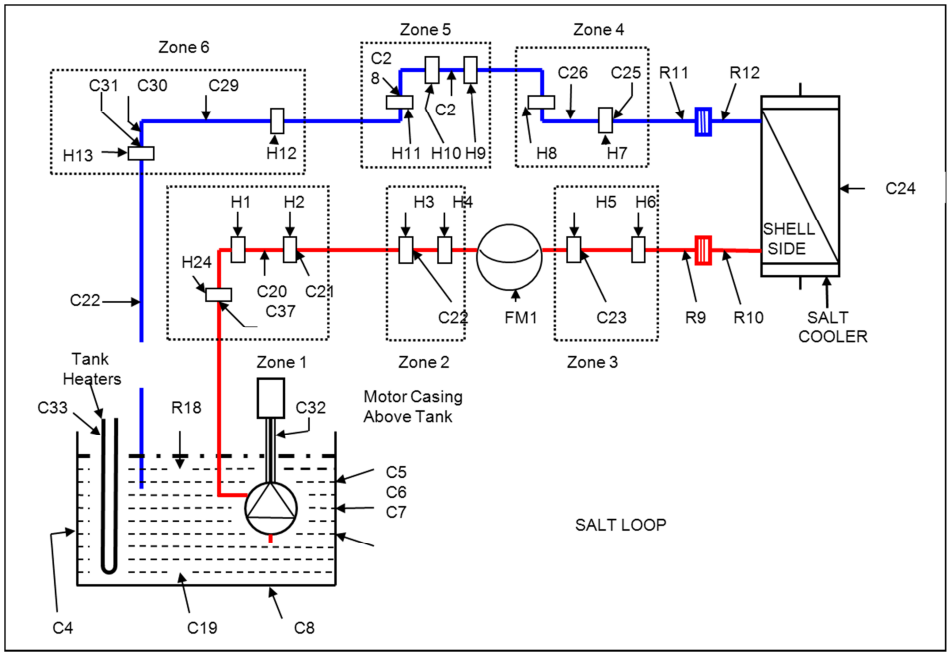

Figure 20: Salt Loop Schematic

Heat Exchanger Issues

The heat exchanger that was built per design calculations experienced many practical problems in experimentation. Tubes were initially furnace brazed into the heat exchanger, and later welded, but differential thermal expansion during the preheat process created huge thermal stresses that cracked these joints. Furthermore, melting blockages in the system can lead to huge increases in pressure, which destroyed a bellows on the system as well as causing additional failure in the heat exchanger. Because of this, a new, simpler heat exchanger was constructed to test the heat transfer properties. A CAD rendering as well as a picture of the final heat exchanger that was utilized in the system is shown in figure 21.

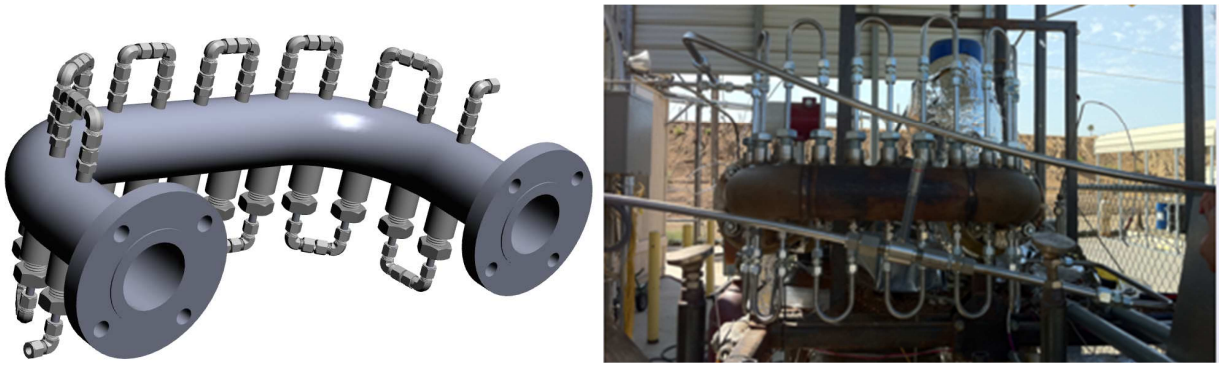

Figure 21. CAD rendering and picture of final heat exchanger utilized for experimentation.

The heat exchanger consists of a single pass on the salt side, and 13 passes on the oil side. Two RTD's were placed at both the inlet and outlet of the salt and oil in the heat exchanger. This heat exchanger design is more robust, utilizing Swagelok and valve packings to allow for more accommodation of thermal stresses. The system also allows for a much better signal to noise ratio on the oil side of the heat exchanger, allowing for better accuracy in heat transfer coefficient measurement. The heat exchanger also

has a high solid tolerance due to 84% open cross sectional area. It does suffer in terms of Reynold's number as well as maximum achievable solid fraction, but is still an excellent test bed to determine the effectiveness of the coatings utilized on the heat transfer coefficient that can be achieved.

Section 7
Experiment Results with the Laboratory Scale Prototype

Experiment Plan

- Conduct set 1 and set 2 of the planned three sets of experiments
  - Set 1 (Oil temp >salt melting point (MPt)
  - Set 2 (HX wall temp <salt MPt but salt temp > MPt)
  - Set 3 (oil temp < salt MPt and salt Temp at MPt)

Study Parameters	
Temperature of oil	various
Temperature of salt	high, medium, low
Flow rate of salt	high, low
Flow Rate of Oil	high, medium, low

Expected Outputs

Heat transfer coefficient (Ufreezesalt) as a function ofsolidification at near solification temperature
Heat transfer coefficient (Ufreezesalt) as a function of salt flow and heat transfer temperature difference
Heat transfer coeffieicent correlation from liquid molten salt
Pumpability of freezing mixture
Experience with handling high temperature molten salts near freezing point

Results of Experiments

Melting of Salt

Experiments were conducted through all three sets of proposed experiments successfully. Figure 31 shows the heat exchanger outlet salt temperature vs. the elapsed experiment time. Experiments began with an initial salt temperature of ~345 C and slowly decreased to ~302 C as the heat was extracted from the salt by the oil system (heat was utilized to help slow this process). Figure 32 shows the salt flow rate vs. the elapsed experiment time. The flow rate was modulated between 50 and 230 gallons per minute of flow rate in order to investigate the dependence of the heat transfer coefficient on the fluid velocity and reynold's number. Figure 33 shows the oil flow rate vs. elapsed experiment time. The oil flow was modulated from .6 to 1.4 gallons per minute to help determine the dependence of the overall heat transfer coefficient on the internal oil convection coefficient. Figure 34 shows the oil heat rate vs. elapsed experiment time. This varies from about 5 kW down to about 1kW as the oil and salt flow rates are varied, as well as the fact that the ΔT between the salt and oil decreases as the experiment goes on. Figure 35 shows the percent solid salt in salt tank vs. the elapsed experiment

time and figure 36 shows the percent solid salt in salt tank vs. temperature. This was calculated by a tank heat balance between heat gained from heaters and losses to the heat exchanger and environment.

Output	Oil Temperature, C (320C, 311,280,270,260, 250)	Oil Flow Rate, high=20gpm, medium=15 gpm, low=10 gpm	Salt temperature above freeze point (high=40C, med=20C, low=1C)	Salt Flow rate (high=40gpm, low=20 gpm)
liq to liq heat transfer coeff	320	high	high	high
liq to liq heat transfer coeff	320	medium	high	high
liq to liq heat transfer coeff	320	low	high	high
liq to liq heat transfer coeff	320	medium	high	low
liq to liq heat transfer coeff	311	low	high	low
solidification heat transfer coeff	311	medium	medium	low
solidification heat transfer coeff	305	medium	medium	low
solidification heat transfer coeff	300	medium	medium	low
solidification heat transfer coeff	280	medium	medium	low
solidification heat transfer coeff	270	medium	medium	low
solidification heat transfer coeff	260	medium	medium	low
solidification heat transfer coeff	260	medium	low	low
solidification heat transfer coeff	250	medium	low	high
solidification heat transfer coeff	250	medium	medium	low
solidification heat transfer coeff	320	medium	high	low
shut down mode	320	medium	heaters off	pump off
shut down mode	fan on	pump off	heaters off	pump off

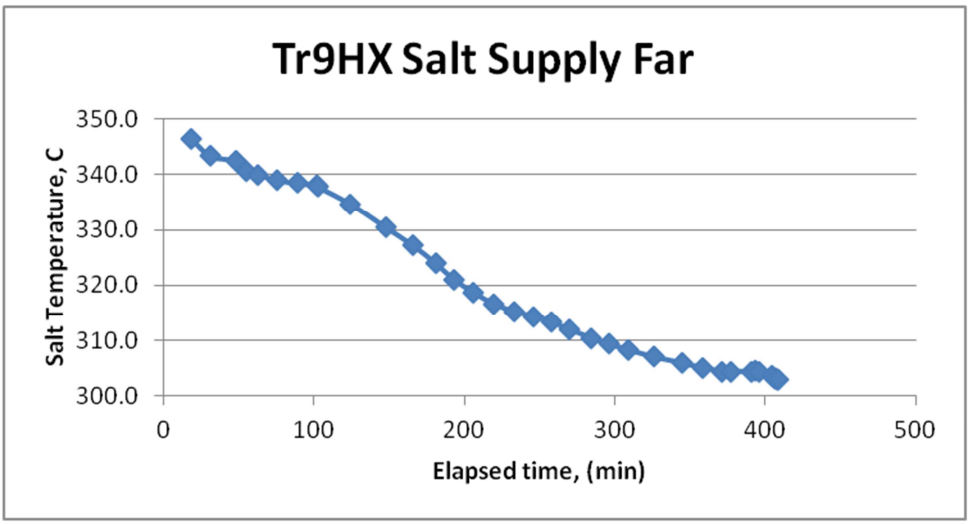

Figure 31: Heat Exchanger Outlet Salt Temperature vs. Elapsed Experiment Time

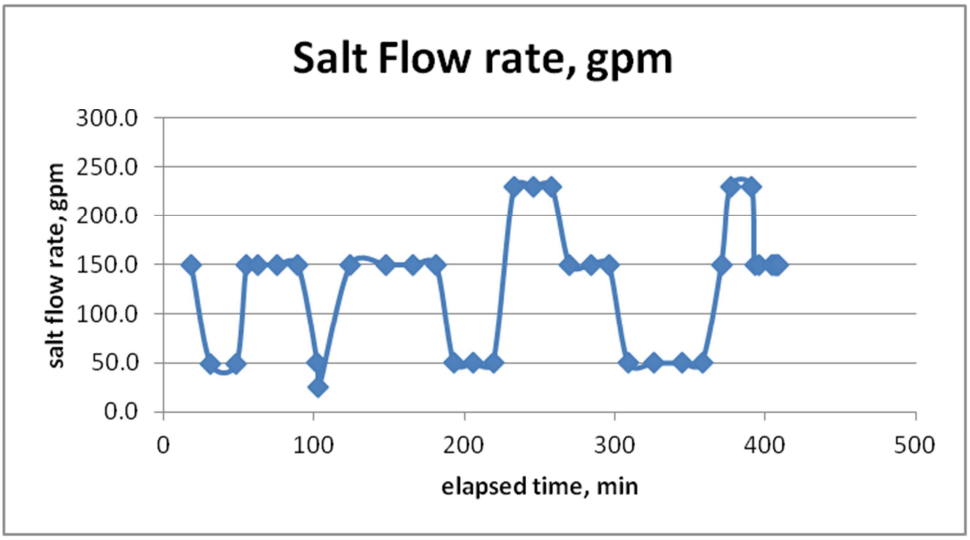

Figure 32: Salt Flow Rate vs. Elapsed Experiment Time

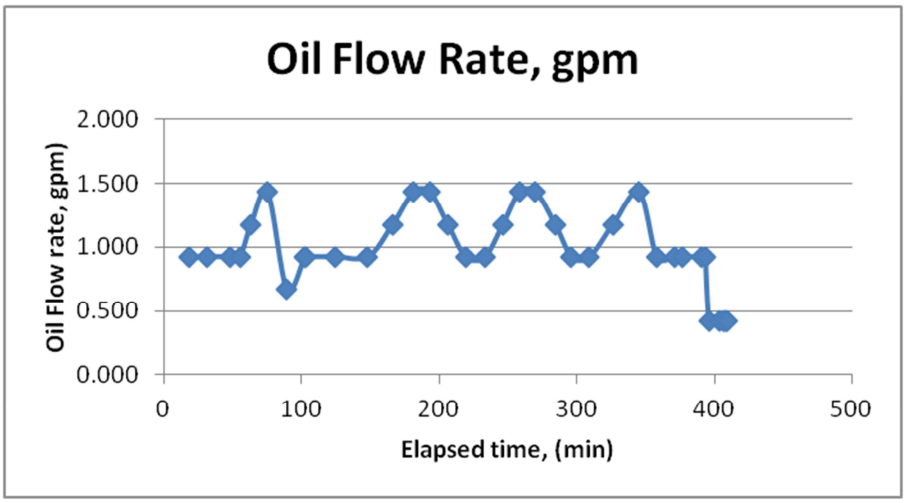

Figure 33: Oil Flow Rate vs. Elapsed Experiment Time

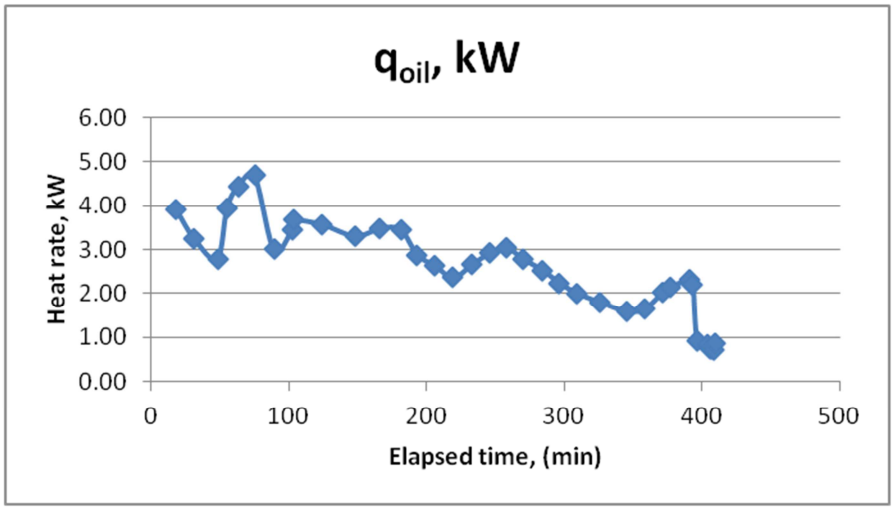

Figure 34: Oil Heat Rate vs. Elapsed Experiment Time

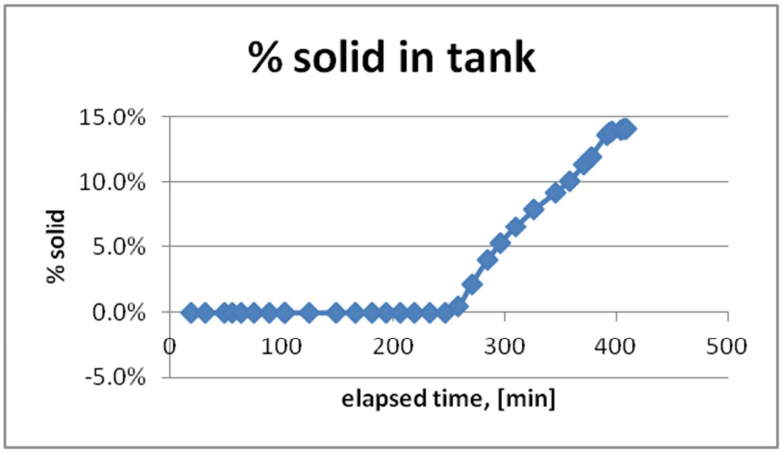

Figure 35: Percent Solid Salt in Salt Tank vs. Elapsed Experiment Time

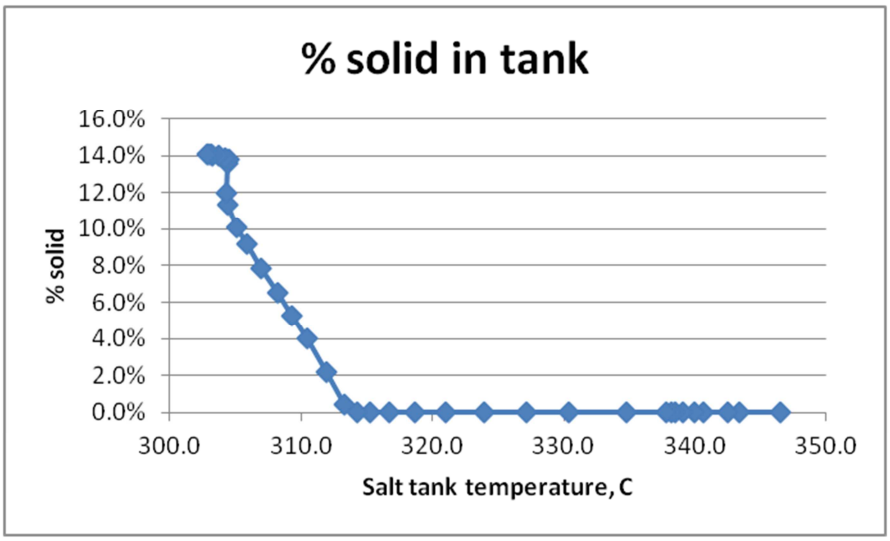

Figure 36: Percent Solid Salt in Salt Tank vs. Salt Temperature

Figure 37 shows the overall heat transfer coefficient, U, vs. salt temperature. It ranges from values as high as 2400 W/m^2K above the melting point at high salt flow rates, to around 500 W/m^2 K at the salt melting point. Figure 38 shows the predicted salt thickness on the heat exchanger tubes vs. temperature. This was calculated utilizing the math model to be presented later, but is a calculated measure of how thick the salt layer on the surface should be to produce a given heat transfer coefficient. Using this, the salt thickness on the tubes was calculated for the given heat transfer properties from the experimental data. Figure 39 shows the calculated salt thickness on the heat exchanger tubes vs. temperature and figure 40 shows shows the calculated salt thickness on the heat exchanger tubes vs. elapsed experiment time. This data can be summarized in figures 41 and 42. Figure 41 shows the overall heat transfer coefficient vs. temperature at different salt flow rates. We can see that for temperatures above the melting point (~308-310^{o}C) we achieve very high heat transfer rates around ~1600 W/m^2 K. This number drops

dramatically as we near the solidification temperature (~303 ^{o}C) to ~1050 W/m^2 K. Figure 42 shows the overall heat transfer coefficient vs. salt flow rate at different temperatures. This graph shows that the heat transfer coefficient is relatively unaffected by flow rate at these low Reynold's numbers, and is dominated more by temperature.

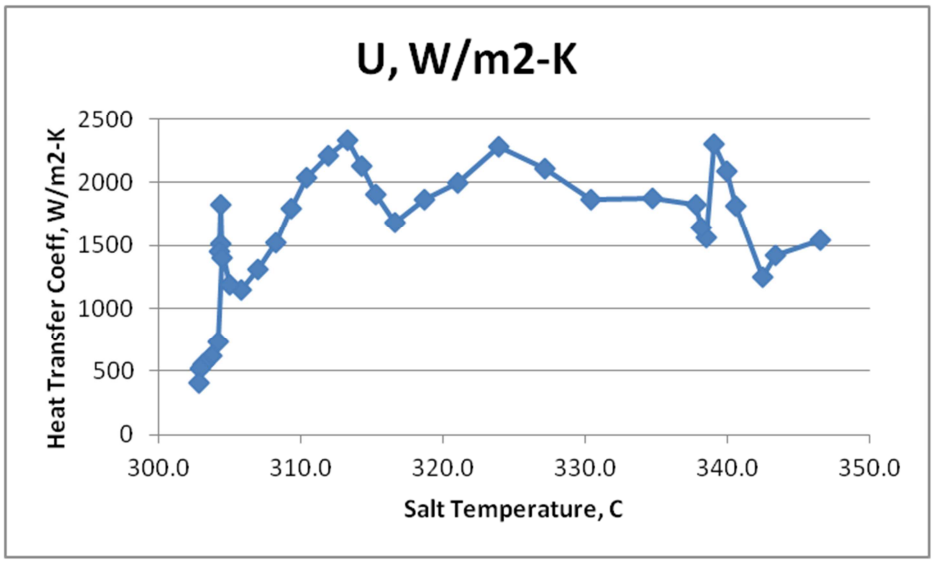

Figure 37: Overall Heat Transfer Coefficient vs. Salt Temperature

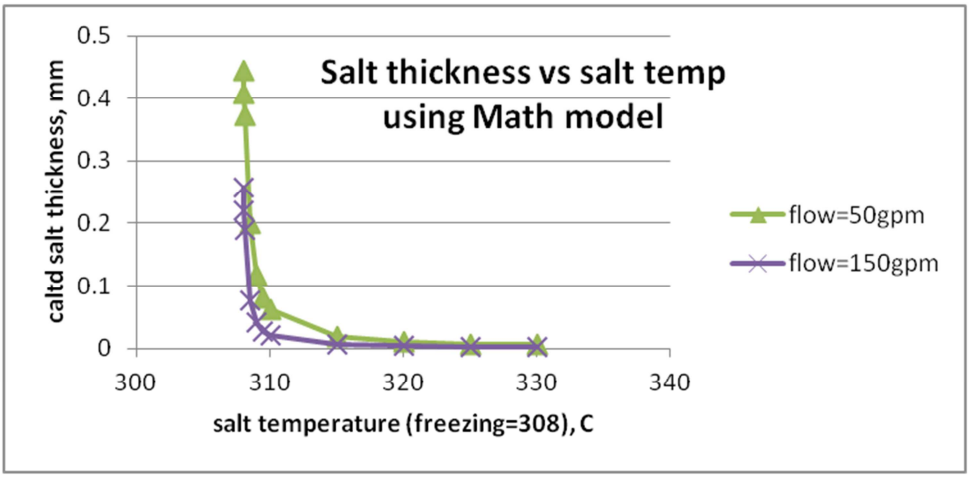

Figure 38: Calculated Salt Thickness vs. Salt Temperature by Math Model

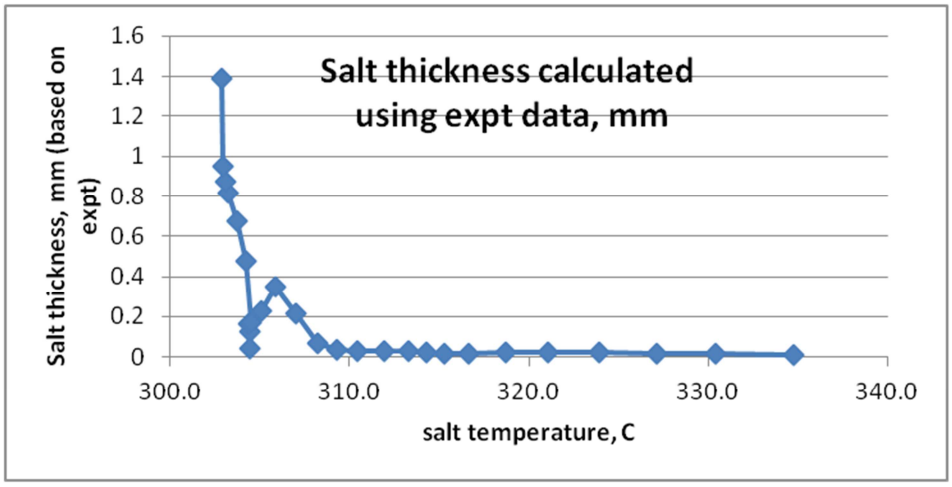

Figure 38: Calculated Salt Thickness vs. Salt Temperature by Experimental Data

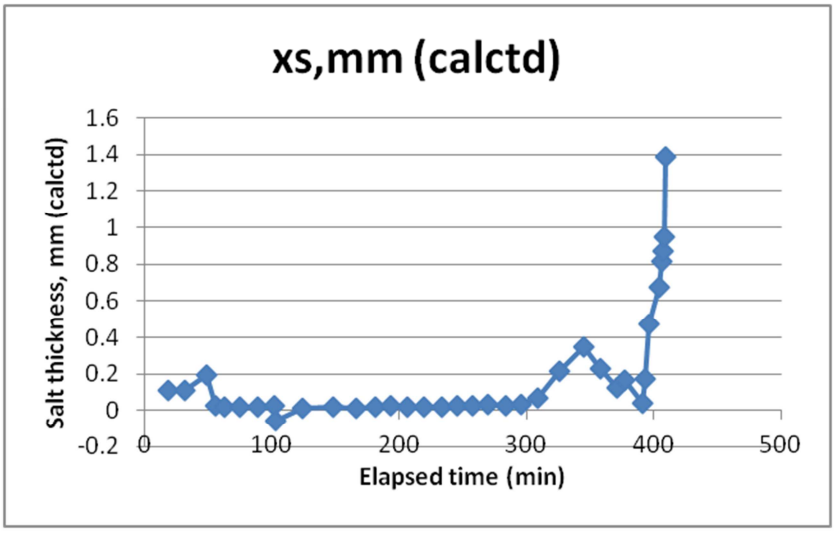

Figure 40: Calculated Salt Thickness vs. Elapsed Experiment Time

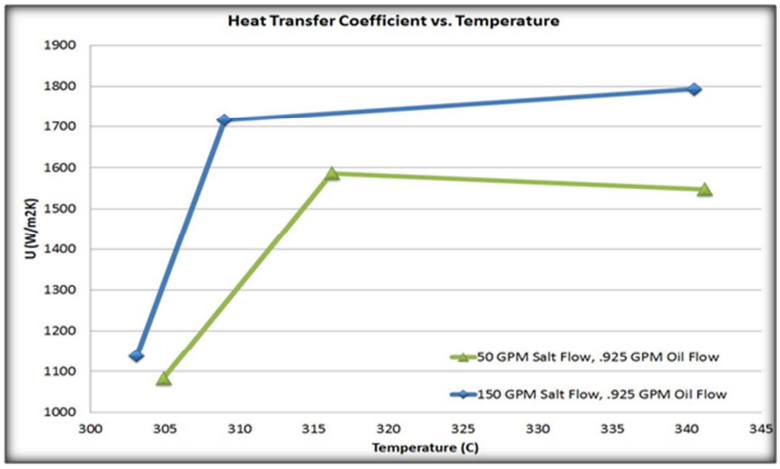

Figure 41: Overall Heat Transfer Coefficient vs. Temperature at Different Flow Rates

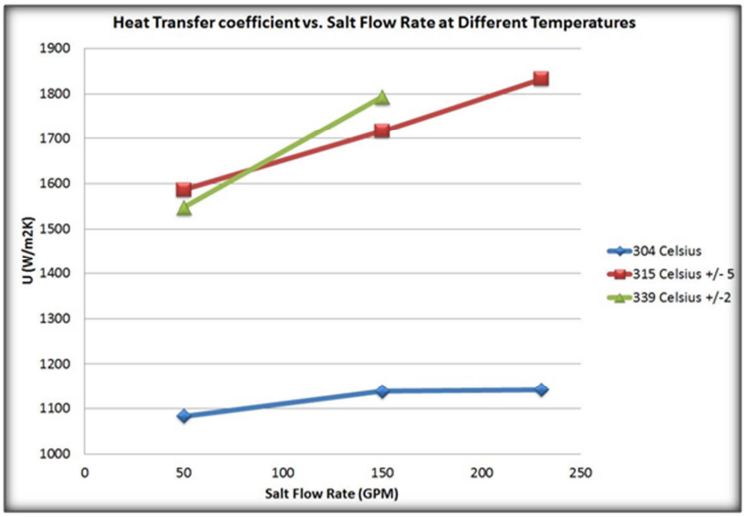

Figure 42: Overall Heat Transfer Coefficient vs. Salt Flow Rate at Different Temperatures

Section 8.
Economic Analysis of PCM-TES with CSP

The LCOE objective can be achieved by the following three factors:

- Technical Improvements from efficient and optimized systems
- Economy of Scale cost reduction due to increased size
- Volume Production discounts resulting from construction of multiple plants, or from procurement of multiple subcomponent parts.

The primary reduction in LCOE of this project will be due to the first bullet: technical improvement resulting from reduced use of salt, smaller container size and from improved turbine efficiency.

Figure 8-1 illustrates the impact of heat of fusion and salt costs on total TES cost. The total TES cost is sum of capacity cost and rate-related costs. The TES cost shown in Figure 8-1 is relative cost and is based on assumed data on costs of heat exchangers, tank and balance of plant.

Capacity Costs ~ 1/Heat of fusion of salt

Rate-Related Cost ~ $1/\sqrt{\ }$ (Thermal conductivity X Heat of Fusion)

The capacity-related costs are inversely proportional to the heat of fusion while the rate-related costs depends on the heat exchanger area required and is inversely proportional to the square root of heat of fusion multiplied by the thermal conductivity of the selected salt.

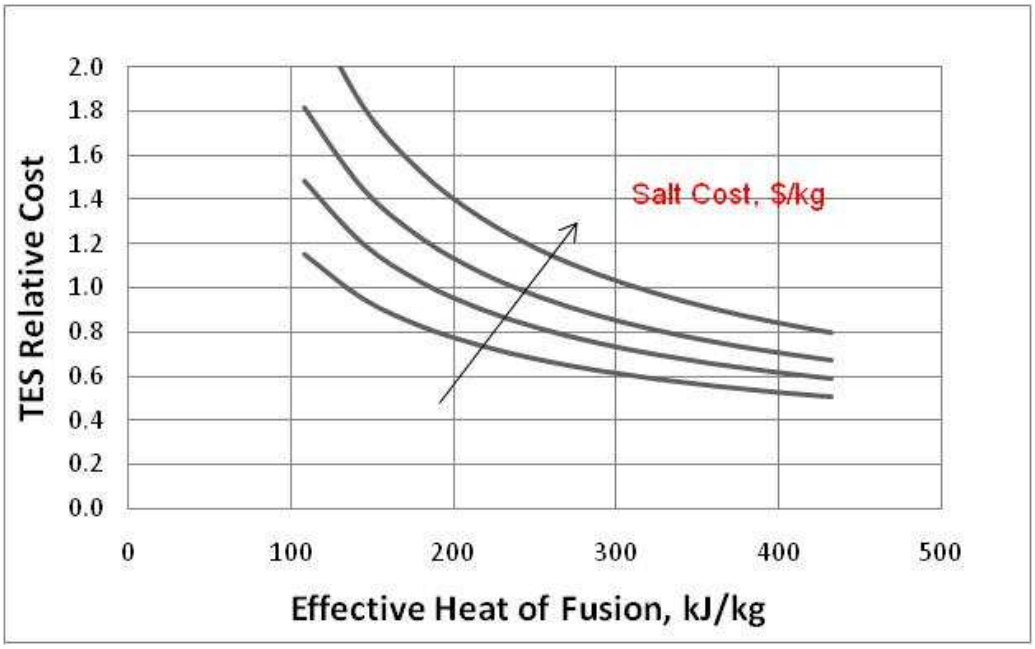

Figure 8-1

The economic analysis uses a nitrate as the baseline salt for calculations.

Benefits of active heat exchange PCM TES

When compared to a two-tank conventional sensible heat TES, the PCM –TES:

- Reduces the amount of salt required by 8% for a 6 hour storage
- Improves CSP plant system efficiency by 0.9% because TES can be charged with lower receiver temperature (450^{o}C instead of 550^{o}C) during periods of low solar flux. The heat is used to melt the salt and bypass the high temperature heat exchanger (see figure 8-2)
    - Simulations using power tower model (PWR) calculate an overall improvement in annual system efficiency of 0.88% or a reduction of 0.88% in system cost for same annual energy. Since TES costs are 10% of the system cost, this represents 8.8% reduction in equivalent costs assignable to TES.
- Uses a single container with actively managed thermal stratification to provide for superheat and vaporization of water. This eliminates the need for the lower cost carbon steel tank.

Additional costs of active heat exchange TES

- Custom design of heat exchanger using coated tubes.
- Additional molten salt pump to pump fluid from storage tank through the high temperature heat exchanger during charge
- Additional charge cycle heat exchanger to transfer heat from receiver heat transfer fluid to storage fluid.

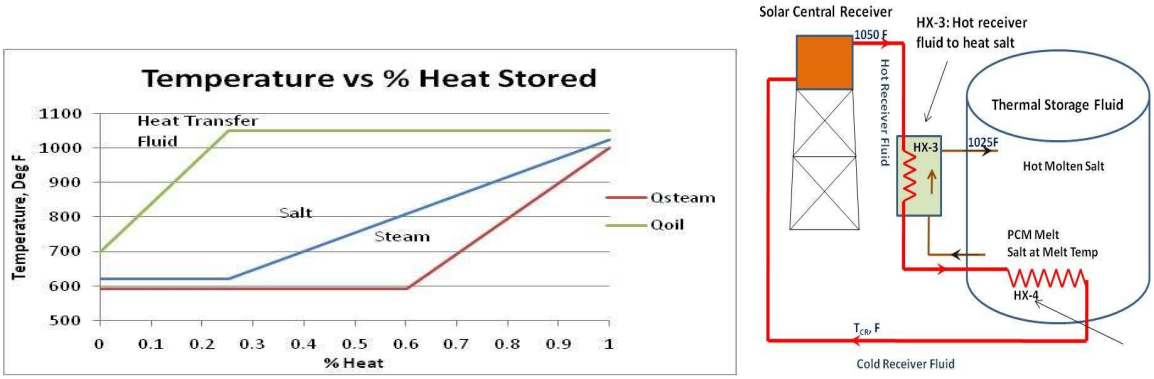

Figure 8-2. Heat transfer fluid temperature for charging TES need not be constant

Table 8-1 shows the estimates of dollar savings with the active heat exchange PCM-TES when compared to a two-tank sensible heat exchange system for two different solidification percentages (even though we used absolute costs, the table should be used for comparing costs between systems). Our goal was to achieve 40% solidification. However, we project we can achieve15%. The table shows costs for both these cases.The conventional sensible heat storage system is a two-tank TES using molten salt as heat transfer and storage fluid, storing heat between 550 ^{o}C and 330 ^{o}C. The heat exchangers are sized to provide heat rate to generate100MWe during discharge. The additional cost due to lower heat transfer coefficient and special coating for the steam generating power block heat exchangers, is included in the PCM-TES columns. The cost of the heat exchanger is assumed to be 25% more for PCM-TES than the nominal cost for a shell and tube heat exchanger in 2-Tank system. Also, PCM-TES system requires

additional heat tracing on piping to and from the heat exchangers, which is assumed to be 5% of the total cost of the system.

The TES cost savings with 15% solidification is 9% whereas for 40% solidification, the net benefit can be up to 21%. However, including the credit for improved system efficiency assignable to PCM-TES the expected savings are 30% and 17% over the two-tank TES for the 40% and 15% solidification respectively.

Even though, we demonstrated that solidifying *a dilute eutectic over coated tubes* can improve heat transfer and reduce the amount of salt used, the savings for the 15% solidification PCM-TES are at best marginal. This is because there are uncertainties in the additional parasitic energy for pumping the high viscosity salt slurry and parasitic energy for additional heat tracing which will increase the operational cost.

Table 8-1 Comparison of Benefits and Costs with PCM-TES and 2- Tank Sensible TES

Solidification %	%		0%	40%	15%
	$/kWht		**$ 28.20**	**$ 22.35**	**$ 25.79**
			2-Tank Sensible 287C to 550C	**1- Tank Active HX TES 300 C to 550C**	**1- Tank Active HX TES 300 C to 550 C**
			263	**250**	**250**
Qsto	MWHt		2000	2000	2000
Delta T	deg F		473.4	450	450
Latent Heat	Btu/lb		0	34	12.75
% volume solid	%		0%	0%	0%
% available volume	%		90%	95%	95%
Specific heat	Btu/ft3/F		45.6	45.6	45.6
Specific heat	Btu/lb/F		0.380	0.380	0.380
Specific store capacity	Btu/ft3		19428	23574	21024
Specific store capacity	Btu/lb		161.9	194.8	174.6
Effective Specific heat	Btu/lb/F		0.34	0.43	0.39
Lbs of Media	lbs		42,148,746	35,039,795	39,092,016
Vol of Media	ft3		351,240	289,471	324,581
No. of tanks			2	1	1
H/D			0.5	0.5	0.5
Diameter (Max=150)	ft		76	94	99
Height (Max=42)	ft		38	42	42
Foundation area	ft2		9107	6892	7728
Surface area	ft2		18213	19253	20817
Pressure at tank bottom	psi		32	35	35
thickness avg	ft		0.334	0.382	0.393
2 tank or 1 tank cost factor (1 for SS tank, 1.65 for SS+Carbon steel tank	est		1.65	1	1
Lbs of steel	lbs		8,034,791	3,996,485	4,485,876
Learning factor			0.81	0.81	0.81
Storage Tank cost			$ 16,968,323	$ 8,440,002	$ 9,473,526

Insulation Cost	$/ft2	30	$ 546,403	$ 577,577	$ 624,500
Surge Tanks	% of tank	3%	$ 509,050	$ 253,200	$ 284,206
Foundation costs	$/ft2	350	$ 3,187,351	$ 2,412,262	$ 2,704,845
Pumps	est	25%	$ 4,242,081	$ 4,242,081	$ 4,242,081
Interconnection pipes		10%	$ 1,696,832	$ 844,000	$ 947,353
Instrumentation & Controls		2%	$ 543,001	$ 335,382	$ 365,530
Total	$		$ 27,693,041	$ 17,104,505	$ 18,642,040
Coated tube HX, Additional charge HX	est		-	$ 3,600,000	$ 6,100,000
Salt	$/lb	$ 0.53	$ 22,338,835	$ 18,410,384	$ 20,643,379
Other Misc (Contingency)	% total	5%	$ 1,384,652	$ 855,225	$ 932,102
additional for heat tracing	5% total	5%	$ -	$ 855,225	$ 932,102
Direct Total			**$ 51,416,528**	**$ 40,825,340**	**$ 47,249,623**
Indirect					
Sales Tax (8.75% on material)		8.75%	$ 3,447,632	$ 2,644,895	$ 2,918,162
Engineering - (3% of direct)		3%	$ 1,542,496	$ 1,224,760	$ 1,417,489
Total Cost of TES			**$ 56,406,656**	**$ 44,694,995**	**$ 51,585,274**
Specific Costs	$/kWht		$ 28.20	$ 22.35	$ 25.79
Relative Cost			100%	79%	91%
Savings				**21%**	**9%**
0.88% improvement in System Efficiency credit for lower temp charging				8.80%	8.80%
Expected Total Savings				29.6%	17.3%

Section 9.
Lessons Learned
Design Considerations for Molten Salt Thermal Storage

Several lessons were learnt in the design, building and operating of the two flow loop systems. The fact that these systems were operating close to the salt freezing point presented some foreseen and unforeseen challenges.

Lessons learnt from Phase 1 Flow Loop:

- First melt of salt in granular form versus subsequent melts when it is a solid mass have to be handled entirely differently. The first time melt needs to be managed to account for inefficient heat transfer from heating surfaces to salt, extra heating time as a result and gradual charging of salt to avoid air pockets and ensure homogeneous molten liquid formation.
- Once the required quantity of salt is melted, it is very important to keep the salt in the molten state for the longest duration possible, preferably until the series of experiments is completed, so as to avoid the complications mentioned below.
- Subsequent melts have to be handled with extreme care. When frozen salt in a tank and pipes is required to be melted, the process of melting needs to start from the salt surfaces exposed to the atmosphere. In other words, the surface of the salt should be melted first and proceeding gradually to the inside. Due to practical considerations of heater placement this is not always possible. Typically heaters are attached to the surface of the tank and pipes and heating starts at those surfaces. As the salt melts at these surfaces its volume expands and pressure pockets are created leading to explosions. There were two such blowouts in the Phase 1 Flow Loop. Safety precautions prevented any damage to property or personnel.
- In the event that it becomes necessary to shut down the flow loop prior to the completion of experiments, a salt drainage system is necessary that can quickly drain the molten salt from the system prior to shut down.
- It is important to drain all pipes and fittings of molten salt after each experiment to prevent solidification. Any solid salt formation in pipes and fittings presents serious challenges to safe re-melting.

Lessons learnt from Phase 2 Flow Loop:

- Salt Melting System for first time melting of salt should be designed to ensure easy flow of melted salt into the molten salt tank. The entire salt flow path should be adequately heated to prevent any freeze ups. The heating system should be designed for maximum hot surface area to be in contact with salt. Heaters should be chosen to ensure best possible contact with the pre-melt tank and be able to withstand hot spots that develop.
- Heat exchangers and all other salt flow paths should be designed to safely withstand the maximum system pressures that might develop in case of freeze ups in the salt flow path.
- Since the salt flow path is designed to automatically drain the salt into the tank at the end of each experiment, there may be a possibility of air locks building up. A suitable vent system should be in place to take care of such a possibility.

- Immersion Heaters are preferred over tank surface heaters.
- Heater placement should be designed for easy replacement in case of failures.
- The system should be designed to keep the salt molten for the entire duration of operation.
- In case of unscheduled system shut downs, salt may freeze and it may become necessary to re-melt the frozen salt in the tank. To facilitate re-melting, immersion heaters should be placed so as to heat the salt so that the salt at the top melts first. This will prevent excessive pressure build-ups.
- Care should be taken to ensure that temperatures of heater surfaces not immersed in salt do not exceed safe levels and also levels that might decompose salt.
- Significant conduction losses occur through the body of the salt pump and the discharge and return pipes. Sufficient trace heating should be provided as close to salt level as safely possible to account for such heat losses and prevent freeze ups.
- Temperatures of salt should be monitored in as many locations in the tank as possible.
- A stirring should be considered for periodic slow stirring of salt in the tank to ensure uniform temperature.
- All piping should be adequately heat traced. This is extremely important if pipes with a low thermal conductivity material such as stainless steel are used.
- Temperatures of the entire salt flow path should be monitored at as many points as possible.
- Prior to starting the salt flow, every time, the salt flow path should be checked to ensure that there are no freeze ups or blockages. This can be done with a simple pressure test using air.
- Emergency procedures to shutdown the system should be in place. A *single emergency shutdown* actuator (button) that will simultaneously shutoff pumps, close or open relevant valves, turn on or off heaters etc should be provided at multiple locations in the plant.
- Salt re-melt procedures in case of unforeseen shut downs should be in place. Due consideration should be given to salt melt process so that it melts from the top and no pressure pockets are formed inside the frozen salt block.
- Safety procedures for operation of the system should be in place. All system conditions should be foreseen and accounted for to the extent possible. A thorough Failure Mode Effect Analysis (FMEA) must be conducted with all operating personnel in attendance.

Appendices

To

Sections

Appendix 1
Eutectic Phase Diagrams

By
Mehrnoush Zare

Phase Diagram and Heat of Fusion Calculations

In Table 3, we list the heat of fusion of eutectic salt mixtures that are major components. The procedure described below is used to calculate the heat of fusion and freezing point depression for the salt mixture consisting of the major and minor components. Appendix C shows the procedure for calculating the heat of fusion and freezing point depression for a few selected salt mixtures. The phase diagrams for some salt systems are available in literature (ref : Tohoku database). Appendix D shows some of the phase diagrams and calculation procedure.

In order to obtain the maximum mass percentage of the first solidified salt which can be released during the solidification process at any temperature range, one can take advantage of the lever rule. This can also be used to determine the amount of latent heat of fusion by multiplying the percentage of solidification with the latent heat of the solidified salt, and adding the sensible heat due to the freezing point depression to the final solidification point.

The best binary would have a small liquidus slope at the solute rich- side of the diagram. This can be determined by simply determining the slope from the A-B diagram. We introduce a term called *effectivity index* to compare different salt systems with each other:

$$effectivity\ index = \frac{effective\ latent\ heat}{slope\ of\ the\ liquidus\ line\ in\ phase\ diagram}$$

Therefore the higher the effectivity index, the better the salt mixture as a PCM, since it stores and releases more latent heat and its liquidus slope is relatively lower.

Another approach would be to calculate the freezing point depression of the solvent A by the addition of the solute B. Freezing-point depression describes the phenomenon that the freezing point of a liquid (a solvent) is depressed when another compound is added, meaning that a solution has a lower freezing point than a pure solvent. This happens whenever a solute is added to a pure solvent. The freezing point depression is a colligative property, which means that it is dependent on the presence of dissolved particles and their number, but not their identity. It is an effect of the dilution of the solvent in the presence of a solute. It is a phenomenon that happens for all solutes in all solutions, even in ideal solutions, and does not depend on any specific solute-solvent interactions.

The extent of freezing-point depression can be calculated by applying Clausius-Clapeyron relation and Raoult's law together with the assumption of the non-solubility of the solute in the solid solvent. The equation is $\Delta T = R (T_m)^2 X_n / L$, where X_n is mole fraction and L is the heat of fusion. This will give us a quantitative selection parameter that approximately follows the calculated slope values.

The equation can also be shown as $\Delta T = K_c X_n$, where $K_c = R (T_m)^2/L$ is called the cryoscopic constant. The technique for determining the molecular weight of a solute by dissolving a known quantity of it in a solvent and recording the amount by which the freezing point of the solvent drops, is called cryoscopy.

Therefore the phase diagram calculations were done for each 10 systems in table 1. First the amount of molar solidification percentage was calculated when cooling down from 350°C to 270°C. Then the same thing was calculated while cooling down from 290°C to 270°C in order to obtain the amount of solidification with approximately 20°C temperature depression. Mass percentage of solidification was determined using the below equation:

If the initial composition of the salt is xA0 and xB0, then the composition of the salt after mass% of solidification is:

$$Mass\% = \frac{x_A \times mW_A}{x_A \times mW_A + x_B \times mW_B}$$

Where x_A and x_B are the molar percentages of A and B and $mW_A and\ mW_B$ are molar masses of A and B respectively. The effective latent heat, slope of the liquidus line, effectivity index, cryoscopic constant and sensible heat release were also calculated for each system.

For the ternary systems one can assume a binary eutectic composition as a single salt phase with the melting temperature of the eutectic point and the latent heat obtained by the rule of mixture. By adding a small amount of the third salt, the amount of temperature depression will be calculated like the binary systems from the equation: $\Delta T = R (T_m)^2 X_n /L$

Therefore, for the ternary systems melting temperature will be the eutectic temperature for the major binary salts and latent heat is obtained by the rule of mixture at the eutectic composition. The cryoscopic constant was also calculated for the ternary systems.

Viscosity of the semi-solid salt mixtures

The rheological behavior of partially solidified salt mixtures to be used in solar power plants is our interest. It is known that in the early stages of solidification, shrinkage is compensated for the simultaneous movement of liquid and solid. This can be called mass feeding. At later stages of solidification the growing dendrites form a continuous skeleton within the liquid-solid zone. As cooling continues, this skeleton is subjected to strain from thermal contraction and this strain can be highly localized. Within local regions of high strain, bonds between dendrites and dendrite arms are broken and dendrites separate.

Vigorous agitation of a molten salt mixture however postpones the formation of a continuous solid network to much higher fraction solid. With this agitation we can make the mixture to behave as thixotropic slurry to fractions of solid up to 50%. Being thixotropic means to become as less viscose as the fluid itself when stirred or shaken and returning to a semi-solid state when allowed to stand.

Apparent viscosity of slurries increases with increasing solid concentration. Therefore solid fraction plays an important role in semi-solid. Cooling rate is another important factor. By decreasing temperature, the viscosity of the semi-solid will increase faster. Dendrite network will be formed faster in this situation in absence of a stirring system.

In the presence of the stirring system the below equation in introduced for simple Newtonian fluids:

$$Viscosity = \frac{Shear\ Stress}{Shear\ Rate}$$

In rheocasting or simply stirring the melt, there is a fixed amount of force applied, therefore when shear rate increases, the viscosity decreases. This is significant in the current research for the ease of pumping the semi-solid salt mixture through the heat exchanger tubes and pumping the high fraction semi-solid out of the heat exchanger tubes to the main tank.

Collected data for a variety of dispersed Newtonian suspensions are shown in figure 1. As it can be seen the apparent viscosity between "0.4 to 0.6" of solid fraction, increases to very high values. When plotted as relative viscosity versus fraction solid, all the data fall on the same general curve regardless of material. If we assume that our solid particles in semi-solid salt mixture are also spherical in shape with the range of diameter between 0.099 to 435 Microns, as it is for the particles in the figure 4, we can use the same values to estimate a bulk figure for the changing of the viscosity in salt mixture by solid fraction.

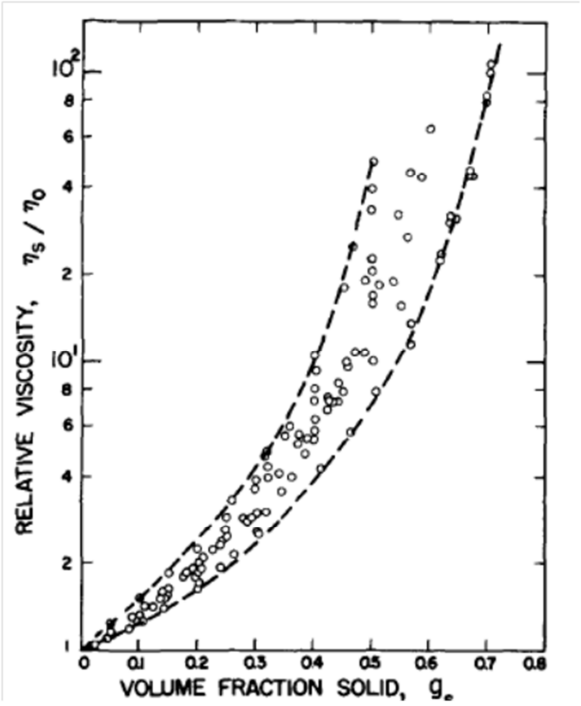

Figure 1. Collected viscosity data of dispersed suspensions of uniform spherical particles. The particle materials included polystyrene, rubber latex, glass, and methyl methacrylate. η_s is the viscosity of the slurry while η_o is the viscosity of the suspending medium [D.B. Spencer, et al, MMT, vol.3 (1973)]

Temperature change is also another factor to be considered. Let us assume a binary salt system A-B which by decreasing the temperature below the liquidus line, salt B starts to solidify first. Because of the temperature depression, there will be an increase on the viscosity of the liquid phase itself ignoring the solid fraction. So there will be a relationship between temperature and viscosity. Also by increasing the solid particles there will be a relationship between solid fraction and viscosity, which is indicated in figure 1. Because the solid fraction is also related to temperature according to the binary system's phase diagram, therefore by combining these two relationships, we can better determine the viscosity change of the salt mixture during the solidification.

It is also to be mentioned that the liquid phase is a molten salt mixture. Therefore by decreasing the temperature the percentage of the saluted salt is decreasing in the liquid phase, and this will cause a

deviation from the viscosity data in the liquid phase. So for accurate viscosity data experimental methods seem to be necessary. However we could estimate the change of the viscosity by temperature decrease and solute increase by doing some simple calculations. These calculations are done for each binary system below, and the results are compared between for systems at the end. The relative viscosity data in figure 4 assumed to be increasing exponentially by increasing the solute as solid particles, as it can be seen in the below equation:

$$\eta = \eta_o \exp(s\%) \ [CP]$$

Measuring viscosity at or near freezing or melting temperature is challenging. Figure 2 shows the viscosity of sodium nitrate salt near melting temperatures (300 to 308 C). These measurements were at conducted at NREL by Dr. Anne Starace.

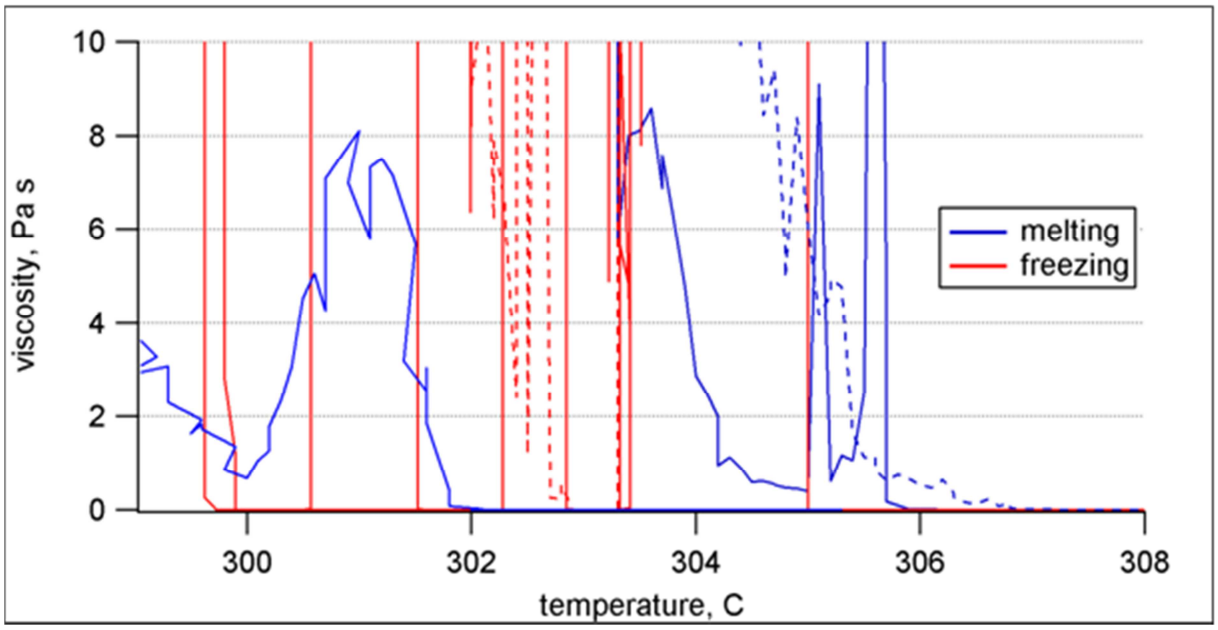

Figure 2. Measurement of viscosity near freezing and melting temperatures for NaNO3
(courtesy Dr. Anne Starace Scientist NREL)

Considerations in Selecting Salt Mixtures

Dr. H. Venkatasetty

Nucleation and Crystallization

Super-cooling of melts, which precludes crystallization and heat release, is one of the problems in the selection of suitable thermal energy storage materials. Our experience shows that the phase–change processes (heating and cooling) do not occur instantaneously as expected. However, the process can be hastened by using suitable nucleating agents. We believe that in large storage systems we are considering for this project, it becomes even more important to identify suitable nucleating agents and conduct preliminary experiments.

Although this problem is well documented in the literature, not much is known on promising nucleating agents for accelerating nucleation and crystal growth in phase-change materials. An understanding of the process involved has direct influence on the heat transfer rate as well as the removal of solidified material from the heat transfer surface. Ideally, the best nucleating agent for salt mixture(s) considered should have similar crystal structure and chemically inert and have high melting point. Understanding the interrelationship between the critical size of the cluster (nucleating agent) and the energy of activation for crystal formation is helpful (1, 2).

Therefore, it is desirable to identify a small number of promising salts that can be studied as suitable and compatible nucleating agents to the eutectic mixtures. These materials should be potentially inert at the temperatures of interest. A few are being recommended as potential materials for early experimentation in the laboratory. Some of these are:

Calcium nitrate Ca (NO3) 2 which has high melting point of 561 C, has cubic crystalline structure, but hygroscopic. Small amount of anhydrous reagent grade salt can be obtained. Another compound is Tungsten oxide (WO3) with high melting point of 14730C and has orthorhombic structure. Low cost Potassium carbonate K2 CO3 with the melting point of 8910C with monoclinic structure is a candidate material. The disadvantage of these materials is that they are not inert and they can interact with the one or more of the components of the eutectic.

Therefore, two inert compounds are suggested: One of them is Titanium Oxide (TiO2).

It has very high melting point (1840°C) and has low thermal expansion coefficient and has been used in certain glass ceramics as a nucleating agent.

Another potential nucleating agent is Zirconia (ZrO2)- a refractory material that has a very high melting point of 2700°C and low thermal expansion coefficient.

Corrosion Rates

Table 4 lists some of the corrosion rates with salts and containment.

Table 4. Corrosion Data for selected components of chemicals in salt mixtures for some container materials

Chemical in the eutectic mixture	***Container Materials***		
	Cast Iron	***Mild Steel***	***Stainless steels***
NaOH	***> 50 Mil/year****	***> 50 Mil/year***	***< 2 to <20 Mil/year***
NaCl			***20 to 50 Mil/year***
$NaNO_3$ SS302) ***		***< 2 Mil/year ****	***> 50 Mil/year (SS 347,***
Na_2SO_4			***> 50 Mil/year***
Na_2CO_3		***> 50 Mil/year*****	
KOH			***> 50 Mil/year***
KNO_3			***< 2 Mil/year***

*** stress, @300C **decarburize**

****** @ 450C with SS 347 has 0.08 % carbon, 18% Cr, 11% Ni and 0.8% Nb. Widely used SS 304 & SS 316 have 0.08% carbon, 19%Cr for 304 and 17%Cr for 316, and 12% Ni for 304 and 11% Ni for 316 and 2.5% Mo for 316.***

Majority of eutectic mixtures with useful melting points in the range of 275 to 350 C, and relatively high heat of fusion, contain anions such as nitrates, hydroxides, sulfates and carbonates with cations of mostly sodium and in some cases potassium partly due to availability and cost. These salts, even in moderately pure state and particularly of commercial grade, contain small amounts of impurities such as chlorides (~ 0.001 to .005%), sulfates (≤ .003%), carbonates (≤ 1%) and Fe (≤ 0.001%) that aggravate corrosion to common container materials. Potentially attractive storage container materials are mild-steels, carbon-steels and cast-irons. Mild-steels contain 0.15 to 0.3% Carbon. Carbon-steels contain up to ~ 2 % carbon and may also contain other elements, such as Silicon (maximum0.6%), Copper (up to 0.6%) and Manganese (up to 1.65%). Cast-irons are Fe-C alloys containing 2 to 4% Carbon. (1). Stainless steels such as 304 and other types contain carbon, chromium and nickel and other metals. For example, Stainless steel 304 has 0.08% carbon, 19% Cr and 10% Ni, stainless steel 304L has 0.03% Carbon, 19%Cr and 10%Ni and Stainless steel 316 has 0.08% Carbon, 17%Cr, 12%Ni and 2.5% Mo. Stainless steel 347 has 0.08%Carbon, 18% Cr, 11%Ni and 0.8%Nb (1

Physical stability and the composition of the container material in contact with the molten salt mixtures are affected by the corrosive properties of molten salt component of the eutectics and some specific impurities present in them by two types of corrosion processes (2). These are chemical corrosion and electrochemical corrosion. The corrosion data for selected container materials in presence of some common molten salt components are listed in Table 4 (3).

Table 6 shows that pressure has little effect on the properties of molten NaNO3 and NaOH. Details of these calculations are shown in Appendix E.

Selected Properties of NaNO3 mixtures

Properties of NaNO3, NaO3					
Property	**Units**	**NaNO3**	**NaOH**	**Eutectic**	**Dilute Eutectic**
Molecular Weight		85	40	71.5	83
Melting Point	Deg C	310	318		
Liq Density	kg/m3	1910	1785	1929	1930
Solid Density	kg/m3				
Heat of Fusion	kCal/mole	3.52	1.52	2.92	3.475
Viscosity	cP	2.89	5.15	3.33	2.9
Heat Capacity	kJ/kg-K	1.84	2.0724		
Thermal Conductivity	W/m-K	0.57	0.8302		
Prandtl Number		9.3	12.9		

Properties of NaNO3 as function of pressure			
Property	**Units**	**P= 1 atm**	**P= 100 atm**
Density	kg/m3	1910	1913
Viscosity	cP	3.062	3.068
Thermal Conductivity	W/m-K	0.57	0.5702
Heat Capacity	kJ/kg-K	1.84	1.832
Isothermal Compressibility	cm2/dyne	17.8 e-12	
velocity of sound	m/s	1704	

Appendix 2 .
Selection of 'Salt-Phobic' Coatings

This section discusses the methods used to select 'anti-stick' coating materials to be used on heat exchangers for storing thermal energy as latent heat of fusion in mixtures of inorganic salts. To enhance heat transfer from freezing salt mixtures heat exchanger tubes are coated so that the force of molten salt at near freezing point pumped from a tank and flowing past the tubes can remove the solid material. The resulting solid slurry is returned to the tank. The heat transfer coefficient is expected to be much higher than passive solidification on tubes.

Statement of the Heat Transfer Problem and Approach to Solution

A major drawback of using phase change molten salt materials is their poor thermal conductivity and the fact that clumping occurs during freezing that sticks to the walls of the storage tank and heat exchanger surfaces. Using our storage media of dilute eutectic would alleviate this problem. As discussed in report on Salt Selection, when a dilute eutectic mixture, such as with a large fraction of NaNO3 in a NaNO3-NaOH mixture, freezes, there is always liquid around the freezing NaNO3. The freezing material is 'mushy' and even though highly viscous, can be pumped to an external heat exchanger. (Note: This is similar to what happens in an ice-cream plant. In these plants, additives such as polysaccharides are added to the ice cream so that it can be easily pumped.)

In addition to taking advantage of the liquid in equilibrium in freezing solid, we are investigating coating materials that can apply to heat exchanger tubes. The coating materials are referred to as 'anti-stick' because the freezing material can be easily removed from it. This is similar to 'Teflon' used in common kitchenware. The coating material should be 'non-stick' to freezing material and have high thermal conductivity. In this report we present results with coating materials such as graphite, metallic nitrides and carbides, and high temperature polymers (such as imides, poly benzo-oxy imidazole). These coatings are deposited on heat exchanger tubes.

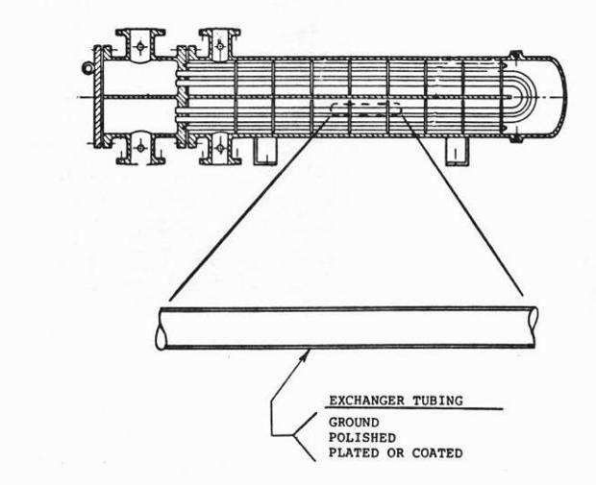

Figure 1. Low adhesion surfaces and shell and tube heat exchangers offer

There are many types of heat exchangers used in the industry for transferring heat during phase change from liquid to solid. Some of the active (not passive) heat exchange designs include shell and coated tubes; others use mechanical scrapers, ultrasonic vibrations or flexing to free the tubes of freezing salts. Three methods show promise:

- use of coated heat exchanger tubes (researched in this project)
- encapsulation of salt in suitable shell material
- direct contact of salt with heat transfer medium such as bubbling water through molten salt.

Our preliminary analysis, based on past research indicates that the shell and tube type of heat exchangers, with the salt on the shell side and the two-phase steam water inside the tube can potentially be successful

when discharging heat from the PCM melt. Furthermore, since this is a commonly used design in the industry it is also the most economical to use.

In addition to the two methods – dilute eutectic mixture and 'anti-stick' coating - , we will investigate a third way to further improve the flow properties and improve the conductivity. We are investigating using additives such as graphite, Nano-carbonaceous materials, and ionic liquids. . We propose these materials because of their high thermal stability, and chemical stability, good heat transfer properties and good non-wetting characteristics with molten salts. We will present the results of this later in another report.

Candidate Coatings

Our approach to selecting and testing coatings consisted of the following steps:

- Use scientific expertise to select a subset of coating candidates
- Use qualitative *dip-test* method to screen and select at least three candidate coatings
- Examine the interface between the solid and substrate using Scanning Electron Microscopy and Optical Microscopy to characterize the morphology of freezing crystals
- Procure tubes coated with the selected coatings and test them on a 'flow rig' specifically designed to freeze salt on the tubes and remove it by using hydrodynamic forces from a flowing salt.

The results from these steps are described below. The tests provide a comparative and qualitative evaluation of selected coatings. A few coatings have been tested. We are discussing with coating vendors for providing samples for a few other coatings. We will continue these tests in Phase II in parallel with the heat exchanger tests planned.

Selection Criteria of Coatings

The strategy for choosing a coating was relatively straight forward. We surveyed the coatings available, and chose those that could handle 4000C or greater. Once we had a collection of such coatings, we further selected from this group coatings which had desirable surface properties. These properties were low roughness, and a hydrophobic nature. A hydrophobic surface is considered desirable because it has a low surface energy. This means that intermolecular attraction between the surface and a crystallite will be limited. As a result "stickiness" of the crystallite should be should be minimized.

A smooth surface is also highly advantageous for two reasons. First of all, lock and key binding of the crystallite to the surface is minimized, second reduced contact surface area minimizes the effect of the intermolecular forces. In effect, the smooth surface enhances its already hydrophobic nature. Appendix A further describes a scientific basis for selecting coatings.

Table 1 is an initial selection of coatings based on the collective scientific thought process which is discussed in the following paragraphs.

Generally speaking, the best coatings are created by physical vapor deposition (PVD), chemical vapor deposition (CVD), and other surface modifying processes carried out in vacuum systems. These coatings are thin, and smooth. Because they are thin, it is expected that heat transfer through them will not be significantly inhibited. The benefit of a smooth coating has already been addressed.

We did not consider using any coating that is applied by flame spraying or similar process because the coatings tend to be porous. This is in line with our desire to maintain a smooth surface. For this reason we did not use Alumina, Chromium Carbide, and Tungsten Carbide.

Boron Nitride was not tested in our first set of experiments. Boron Nitride is generally used in applications were it s not firmly bonded to the surface. For this reason, the common coatings do not firmly adhere to the substrate. An example is its use as a mold release agent. Additionally, Boron Nitride in its most common (hexagonal) form is quite soft. These properties make it less than ideal despite the fact that it is an extremely hydrophobic material. A less common form of Boron Nitride is the cubic variety. In this form, its crystal structure is diamond like, and it is very hard. This form can be applied so that it is very thin. The cubic form is probably suitable for our application and will be a candidate for future experiments once we find a vendor who will apply this coating.

Titanium Carbide is known to have non stick properties in molten salt baths. It surface is extremely smooth and can be made quite thin. It is an excellent candidate.

Titanium Nitride and Chromium Nitride can both be applied in a very thin smooth layer. Both are also known to be hydrophobic. The vendor also supplies a more hydrophobic silicate based coating that can be applied over either nitride and is also extremely thin. This overcoat is said to bond more effectively to the nitride surface than the steel substrate alone. It is subject to a lower maximum temperature limit.

Porcelain is very smooth and would be expected to be low cost because it is a commercial product with a variety of applications. It is not as thin as coats applied using PVD or CVD. It is also not quite as hydrophobic because it contains a substantial amount of glass.

Diamond-like coatings are thin, hydrophobic, and very hard. They are potentially ideal candidates. Cost was a concern, but one type is actually used to coat razor blades. We plan to look into whether the type of diamond like coating we would need is equally inexpensive for future experiments.

Two proprietary coatings of unknown composition may also be very suitable. These are Cerablak and FGI-400HR. The latter has been used on heat exchangers. Coated samples may be available pending special arrangements.

Table 1 CANDIDATE COATINGS

*Indicates the material was tested in this reporting period

COATING	SOURCE	COMMENTS	MAX TEMP	HYDROPHOBIC	SURFACE ROUGHNESS
*Mild Steel		CONTROL	N/A	No	Fine Sanding
*Porcelain SH502	Ferro			Somewhat	Very Smooth
*Titanium Carbide on graphite Titanium Carbide on Steel	Solar Atmospheres Ultramet and others	Temperature limited by graphite substrate and presence of air CVD coating on steel also possible	>400	Yes	Very Smooth
*Titanium Nitride	BryCoat	PVD coating	600^{0}C in air	Yes	Smooth
*Chromium Nitride	BryCoat	"	1050^{0}C	Yes	Smooth
*Brycoat HTS over *Titanium Nitride	Brycoat	Proprietary silicate based overcoat	400^{0}C	Yes	Smooth
*Brycoat HTS over *Chromium Nitride	Brycoat	"	400^{0}C	Yes	Smooth
Cubic Boron Nitride (Diamond Like)	Ceratizit	PVD	2973^{0}C	Yes	Smooth
Alumina	Brycoat (and others)	Flame sprayed	1700^{0}C	No	Porous when flame sprayed
Chromium Carbide	Pacific Particulate Materials among others	There are several chromium carbides with different melting points	1250^{0}C - 1895^{0}C	Probably	Porous when flame sprayed
Tungsten Carbide	CCI (Canada)	Flame sprayed	2870^{0}C	Probably	Porous when flame sprayed
FGI-400HR Ceramic Thermal Transfer Coating	FGI International	Used on heat exchangers	980^{0}C	No data yet	No Data yet
Diamond like Carbon	Morgan Advanced Ceramics	Ion Beam and RF plasma deposition	1200^{0}C	Yes	Smooth
Cerablak	Applied Thin Films Inc.	No data	1400^{0}C	Yes	Smooth

Dip Testing Method for Selecting the Coatings

The test we devised is intended as a preliminary, rapid screening test. The idea is to determine if crystallites formed in the molten salt were likely to stick to the surface of the heat exchanger. The test as devised does not duplicate all the conditions within the molten flow loop. As a result, the screening tests will not necessarily duplicate what will be seen in the field. Despite this limitation, it should be able to allow the qualitative comparison of one coating to the other. In certain respects, the test as designed represents a more severe test of crystallite adhesion/accumulation than might be expected in actual operation.

For the purpose of the test, a furnace is equipped (Fig. 3 and Fig. 4) with a stainless steel pot to contain the salt. In the pot are a stirrer and thermocouple. The stirrer is driven by an air motor which can be set to spin very slowly. The stirrer passes through the wall of the furnace through a stainless steel sleeve. This was necessary to eliminate the grinding off of firebrick insulation by the rotating shaft. The thermocouple is connected to a digital temperature controller that replaces the older malfunctioning analog temperature controller originally built into the furnace. The new controller is more reliable, accurate, and easy to read.

The furnace is also provided with an Argon gas port. The purpose is to prevent oxidation of samples where this is an issue and to insure that the molten salt is not affected by CO_2. CO_2 is an issue when the salt contains NaOH. The NaOH can react with the CO_2 to form carbonates, thus changing the melt composition.

In order to evaluate the performance of different coatings we used a "dip" test. This test was conducted in the following manner.

First, the salt is prepared. We used a proprietary binary salt mixture with a dilute eutectic melting about 300^0C. The salt is placed in a 316 stainless steel container. The thermocouple and stirrer are temporarily suspended above the salt. The Argon is turned on and the furnace is closed. The temperature controller is set to 500^0C. This high temperature is needed because the two components are not mixed initially and the salt melting point is higher. Once the melting has begun, the stirrer and thermocouple is lowered into the salt bath. When the bath is completely liquefied, the stirrer is turned on, and the temperature is lowered to 400^0C. Now that the binary mixture is completely mixed, it remains liquid at a lower temperature. The sample is lowered into the bath suspended on a stainless steel wire. After the sample is immersed, the temperature controller is set to 250^0C. The door of the furnace is now cracked open to allow for cooling. When the solution cools to the point that it is full of crystallites, but not fully solidified, the sample is withdrawn. Generally, this occurs at about 300^0C. At this time the sample is briefly inspected to determine if some crystallites are present. As the sample cools off, more crystals form. The former type of crystal sticks out of the surface. The ones formed as a result of cooling in air are relatively flat. They are formed from the adherent film of salt that is liquid at the time of sample withdrawal.

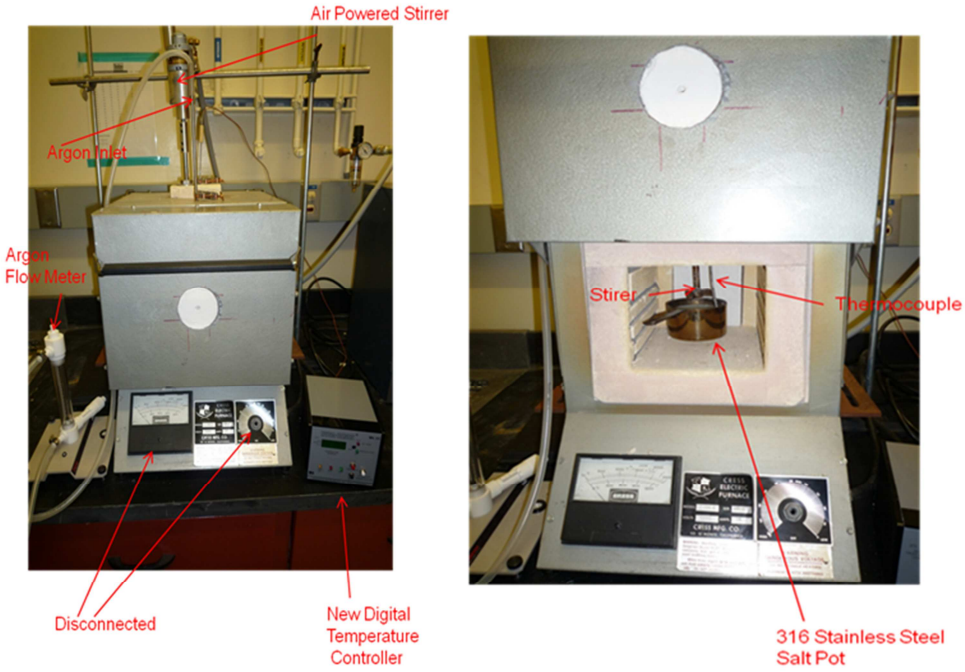

Figures 3 & 4. Dip Test Furnace

Results of Dip Tests

Samples were not characterized quantitatively as to smoothness, but all the samples were very smooth with the possible exception of the mild steel control. This sample was sanded and had obvious markings. The first 3 samples in Table 2 below were of various sizes, the ones after were standardized to 2 cm x 2 cm. The mild steel coupon was prepared under Argon gas blanket to prevent oxidation. The porcelain and Titanium Carbide samples were prepared in air before it was recognized that the bath could degrade as the result of a reaction between NaOH and CO_2. The remaining samples were prepared from a new bath and under an Argon blanket.

The samples were checked for crystallite adhesion when cool. We were looking for very large differences in adhesion so we employed a very simple test. We scraped the surface of the sample with a finger nail. If a crystal could not be removed this way, we considered the surface unsuitable. Those samples were crystals could be removed in this manner were classified as mild or moderate adhesion. Photographs of most of the samples are shown below with explanations. For TiN and CrN (without Brycoat HTS), the adhesion declined after several days.

Table 2. Qualitative Evaluation of Coatings

Material	Adhesion
Mild Steel	Strong
Ferro SH502 Porcelain on Steel	Strong
Solar Atmospheres TiC on Graphite	Mild ***
Brycoat TiN on Mild Steel	Moderate ***
Brycoat CrN on Mild Steel	Mild/Moderate Presumed Surface Damage
Brycoat HTS over Brycoat TiN on mild steel	Strong
Brycoat HTS over Brycoat CrN on mild steel	Strong

***Recommended for Further Testing

Discussion of Results

The sample below shown in Fig. 5 is mild steel with no coating. The bottom accumulation is caused by surface tension effects. Liquid accumulates there during cooling and then freezes. The top accumulation is the liquid line. This sample was tall enough to protrude beyond the liquid level. Crystal accumulation between those lines formed in the pot. The very flat crystals are generated from the liquid film that remained on the sample when it was removed from the pot. All of these crystals were strongly attached.

Figure 5. Photograph of salt on uncoated mild steel surface

The porcelain sample below (Figures 6 & 7) was much smaller. It did not stick out of the melt. The crystals stuck on to the porcelain very strongly despite the shiny surface of the material. This material is

only somewhat hydrophobic, and it might be getting etched by the NaOH. It does not appear to be a candidate choice.

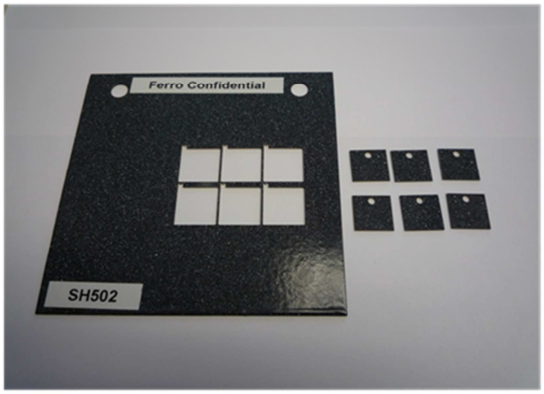

Coupon Before Immersion in Molten Salt

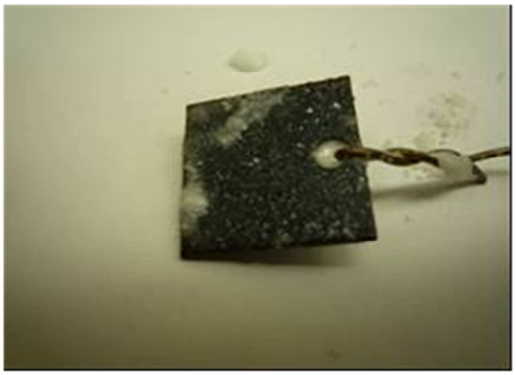

Coupon After Immersion

Figures 6 & 7. Ferro SH 502 Porcelain

The TiC shown in Figures 8 & 9 is grown in situ on a graphite substrate. It is a mirror finish. This is shown by the reflection of a paper clip on to the surface.

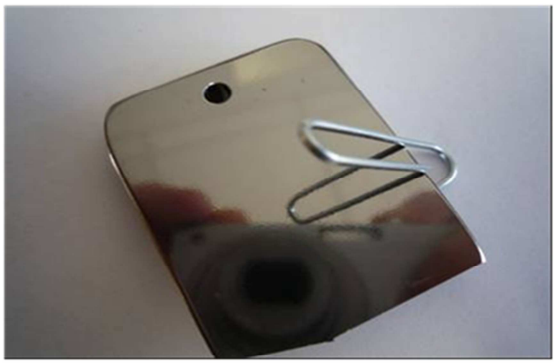

Coupon Before Immersion

Cross Section Showing Graphite Substrate

Figures.

Figures 8 & 9. Photographs of TiC coupon before immersion

The crystal formed on this surface were easy to remove. Figure 10 shows a patch that peeled off by using fingernail pressure. The very smooth deposit suggests that most crystals did not attach while the sample was immersed in the salt. The crystals showing are the type associated with the liquid film that remains o the sample after it is removed from the bath.

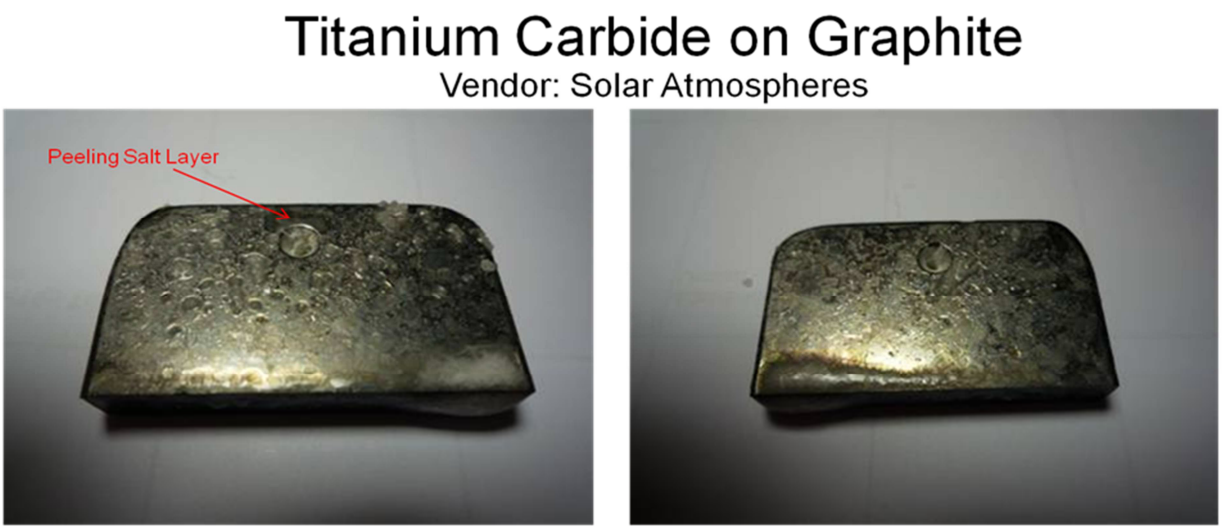

Figures. 10 &11. TiC on Graphite samples

The TiN samples shown in Figure 12 and Figure 13 below are before and after photographs respectively. The surface of the TiN was very smooth, although it was not mirror like. The salt did not stick very strongly to this surface. The photo in Figure 13 (right) shows a small area where the salt peeled off as a result of applying fingernail pressure. After a few days storage in air, the salt came off more easily. The surface did not appear harmed in any way from salt exposure.

Figures 12 & 13. Photographs of TiN on Steel

The CrN samples both before and after are shown in Fig. 14 and 15. The adhesion to this surface was a bit less than the TiN but it was obvious that the sample was damaged in some way because of the discoloration after treatment.

Figure 14 & 15. Photographs of Chromium Nitride coating

Both of the same types of samples were also coated with Brycoat HTS. This silicate based coating is extremely hydrophobic. The coating is not good above 400^0C normally, but we chose to try it anyway because the temperature limit was for exposure to air and because our operating temperature would normally be lower. Our system was more or less free of air so it seemed worth a try. The coating degraded and changed color in patches. Our salt stuck to it very strongly. This proved not to be a good candidate for further screening.

We will continue to test and screen more coating samples in Phase II. The next section describes and discusses the results from the scanning electron microscopy of some of these *dip-coated* samples.

Interface Properties during Freezing of Salt on Coated Tubes

Scanning Electron Microscopy images and discussion for different coatings

Samples from dip tests in salt with the dilute eutectic composition of NaNO3 and NaOH, described earlier, were observed in a Scanning Electron Microscope (SEM) to study the interface properties between the salt and metal surface.

All samples are properly prepared and polished in order to minimize the damage to the surface salt layer, and are coated by Au-Pd to become conductive for SEM microscopy.

The aim of this study is first to measure the thickness of the surface salt layer accurately to compare the different coatings and next to study the surface morphology. The thickness can give us a value for

measuring the stickiness of a certain salt composition to a certain surface and the morphology will provide the types of crystals adhering to the surface.

Figures 16 to 20 show the images of scanning electron microscopy for five different samples: mild steel without coating, mild steel with Porcelain coating, mild steel with CrN coating, mild steel with TiN coating, and graphite with TiC coating in two magnifications.

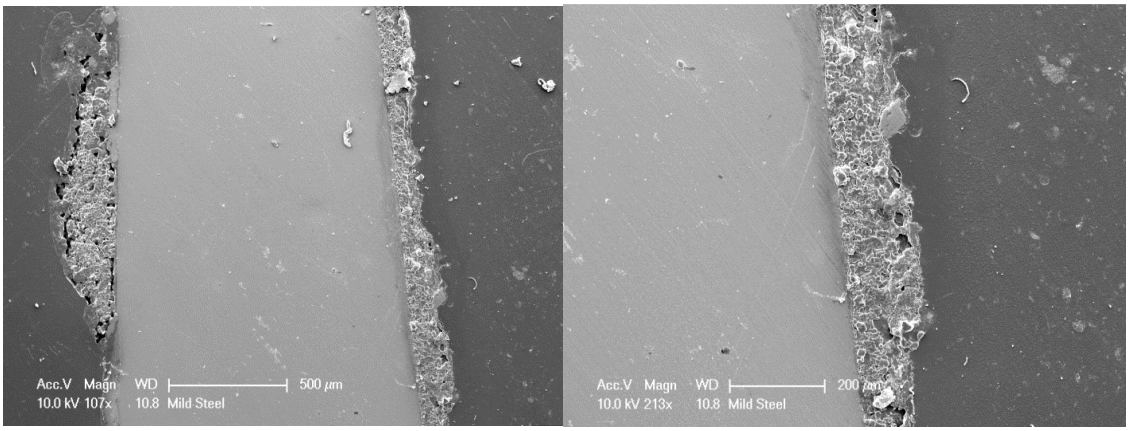

Fig 16 SEM image of the mild steel dipped into the $NaNo_3$(98%)-NaOH(2%) molten salt. The solidified salt layer can be seen in two different magnifications.

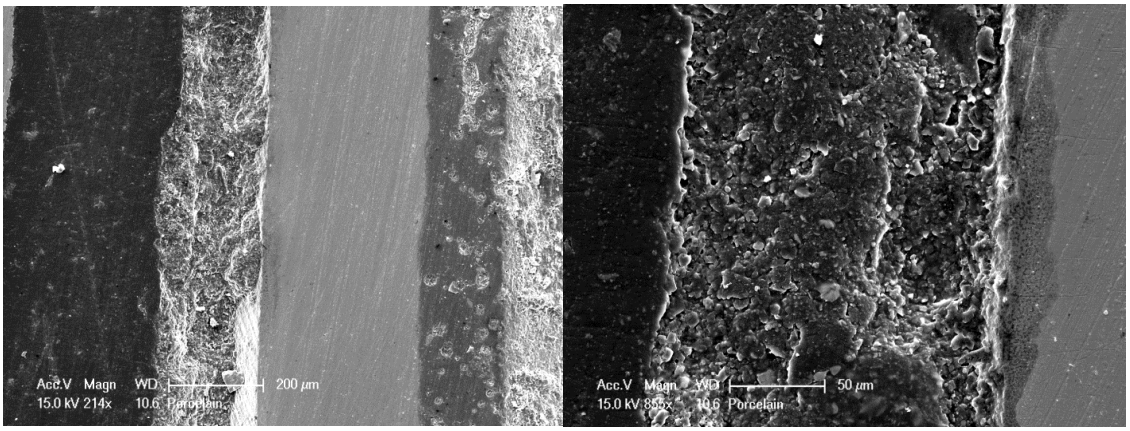

Fig 17 SEM image of the mild steel coated by Porcelain and dipped into the $NaNo_3$(98%)-NaOH(2%) molten salt. The solidified salt layer can be seen in two different magnifications.

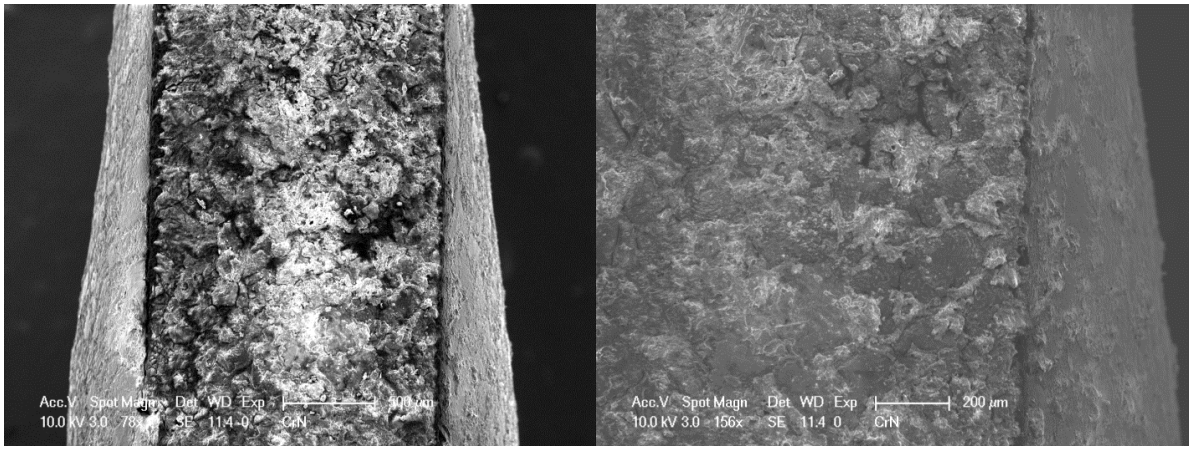

Fig 18 SEM image of the mild steel coated by CrN and dipped into the $NaNo_3$(98%)-NaOH(2%) molten salt. The solidified salt layer can be seen in two different magnifications.

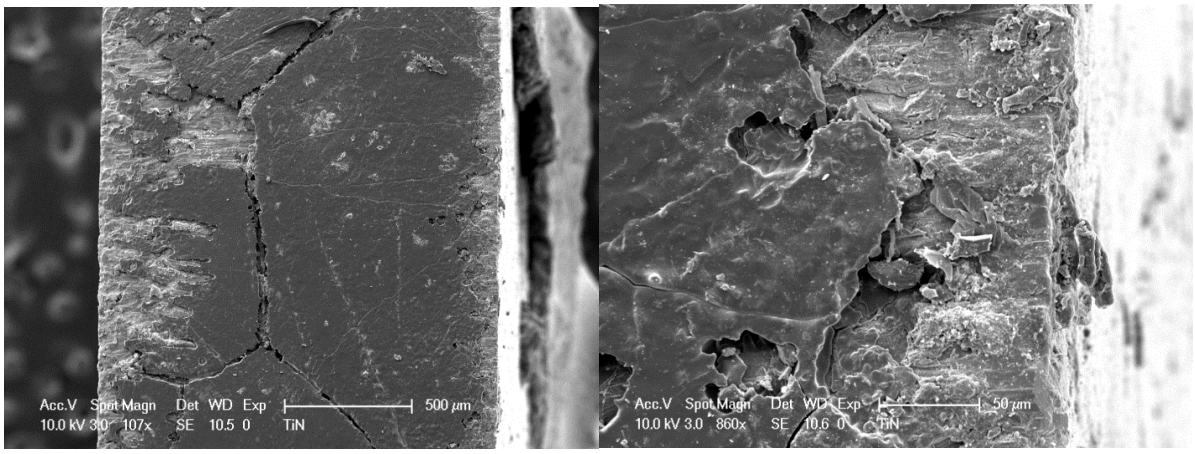

Fig 19 SEM image of the mild steel coated by TiN and dipped into the $NaNo_3$(98%)-NaOH(2%) molten salt. The solidified salt layer can be seen in two different magnifications.

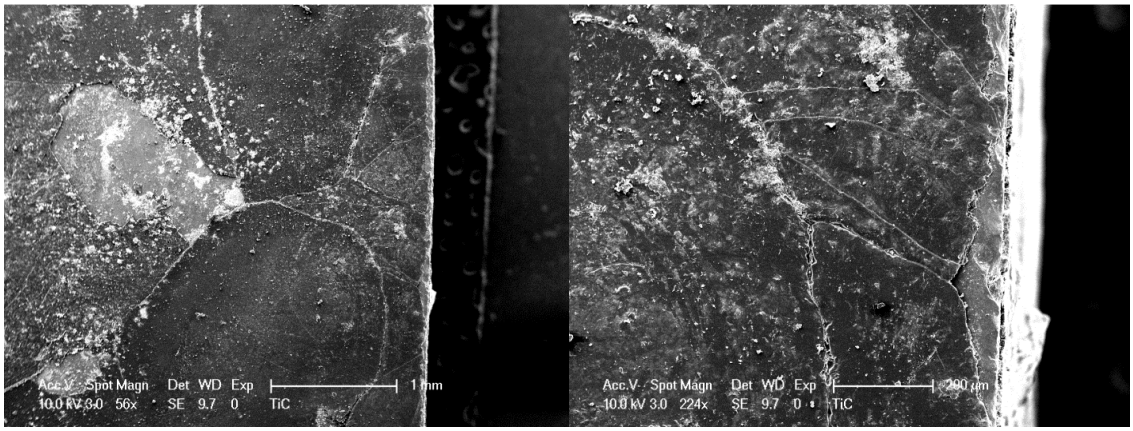

Fig 20 SEM image of the Graphite coated by TiC and dipped into the $NaNo_3$(98%)-NaOH(2%) molten salt. The solidified salt layer can be seen in two different magnifications.

Table 1 Comparing different samples salt layers

Coatings	Mild St/non	Mild St/Porcelain	Mild St/CrN	Mild St/TiN	Graphite/TiC
Sample thickness	1.25 mm	0.7 mm	1.5 mm	1.5 mm	10 mm
Salt layer thickness	187 µm	200 µm	333 µm	125 µm	57 µm

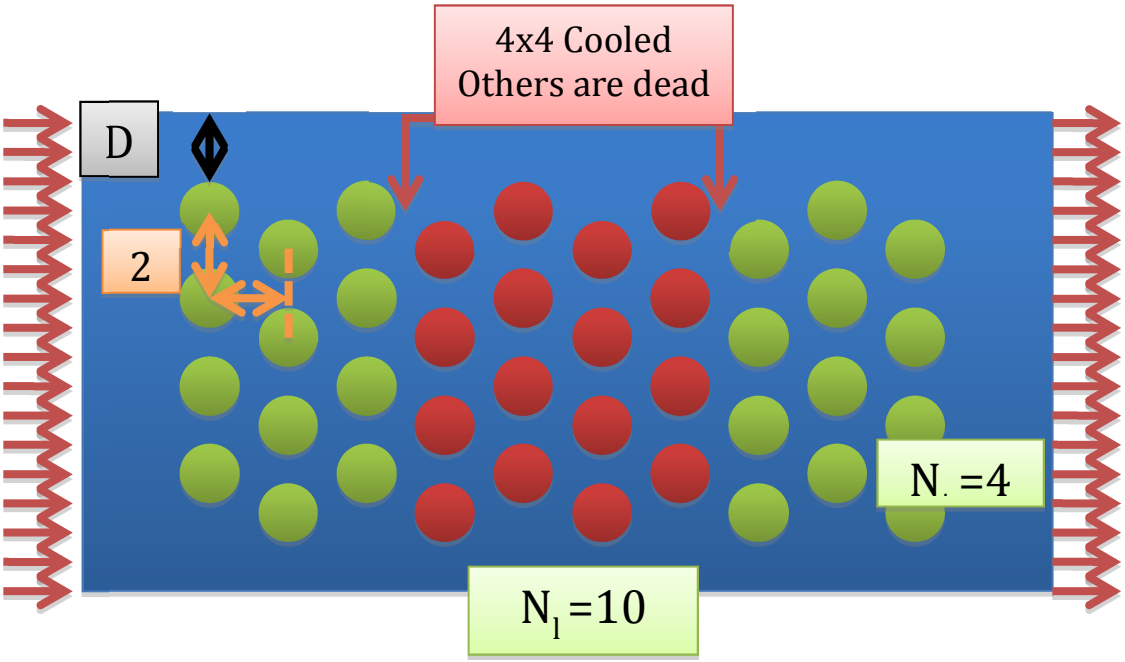

Table 1 above, shows the measured thickness of salt layer on each of the surfaces. According to the results on table 1, TiC coating has the lowest salt layer thickness while the mild steel surface has the highest. The lower thickness of salt may indicate either the salt removal when material was stirred or could be due to the amount salt held by surface tension forces when the sample was retrieved or could be due to cooling and exposure time. The TiC coating may be a promising candidate based on the visual observation of the surface and surface finish and the lower thickness of the coating which may indicate salt removed during stirring.

In addition to salt layer thickness, solidification morphology on different samples was studied. Fig 21 shows the main observed ones.

The bottom right coating with dendrite salt crystals may be better for removal with fluid flow force. However, if this grows uncontrolled and we are unable to break the structure in the early stages of formation, then it can form a strong mesh structure. The space between the dendrite may have been the equilibrium liquid which froze when the sample were cooled down. We will continue to study these morphologies using controlled and re-producible experiments.

Candidate Coatings for Tests with 'Flow-Rig' Heat Exchanger

Based on tests and our interpretation of the results from these tests, we selected the following three coatings for further evaluation with the 'flow-rig' experiment.

- Titanium Carbide Coating on Stainless Steel
- Titanium Nitride on Stainless Steel
- Chromium Nitride on Stainless Steel

Stainless is recommended for the flow-rig experiment to prevent or reduce corrosion. The entire flow-rig is constructed using stainless steel. We will continue to investigate by dip tests the following coatings:

- Cubic Boron Nitride Coatings on graphite or stainless steel
- Cerablack TM coating (proprietary to vendor)
- SGI 400 HR another vendor proprietary hydrophobic coating used on heat exchangers

If any of these show promise we will evaluate them using the flow-rig. The flow-rig is designed to replace tubes easily to conduct qualitative coating tests and measure temperature rise in the fluid inside the coated tube. The temperature rise will provide a relative quantitative measure on *stickability* of salt.

For the final selected coating, we will determine the best thickness of coating, method for depositing the coating and the substrate finish required to meet the performance objective. This will be done prior to building the Phase III engineering model design.

A Note on Candidate Coatings for the Dilute Eutectic Mixture:

It was deemed necessary to investigate further and with more detailed experimentation than the initial results provided by JPL with the dip tests. The effort included electropolishing the samples, setting up the vacuum chamber, making the coatings (evaporation and/or sputtering), testing them with DSC, and analyzing the surfaces and samples by optical microscopy, SEM, and profilometry.

The coating experiments were conducted with pure NaNO3. Even though these coatings performed well with sodium nitrate, adding a small amount of sodium hydroxide caused pitting and the coatings did not survive the attack.

Additional tests were carried out using differential scanning calorimeter to screen coatings for use the dilute eutectic mixture. As discussed in Section 3, chromium coatings were selected as preferred coating.

Seamless stainless steel tubes were first electropolished and chromium is deposited on the tubes. The method and amount of chromium made a difference as discussed in Section 3.

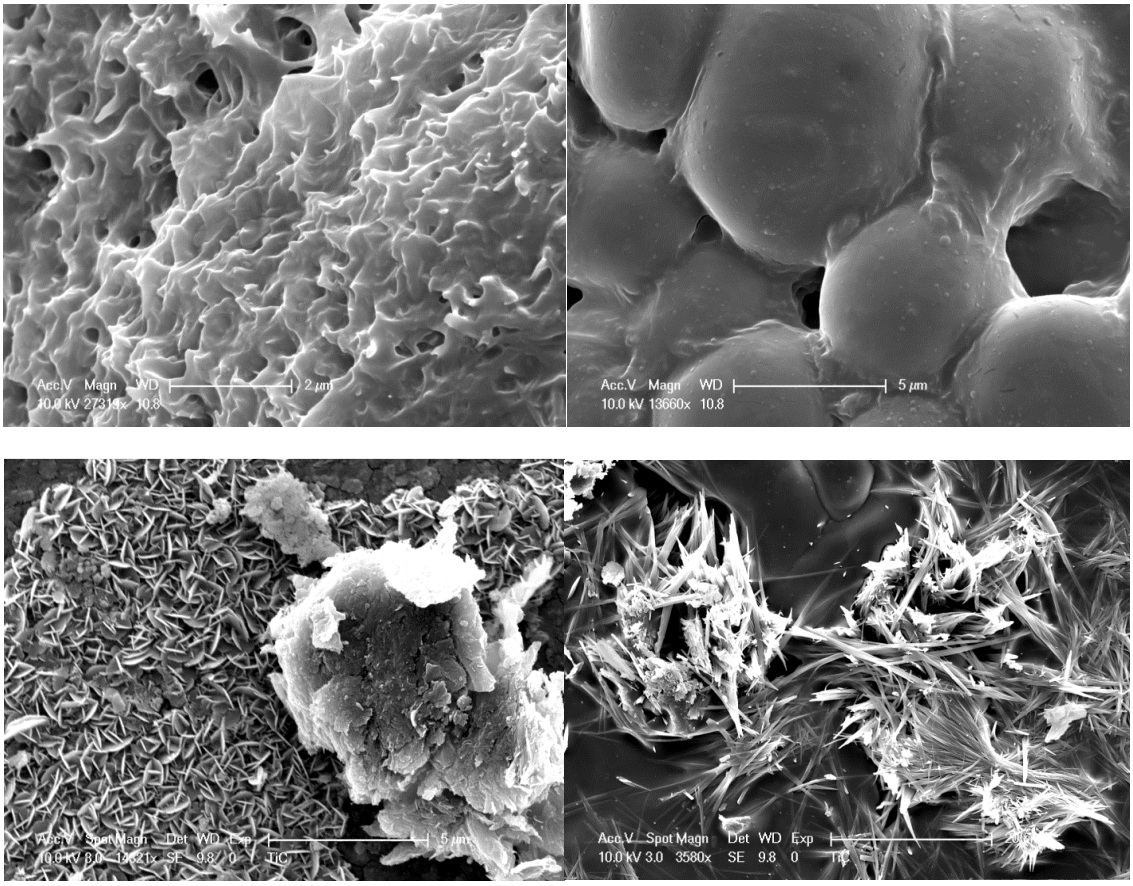

Figure 21. Main salt solidification morphologies observed by SEM

Surface Physical Chemistry – Properties of Coatings Likely to Influence Stickiness of Crystallizing Molten Salt on Heat Exchanger Tubes

Andrew Kindler, JPL

When a crystallizing molten salt is in contact with a heat exchanger tube, there are gradual accumulations of crystals that stick to the outer portion of the tube and impede heat transfer. In order to prevent accumulation of these crystals, both the surface (physical) chemistry and the surface morphology of the tube and crystals must be taken into account. Below the influence of two surface properties on adhesion of crystallites is summarized and related to the choice of material screening test for the heat exchanger.

There are two properties that are likely to influence crystal adhesion: 1) Surface energy of the crystal and heat exchanger surface, and 2) Presence of defects on the heat exchanger surface that are likely to precipitate nucleation there. A simple contact angle test may be insufficient to determine a suitable heat exchanger material.

Surface Energy

The surface energy is the property that determines the surface tension. High surface energy materials like clean metal surfaces have high surface tension. Practically, this means that the interatomic forces of attraction within the metal are relatively high. It also means that the attractive forces relative to anything in contact with it will also be high. Based on this characteristic alone, one might prefer a low energy surface to discourage adhesion. A good example of such a surface is Teflon. Although it is not useful at our operating temperature, it is a low energy surface, and is known for its non stick properties. Such surfaces can be characterized by the contact angle of a liquid on the surface to be tested. A high contact angle (beading up) of a liquid drop on the solid surface is generally indicative of low surface energy of the solid. To be more precise, the surface tension of the solid is low relative to the liquid. If both liquid and solid have the same surface tension, there will be no beading. In our system, we might look for a solid that has low surface tension relative to the molten salt and characterize it by the contact angle of the molten salt on the surface of the solid. This characterization may not be sufficient.

It is not, after all, the molten salt that is sticking to the heat exchanger it is the crystal. The crystal is irregularly shaped, so it is unlikely to have excellent contact with the heat exchanger surface. Even if the crystal has the same surface energy as the liquid (uncertain) its effective surface tension is lower because only a small part of the crystal may have intimate contact with the surface. In other words, the stickiness of the crystals relative to the heat exchanger may be not play as great a role as one imagines. If such is the case, an interesting outcome is possible. You might actually find that a high surface energy surface (as well as a low one) discourages the adhesion of crystals! The reason for this is that the liquid will make more intimate contact with the heat exchanger surface. The intermolecular forces binding the liquid to that surface are greater than that binding the crystal. This means that the crystals will be displaced by the liquid. In this scenario, the greater the attractive intermolecular forces emanating from the heat exchanger made of high surface energy material, the more likely it is to physically bond with the liquid rather at the expense of the solid. From this discussion, you could conclude that both very low energy surfaces and very high energy surfaces could prevent adhesion of crystals. In such a case, you would look for both beading of the molten salt on the surface, or complete wetting. In view of this

conclusion, a contact angle test might not be sufficiently definitive to select a material. Additionally, there is another issue discussed below.

Morphology

Surfaces can be smooth, rough, or even porous. The morphology of the surface is very important. The reason is, rough or porous surfaces offer nucleation sites for the growth of crystals. If a crystal is nucleated on the surface, it is likely to stick. Nucleation sites can be regarded a "sticky" because they allow the forming crystal to drop to a lower energy state than in other locations. If this is the dominant mode of accretion, preparing the surface so that it is extremely smooth is advantageous. Additionally, a low energy surface would be the best choice because the nucleation sites remaining would be far less effective.

Observations

Although both low and high energy surfaces may prevent crystals in the molten salt from depositing on the heat exchanger, preventing nucleation is best accomplished with a very smooth low energy surface. Because it is not known, whether nucleation at the surface is a dominant mode, it is not entirely clear whether we want a low or high energy surface. A contact angle measurement to screen for low energy surfaces may overlook useful high energy surfaces that do not accumulate crystals. A more reliable test for heat exchanger coatings is to immerse a coupon in the crystallizing molten salt and actually test how effective a coating it is. Another possible approach is to correlate the immersion test with the contact angle test for both high and low surface energy surfaces to see which one works best. After this determination, contact angle can be used as a more rapid screening method.

Electrochemical Polishing Parameters for Stainless Steel Tubes

Dr. H. Venkatasetty

316 Stainless tube materials are attractive for heat transfer in high temperature thermal energy storage systems. However, most metals and alloys (including stainless steels), have many surface impurities and/or defects such as metal oxides, foreign particles and stress points which result in poor thermal conductivity and are to prone to corrosion. Electrochemical polishing of surfaces is a well established technique used in industry to produce bright and shiny surfaces suitable for commercial applications. In the case of stainless steel, electrochemical polishing has the potential to provide passive surface with improved corrosion resistance and enhanced thermal conductivity.

With a view to develop suitable electrolyte solutions and experimental parameters for obtaining optimum surface characteristics for 316 stainless steel, we prepared several electrolyte solutions using pure Sulfuric acid and Phosphoric acid and their mixtures with de-ionized water as shown in Table 1.

Table 1. Electrolyte solutions with de-ionized water and Electropolishing parameters

Electrolyte Solution	Composition	Electropolishing time
1.Sulfuric acid	68% by volume	10 & 20 mins
2.Sulfuric acid	40% by volume	3, 5, 10 and 15 mins
3.Phosphoric acid	5% volume	10 and 20 mins
4.Phosphoric acid	50% by volume	10 and 20 mins
5.Phosphoric and Sulfuric acid	60% and 20% vol	25 and 30 mins
6.Phosphoric and Sulfuric acid	40% and 40% vol	8, 10, 20, 25 and 30 mins

316 stainless steel substrates were obtained and their surfaces were cleaned with distilled water and isopropyl alcohol and dried. Digital images of the surfaces were obtained. The cleaned substrate was made the working electrode (anode), the counter electrode (cathode) was a larger size stainless steel substrate and the reference electrode was a Saturated Calomel Electrode (SCE). The electrodes were placed in a suitable container with the electrolyte solution. Using the laboratory Electrochemical Instrumentation, the voltage on the working electrode was slowly increased while monitoring the cell current till the current showed a rapid increase and the voltage was set at a known value and the electrochemical polishing continued for known periods of time. The experiments were conducted at different voltages namely 1.4 V, 1.53 V, 1.6 V and 2.1 V at room temperature. The experiment was stopped at known time interval and the samples were cleaned and dried and the surfaces were examined in the microscope and the digital images were taken. The compositions of the electrolyte solutions and electrochemical polishing parameters are shown in Table 1. Digital images of 316 stainless steel, initial and electrochemically polished for different times in Sulfuric, Phosphoric acid and their mixtures are shown in Figures 22 to 31.

The results of these experiments show considerable improvements of the surface characteristics of substrates after electropolishing in many of the electrolyte solutions particularly from 8 to 30 minutes in sulfuric acid solutions at 40, 50 and 68% by volume. Similarly, Phosphoric acid at 50 % by volume and Phosphoric acid and Sulfuric acid and the mixtures 60 % and 20 % by Volume respectively for 10 and 20 minutes shows promising results. However, it was found that the electrolyte solution with 40% volume

Phosphoric acid and 40% volume Sulfuric acid on electropolishing at 2.1 V for 8 minutes shows much better surface characteristics such as shiny and smooth surface (Figures 9,10).

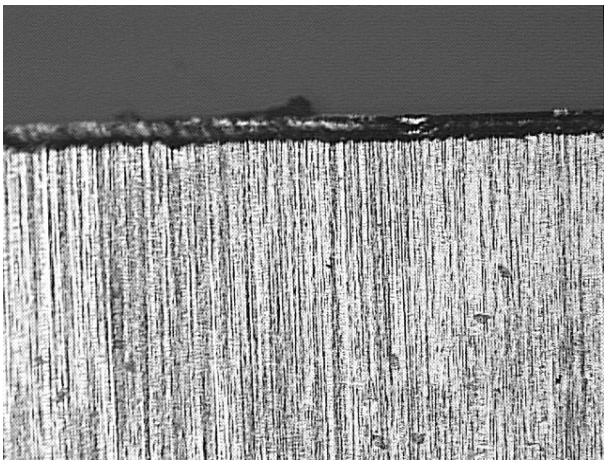

Figure 22. Initial surface characteristics of the Sample . 100X

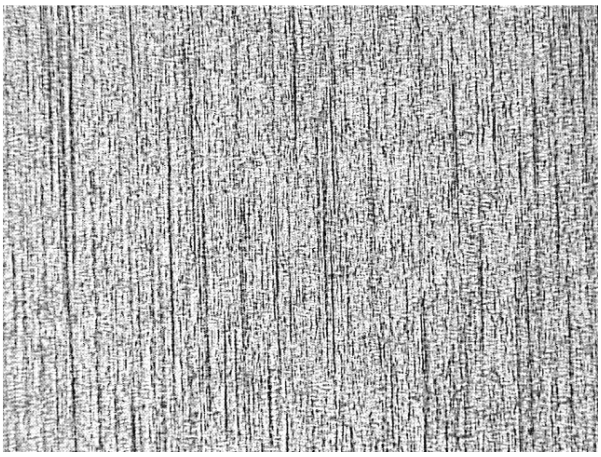

Figure 23. Electropolishing in 40% Sulfuric acid for 5 minutes, center of Sample. 100X

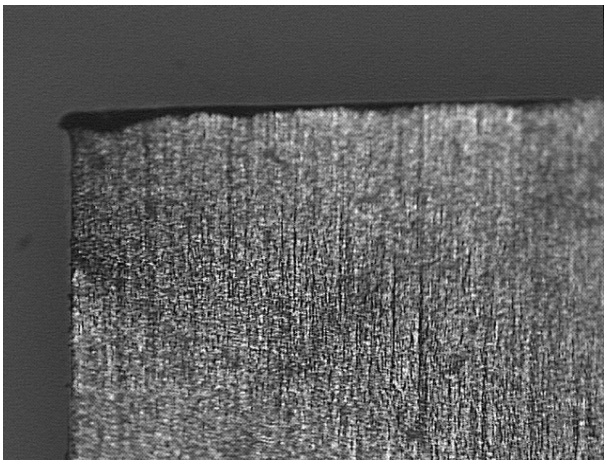

Figure 24. Electropolishing in 40% Sulfuric acid for 10 minutes. 100X

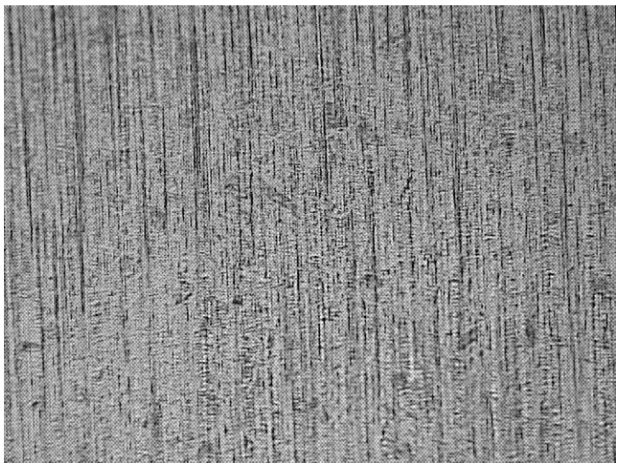

Figure 25. Electropolishing in 68% Sulfuric acid, for 10 minutes. 100X

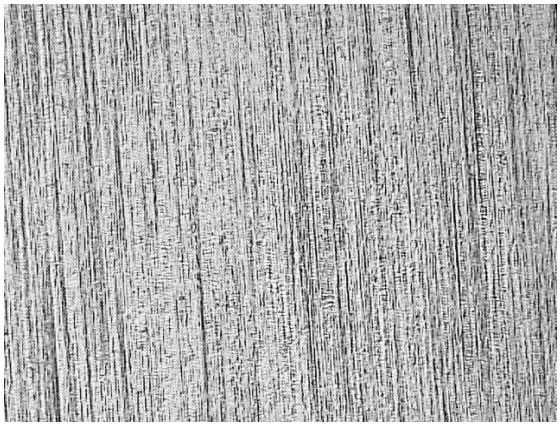

Figure 26. Electropolishing in 5 % Phosphoric acid for 20 minutes. 100X

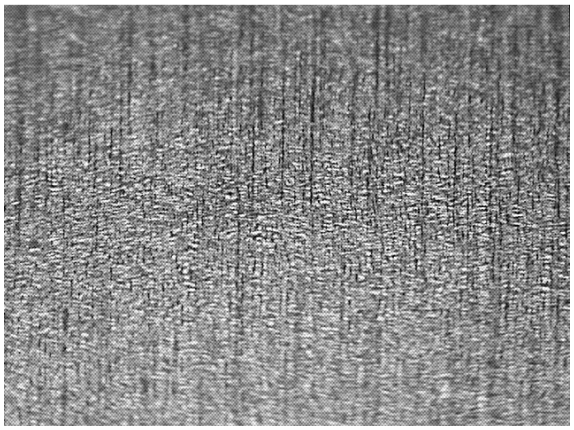

Figure 27 Electropolishing in 50% Phosphoric acid for 20 minutes. 100X

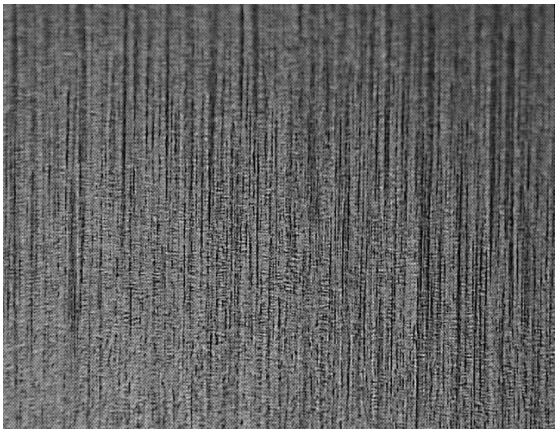

Figure 28. Electropolishing in 60% Phosphoric acid and 20% Sulfuric acid for 15 min. 100X

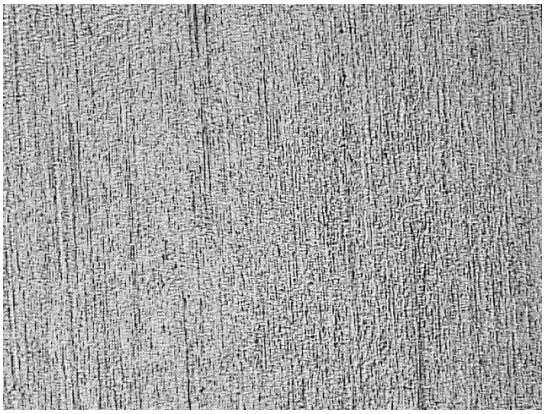

Figure 29. Electropolishing in 60% Sulfuric acid and 20% Phoshoric acid for 30 minutes. 100X

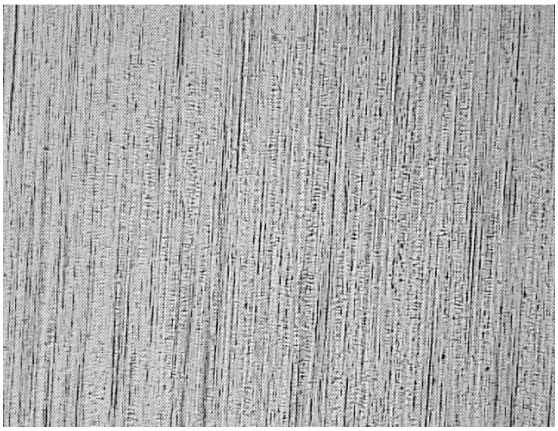

Figure 30. Electropolishing at 2.1 V in Phosphoric/Sulfuric acid 40/40/20 for 8 minutes. 100X

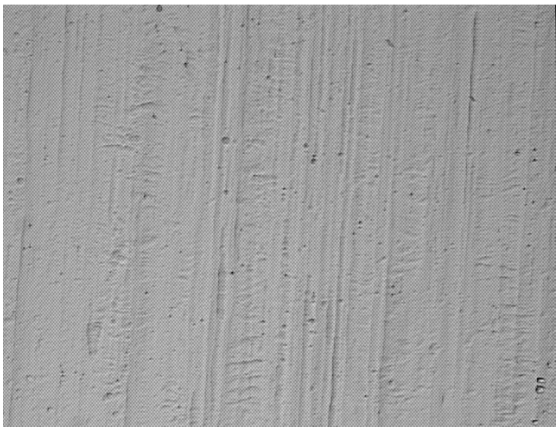

Figure 31. Electropolishing at 2.1 V in Phosphoric/Sulfuric acid 40/40/20 for 8 minutes. 500X

Appendix 3
Design of Laboratory Scale Prototype

By Corey Hardin

This section focuses on the design of the experiment apparatus for studying the heat transfer performance in latent heat storage systems. The report begins with a baseline analysis balancing predicted overall heat transfer coefficient and solidification with heat exchanger area. After this, more detailed analysis is presented to analyze the effects of tube size on Reynolds number, pressure drop, % *solidification, etc. The purpose of this is to establish a baseline of calculations for further detailed design to follow. The analysis assumes cross flow, which should be analogous to a baffled shell and tube heat exchanger.*

Introductory Analysis

To begin our analysis we will present a baseline energy balance calculation. We balance the overall heat transfer rate with the energy it takes to bring the salt down to melting temperature and achieve a solid fraction of 20%. For the purposes of this calculation we assume tubes of 0.375" OD, and a channel cross section of 10 diameters square (i.e., 3.75" x 3.75"). We account for 50% of this area being blocked by tubes giving us a cross sectional area, A_c, of .009 m^2*50%. We also assume an overall ΔT of 15 degrees Celsius between salt and tube walls, and an inlet superheat of 5 degrees Celsius.

$$\dot{Q} = hA_s\Delta T = \dot{m}\left(C_pT_{superheat} + H_f\varphi\right) = \left(\rho A_c V\right)\left(C_pT_{superheat} + H_f\varphi\right)$$

h (W/m^2K)	500
ΔT (C)	15
C_p (kJ/kgK)	1.821
$T_{superheat}$ (C)	5
H_f (kJ/kg)	174
ϕ (% Solid)	20%
ρ (kg/m^3)	2260
A_c (m^2)	.009*50%

From this we are left two independent variables: heat exchanger surface area A_s and salt velocity V. If we assume a velocity of 1 m/s (Re_D=8300), Q works out to 450 kW, which leads us to a heat exchanger area of 60 m^2. This means for an array of 40 cooled tubes we would need over 525 passes to achieve the desired solid fraction. Alternatively, we could achieve the desired 20% solid fraction at only 14 kW if we decreased the salt velocity to 0.03 m/s; however in this case the salt-side Reynolds number would be only 250.

Importance of Reynolds Number

The capability of operating at high Reynolds number is an important functionality for this apparatus for two major reasons:

(i) To ensure that we can produce the hydrodynamic forces that will be necessary to achieve "flaking" of the salt off of the tube. The larger the range of Reynolds numbers we can test, the larger the range of coatings we will be able to test. Even if our coatings fail to flake at industrially viable Reynolds numbers, if we can prove that flaking will occur at higher Reynolds numbers this will be proof that our concept is viable. From a scientific perspective if we could hit a high enough Reynolds number to flake off of a plain or coated steel tube, we could begin to perform a thorough study in which we could possibly come up a with a formula to relate coating surface energy to Reynolds number necessary for flaking. This would make heat exchanger design for the full scale system very simple. On the other end, if we don't give ourselves the capability of high Reynolds numbers we may fail to create the flaking phenomenon at all.

(ii) Scaling to match full-size heat exchangers. Basic on initial familiarity with typical full-scale heat exchangers involving molten salt, we expect that a typical Reynolds number is in the range of 20,000. Also, typical convection design curves for staggered tube banks and shell & tube heat exchangers show a transition in behavior at around $Re_D \approx 1{,}000$, in terms of both pressure drop and heat transfer [ref. *Perry's ChemE Handbook*; Zukauskas in Hartnett & Irvine *Adv. Heat Transf*]. Therefore, to be able to match the approximate operating conditions of a full-scale heat exchanger, it is important for this apparatus to be capable of operating in the ReD range of several 1,000 at the very least, and with a strong preference to reach the range of 20,000+.

Heat Transfer Fluid Selection

We first performed a study to analyze the affects of using various different heat transfer fluids to determine which would be most effective for use in the phase 2 apparatus. The fluids analyzed were air, helium, compressed air, compressed helium, and Therminol 66. Of these, Therminol 66 and compressed helium both showed excellent heat transfer characteristics while having distinct advantages and disadvantages in other areas. Compressed helium was favorable due to its ease of implementation, without any design research necessary to implement. Leaks are also much easier to deal with, and the system overall would be far less complicated than a Therminol system. It does however suffer from a few drawbacks. The first is that it is not a current staple in power generation, although it has been used as a heat transfer fluid elsewhere. The helium compressor necessary was also considerably more expensive than a heat transfer equivalent Therminol pump and we would have to deal with greater pressures. Therminol has a few drawbacks in that it does require a good amount of research to implement properly, there are more safety issues in design, leaks are far less tolerable, and the system must be much more complex in order to operate safely. In the end Therminol won out over helium due to the fact that it gets higher heat transfer at less cost, is widely used in industry, and works at significantly lower pressures.

Scaling Rules

Before more detailed analysis could be performed, standard scaling parameters had to be established to allow for fair comparison between different tube sizes. A preliminary analysis was performed to determine the best tube arrangement to produce. It was observed that higher tube pitches allowed for higher heat transfer rates with much smaller pressure drops and similar flow rates. It was therefore decided to pick a fairly high pitch to diameter ratio of 2 (table values for heat transfer correlations range from 1.25 to 3). In Incropera and Dewitt's *Introduction to Heat and Mass Transfer* it states that heat transfer conditions do not fully develop until the fourth tube in a bank, therefore it was decided to place 3 dead columns of tubes on each side of the cooled section. If more cooling is required, there are correlations that take into account this entrance region, but they are only valid if you have a minimum of

10 columns. It was therefore decided to do analysis on 4x10 banks of tubes with only the center 4x4 tubes being cooled. Figures 1 and 2 show schematics of the sizing parameters utilized. An overall heat transfer coefficient of 500 W/m^2*k was assumed in all cases.

Although it is understood that the standard correlations may not apply to tubes with a heavy salt coating, we expect that many of the test runs will have a relatively thin salt coating -- ideally no salt layer in the best case -- and thus may be fairly well approximated by the standard correlations.

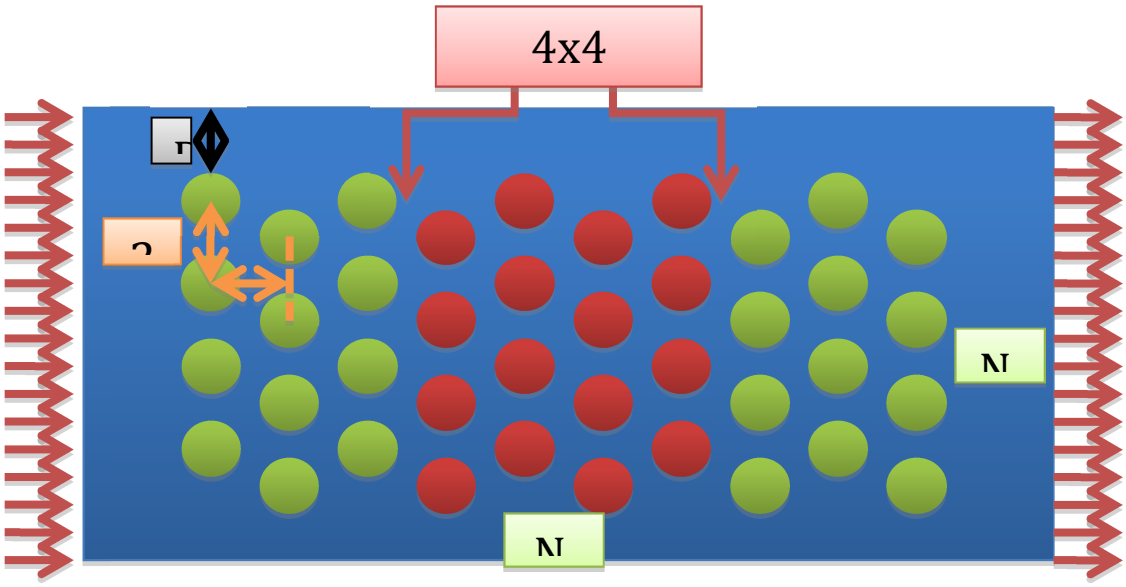

Figure 19: Side View Sizing Schematic

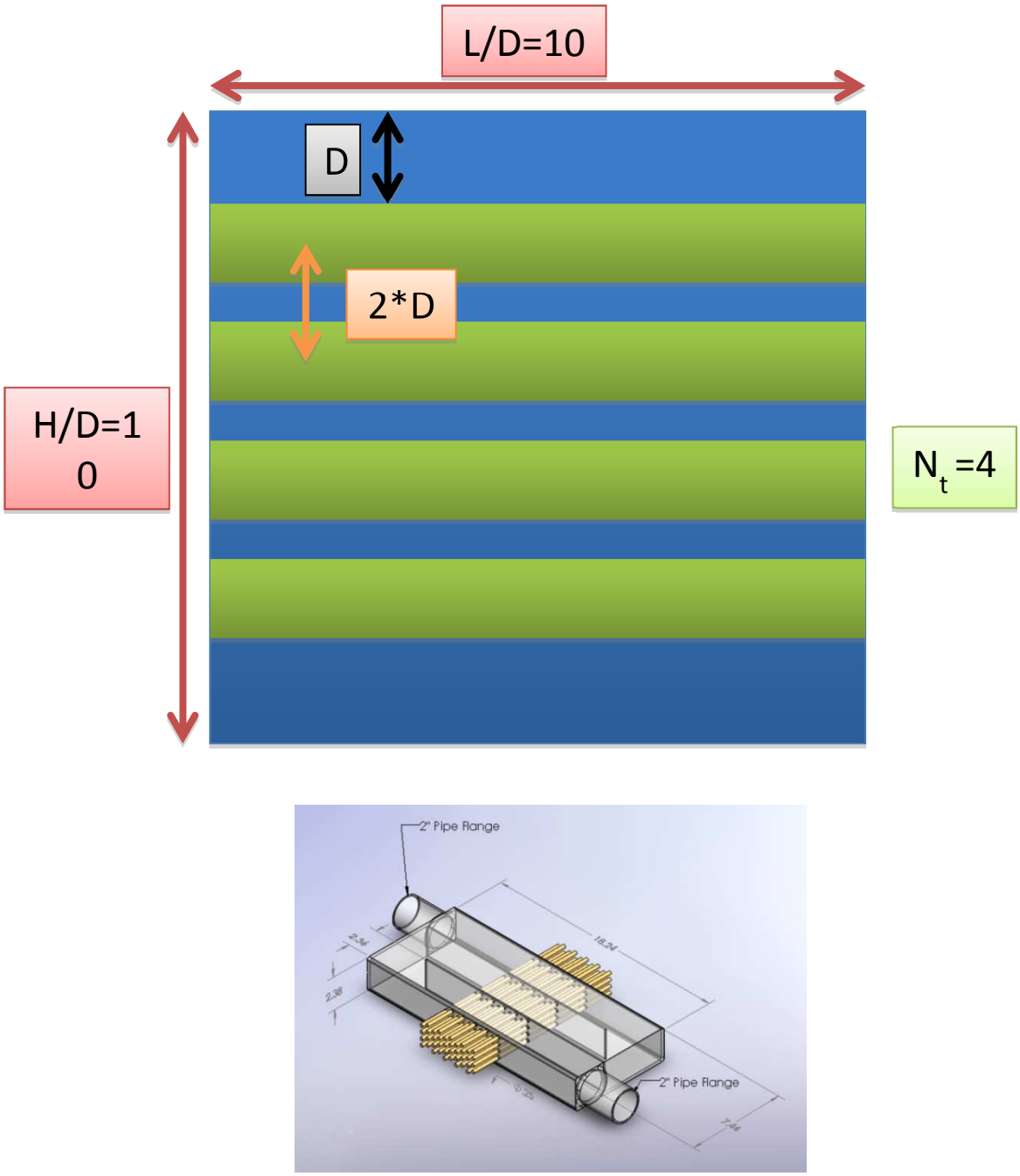

Figure 20: Front View Sizing Schematics and Rendering of Example Heat Exchanger (3 passes shown). In the case of multiple passes, the length allowed for the 180° turns has not been optimized in this schematic.

Salt Flow Analysis

We then went on to analyze the salt flow and heat transfer conditions. A parametric study was performed to study various tube sizes under equivalent dimensionless parameters (Re, Nu, Pr, etc.) The effect of tube size was analyzed versus pressure drop, maximum achievable Reynolds number with current salt pump, change in solid fraction per pass, and overall heat requirement to achieve solid fraction. Plots of all of this analysis can be found in the appendix.

From a pressure drop perspective on the salt side, it was found that a ¼" tube is marginally acceptable with a pressure drop of 12 psi per pass at ReD of 20,000. Larger tube sizes decrease the pressure drop, but increase flow rate requirements. From this perspective it was determined that ½" was the largest tolerable tube size with a maximum ReD of 10,000 with our current pump. If we want Reynolds numbers in the 20,000-30,000 range we will need to get a new pump with either better pressure or flow performance as the ¼" tube barely achieves 20,000 ReD which will most likely be diminished by the large pressure drop.

Solid fractions achievable are fairly small at low delta T and high flow rate. In order to achieve large solid fractions we must do one of 4 strategies.

(i) The first strategy is to use large numbers of passes. This can quickly become impractical however, and in general the number of passes should be kept to a minimum with a maximum of ~5-7.

(ii) The second strategy is to increase delta T. This can be accomplished fairly easily, but produces problems in modeling and solidification conditions.

(iii) The next strategy is to decrease salt flow rate. This decreases the amount of mass that has to be cooled, but also decreases the hydrodynamic forces available to break the salt free from the tube surface, and decreases the salt-side Re_D which is undesirable for reasons of scaling.

(iv) The final strategy would be to rely on increasing the solid fraction a small amount on each pass until the entire system was in slurry form. This would require us to develop a pumpable slurry however that we may not need otherwise.

It must also be taken into account that larger solid fractions require higher heating rates. As tube diameter, and therefore the cross sectional flow area, increases the mass flow rate increases and therefore the more heat it required to achieve the same solid fraction.

Therminol Flow Analysis

On the Therminol side pressure drop was only an issue with 1/8" and smaller diameter tubes. Regarding the flow rate, the smallest pump quoted so far will still perform well in a 4x4 array of 1" tubes. If we decide to cool all 10, we should stay at .5" or smaller in order to maintain a ratio of Therminol convection to overall heat transfer coefficient (h/U) of 10 or greater. Having a high h/U will allow us to better control the wall temperature of the tube, and make it easier to get accurate measurements of the salt side convection coefficient (and solid formation conduction). Temperature rise of the Therminol per pass changes with Reynolds number and tube diameter. The higher the flow rate and the smaller the tube size, the smaller the delta T will be. This creates similar problems to the overall delta T mentioned earlier as well as that the overall delta T will vary as the salt passes over different areas of the tube array which can add error to heat transfer calculations.

Next three different pump curves were obtained from Magnatex Inc. for their three smallest mag-drive high temperature pumps. From the curves the maximum Reynolds number and h/U ratio were calculated. The 1/8" tube produced the highest h/U ratios, but is slightly inefficient in that flow is pressure limited, not flow limited. The ¼" tube and above were flow limited, and with the exception of the 1" tube produced an h/U greater than 10 even for the smallest pump. Below we present more details of the actual design and hardware being installed.

Tank assembly (Solidworks). The brown rectangles are the numerous strip heaters.

Electrical Heaters

One of the lessons from the Phase 1 design was that the heater capacity should be increased significantly, and include immersion heaters as well as external heaters mounted to the outside of the tank and flow sections. This extra heater capacity helps save time when charging and discharging the tank, and allows us to withstand the occasional failure of a few heater elements. Therefore one of the major features of this Phase 2 design is a large amount of heater capacity, exceeding 60 kW, as summarized in the table below.

Type of Heater	Location	Quantity	Capacity (Watts)	Subtotal (Watts
Immersion heaters	Main salt tank	5	1,000	5,000
Strip heaters	Various, mainly tank exterior	42	625	26,250
Strip heaters	Heat exchanger	4	625	2,500
Cartridge heaters	Therminol rig	6	1000	6,000
Tape heaters	Flow sections	4	840	3,360
Band heater	Salt drain	1	2000	2,000
Band heaters	Salt melt tower	8	2300	18,400
Band heaters	Salt melt tower	2	350	700
	TOTALS	72		64,210
		elements		Wattage

Specifying the immersion heaters took considerable time, and we explored various commercial products from companies including Watlow, Tempco, and Hampton Controls. Finally, for reasons of price and availability we elected to have own immersion heaters fabricated based around commercial cartridge heaters using a common specialty machining technique known as gun drilling.

Electrical Infrastructure

Because of the demands of the pump, the desire for large heating capacity described above, and because some of the heaters require 480 V, we had to more than triple the electrical capacity at the experimental working area:

New / Existing	Phase	# of Circuits	Volts	Amps	Watts	
Existing	1	3	240	40	28,800	
Existing	3	1	240	30	7,200	
New	1	4	480	40	76,800	
New	3	1	480	30	14,400	
				TOTAl	127,200	
					Wattage	

This required running new conduit from a CE-CERT transformer to the lab, into a new breaker box and control box, and then on to the experimental station. The previously existing control system was updated to accommodate all of the new heating zones.

Salt Pump

After a time consuming search among possible vendors including Friatech, Lawrence, and Wenesco (lower cost solder pumps), we procured a p ump from Friatech that was specifically designed for molten salts. The pump has salt lubricated bearings and a 20 HP motor. We expect it to provide ~150 GPM at the actual HX head loss. The pump has been installed at CE-CERT and tested with water, and provided over 400 GPM at 60% drive through a test pipe section (not the actual HX).

Friatec Salt Pump. Left: Overview. Right: Detail of flange assembly.

Therminol Pump

The flow loop uses Therminol 66 to on the cold side of the molten salt heat exchanger. The design includes a Therminol reservoir of capacity 55 gallons. The Therminol pump was purchased from Dickow. It is 2 HP with a magnetic drive, and rated to a flowrate of 30 GPM and a maximum temperature of 300 °C. The Therminol pump has been tested successfully.

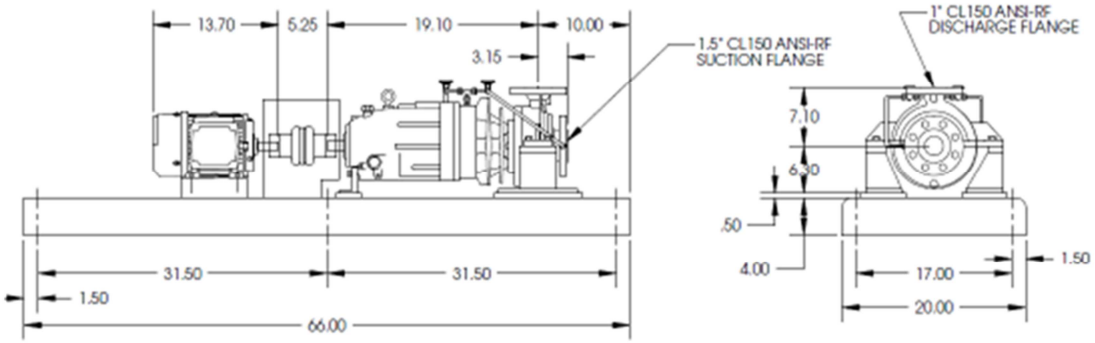

Recommendations and Discussion

From these calculations a tube size of ¼" to ½" is recommended. A ¼" tube size gives a good range of salt Reynolds number, but is limiting on the pressure drop side, and therefore is not recommended for large numbers of passes. A ½" tube size is not nearly as limiting on pressure, but the range of Reynolds number available with our current pump is limited. Therefore from a salt flow perspective, .375" diameter tubes should be optimal. The Therminol flow conditions are adequate over most of the entire size range, so this is not a major factor in the decision.

Table 2: Sizing Calculations Overview

	Tube Diameter	1/8"	¼"	3/8"	1/2"	1"
Salt	Pressure Drop Per Pass (psi)	740	18	8	5	2
	ReDmax at 140 GPM	43000	22000	16000	11000	5500
	ΔSolid Fraction Per Pass @100GPM	0.02	0.04	.06	0.08	0.17
Therminol h/U=10	Pressure Drop Per Pass (psi)	1.2	0.25	.12	0.05	0.01
	GPM	8	20	30	40	80
	ΔT per pass	52	35	34	33	32
Overall	Q (kW)/Pass ΔT=15 (C) ϕ=20%	150	300	450	600	1600
8" Volute 2HP	(Therminol h)/ (Salt-Side U), Max (higher is better)	40	28	22	15	7
10" Volute 2HP		43	33	25	17	9
8" Volute 5HP		49	62	47	31	17

In the end **the heating rate is the largest limiting factor**. Also, there is an important competition between the desire for large change in solid fraction (e.g. input of 5 C superheat and output of 20% solids fraction) and the desire for a high Reynolds number (for reasons of shear stress and scaling similitude). The scientific goals could still largely be studied even in the absence of significant solid fraction. Specifically, for a pure liquid salt and a sub-cooled wall temperature, can we ensure that the solids do NOT nucleate (or build up) on the tube wall? If we do require the high solid fraction, will we rely on pumpable slurry or will we sacrifice Reynolds number? Figure 31 shows how high of a solid fraction we can achieve at Reynolds number for different heating rates for a 0.375" diameter tube. Our system is currently outfitted with approximately 20 kW of heating. We need to decide how much we will need to increase this, taking into account we need heating and cooling on the Therminol loop as well.

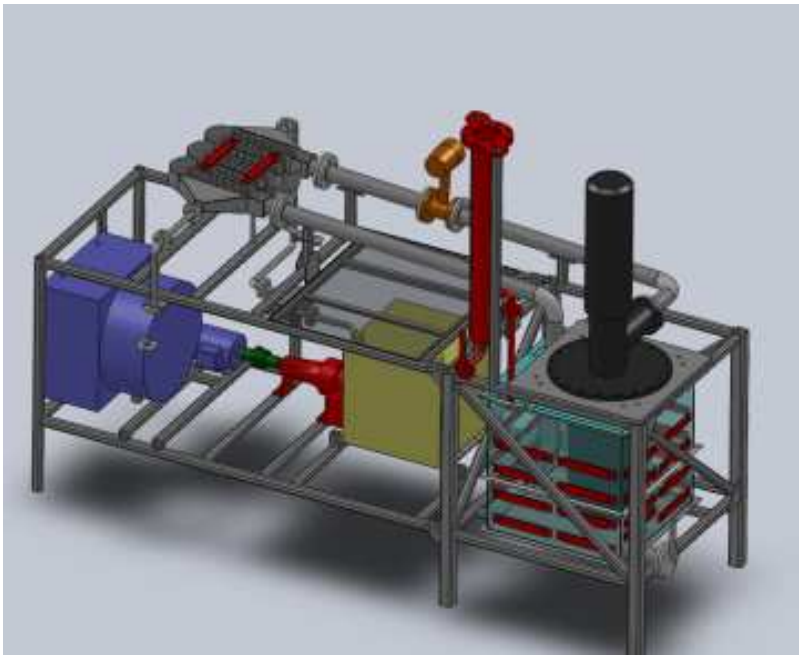

Overview (Solidworks rendering)

Overview (Dec. 2010).

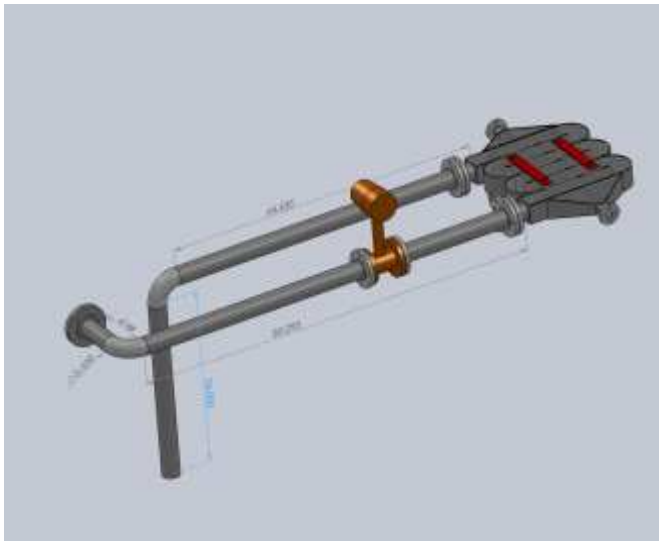

Heat exchanger overview, including inlet and outlet pipe runs and flow meter.

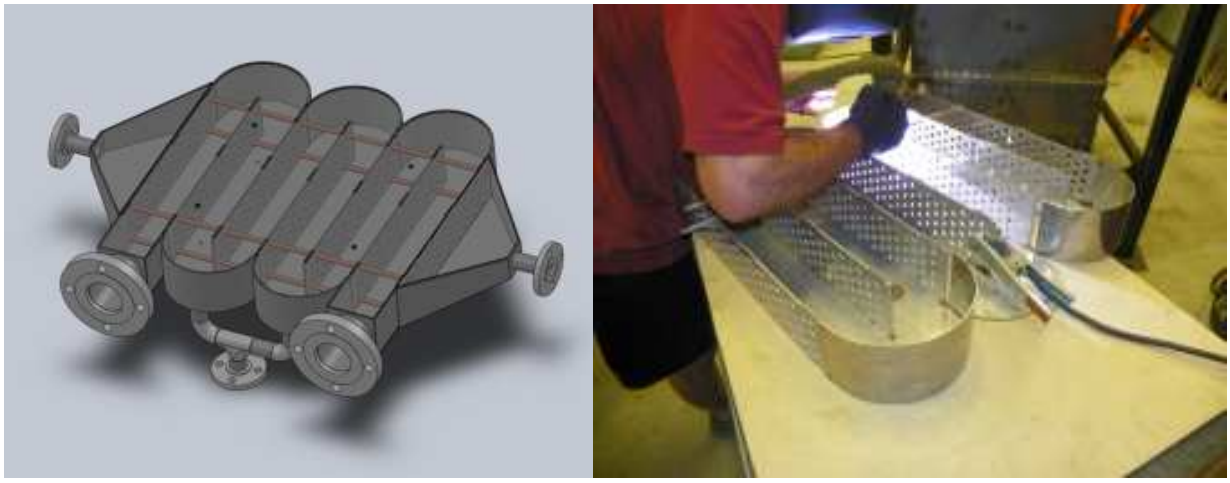

Heat exchanger detail. Left Image: The two large flanges are the inlet and exit for the salt side, which is 6 pass. Only four of the 80 tubes (3/8") are shown (brown cylinders). Right Image: Welding part of the flow section.

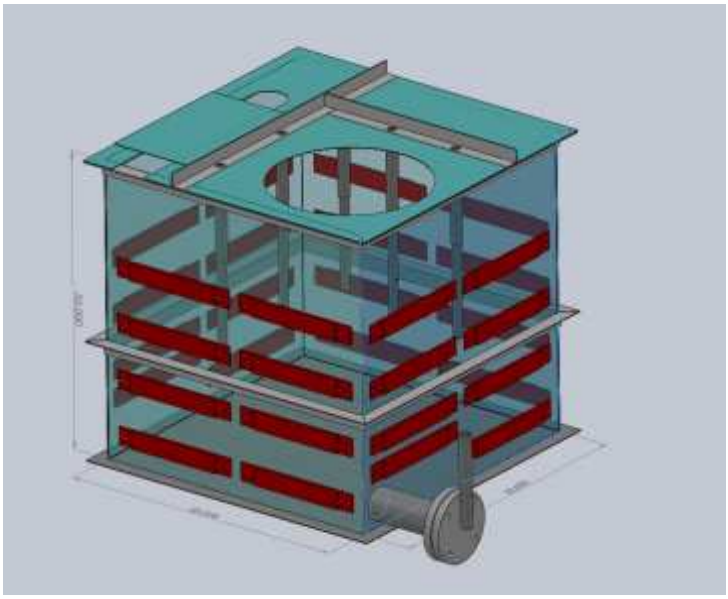

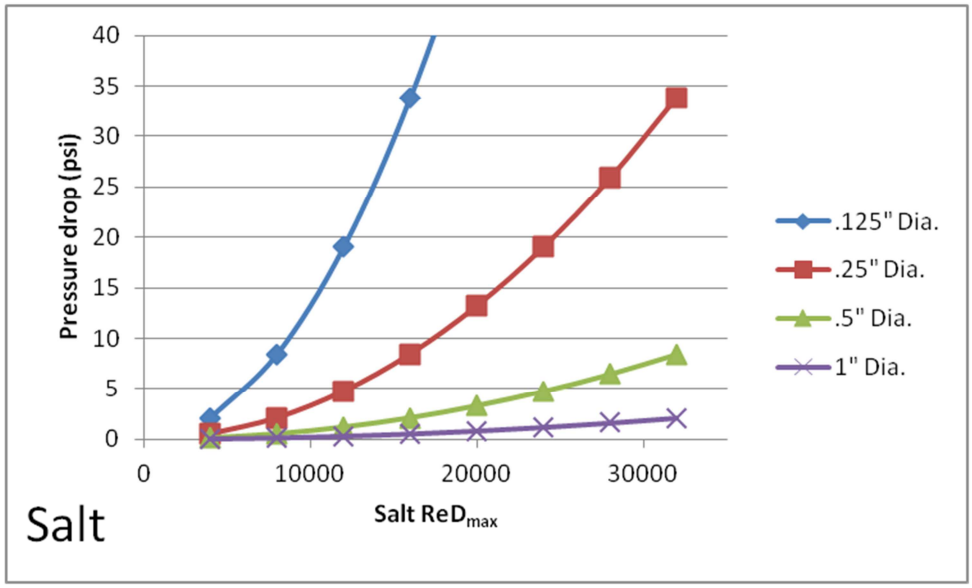

Figure 21: Salt Pressure Drop vs. Reynolds Number

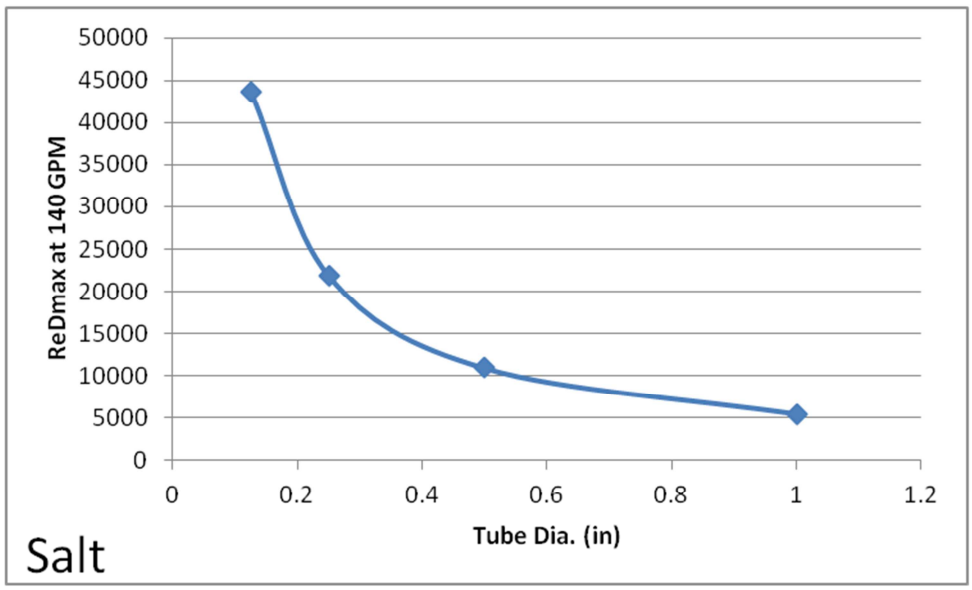

Figure 22: Maximum Salt Side Reynolds Number at Current Pump Maximum Flow Rate vs. Tube Size

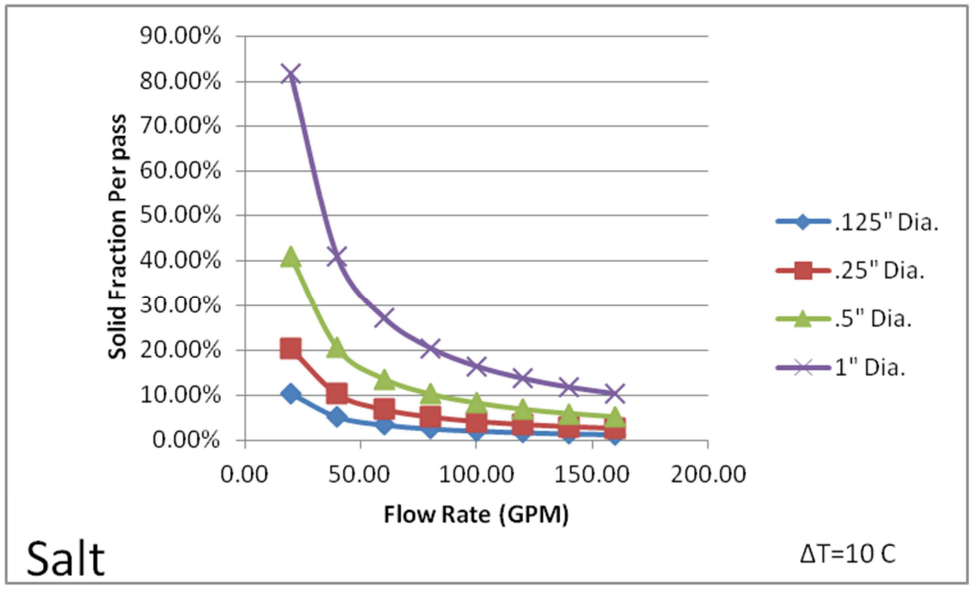

Figure 23: Change in Solid Fraction per Pass vs. Flow Rate and Tube Size

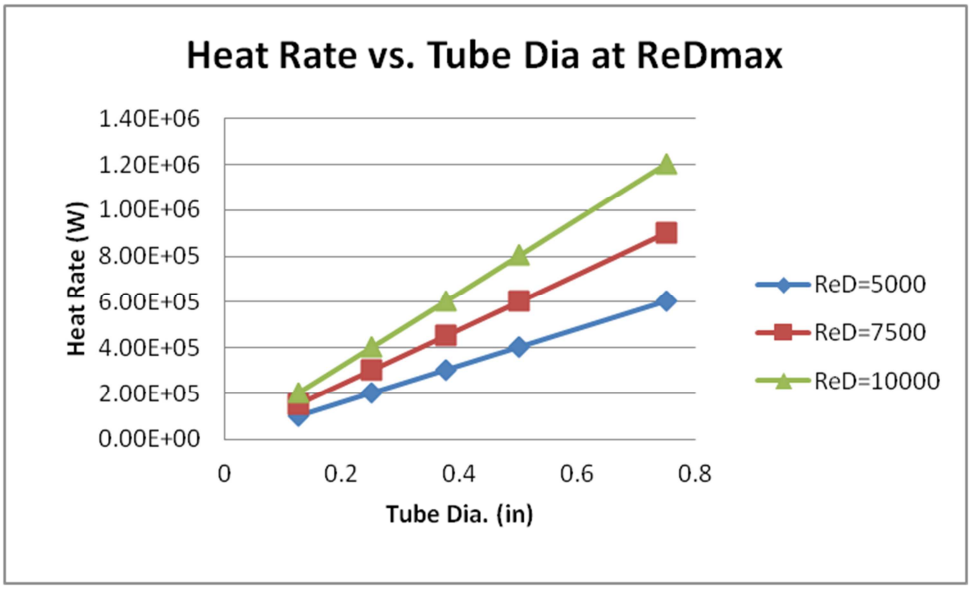

Figure 24: Cooling Rate Required to achieve solid fraction with different tube sizes at different Reynolds numbers

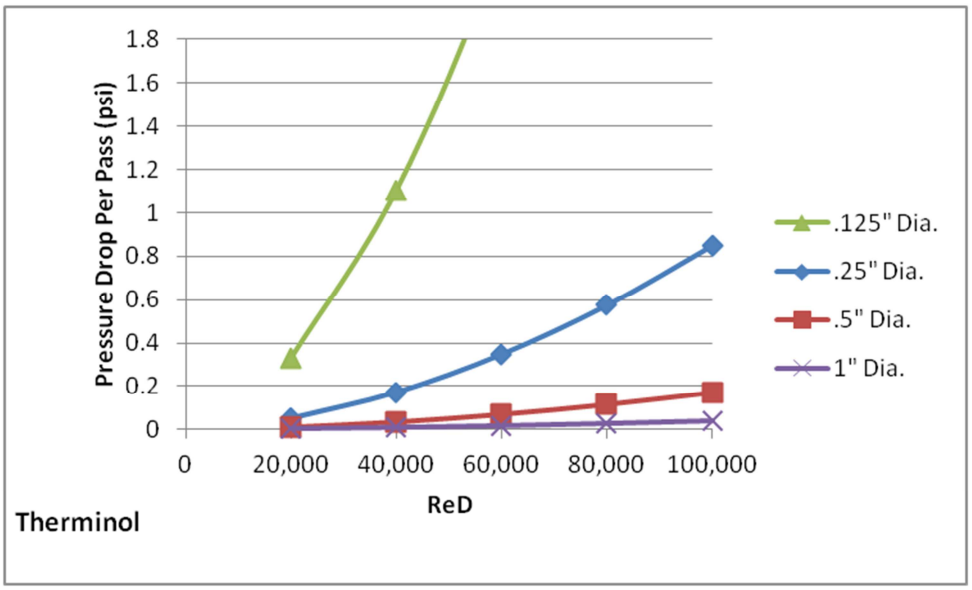

Figure 25: Therminol Pressure Drop Per Pass vs. Reynolds Number and Tube Size

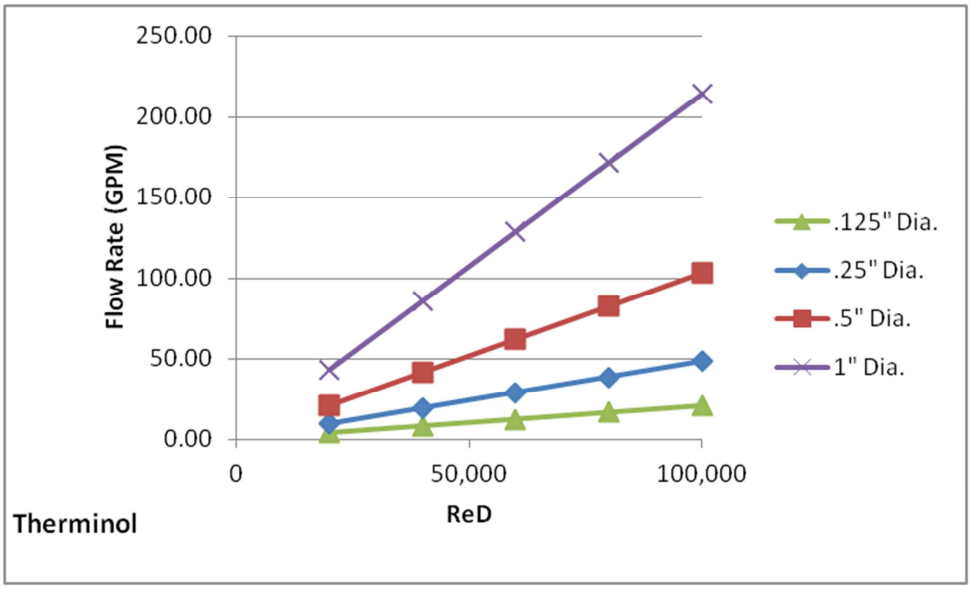

Figure 26: Therminol Flow Rate in GPM vs. Reynolds Number and Tube Size

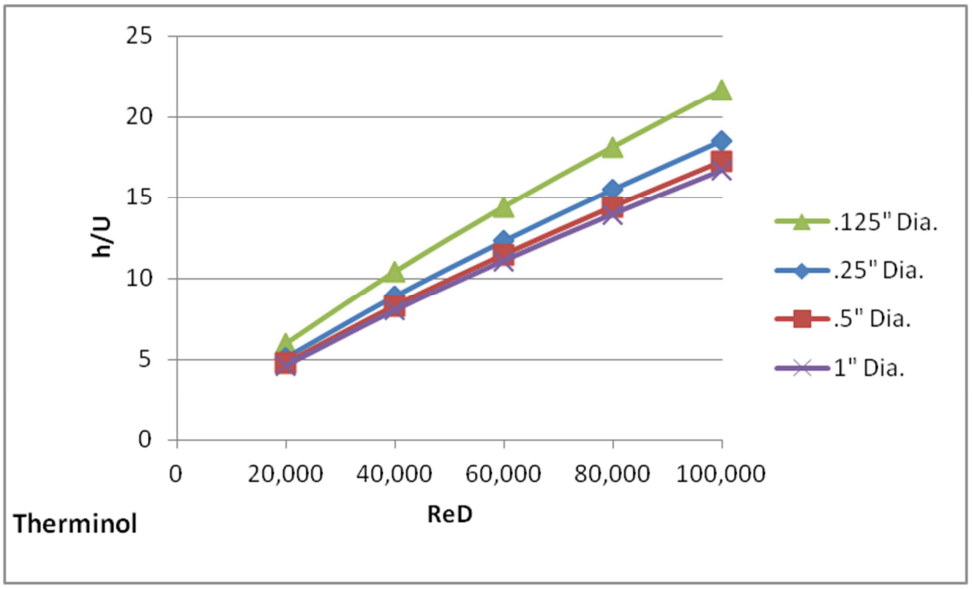

Figure 27: Ratio of Therminol h to Overall U vs. Reynolds Number and Tube Size

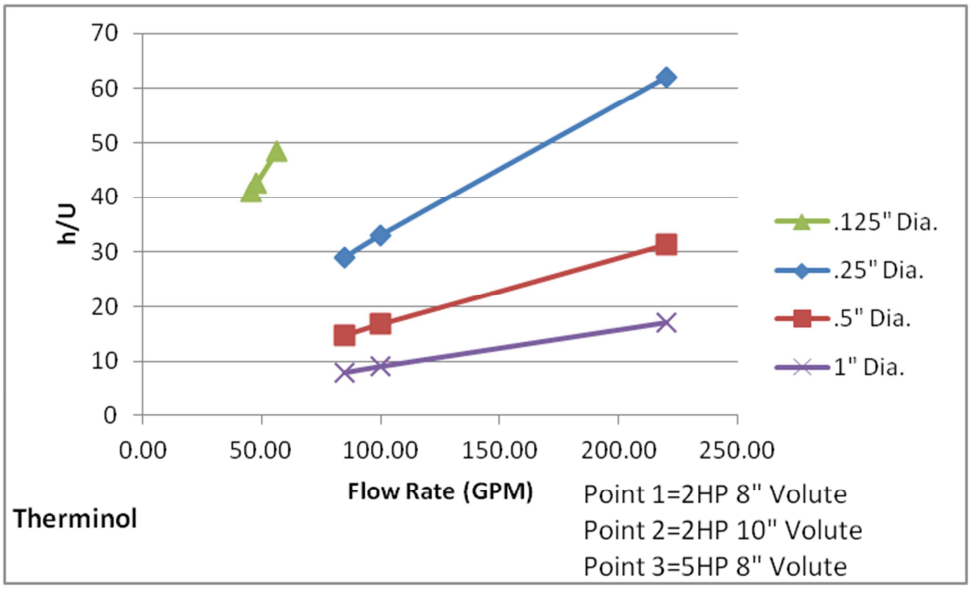

Figure 28: Ratio of Therminol h to Overall U vs. Pump Flow Rate Achievable and Tube Size

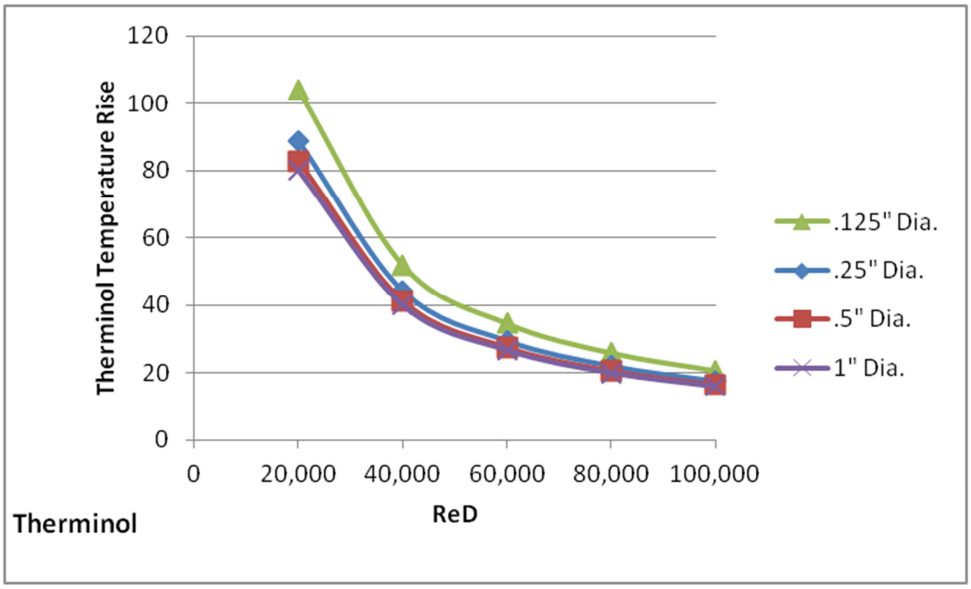

Figure 29: Therminol Temperature Rise per Pass vs. Reynolds Number and Tube Size

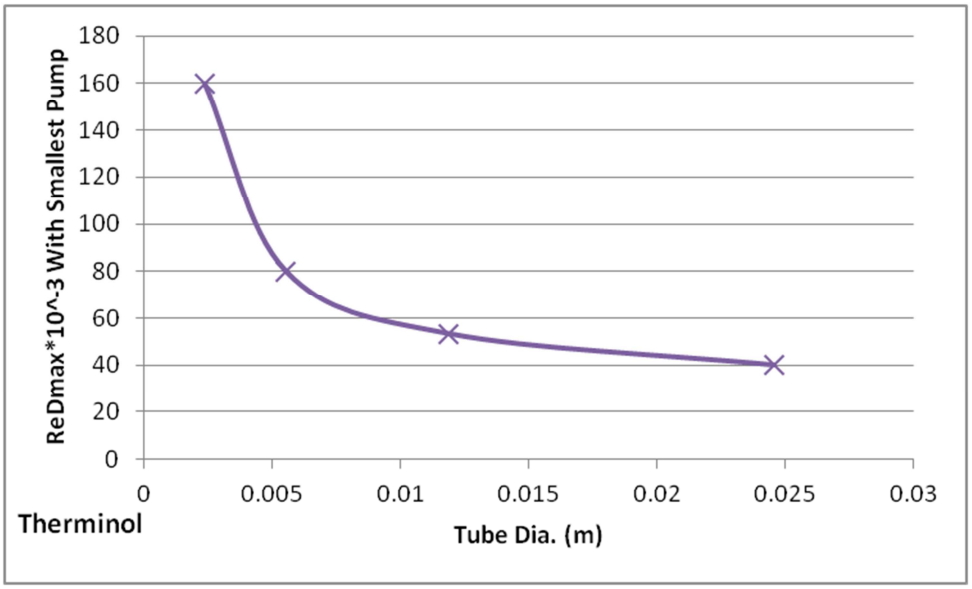

Figure 30: Maximum Reynolds Number Achievable with Smallest Therminol Pump vs. Tube Size

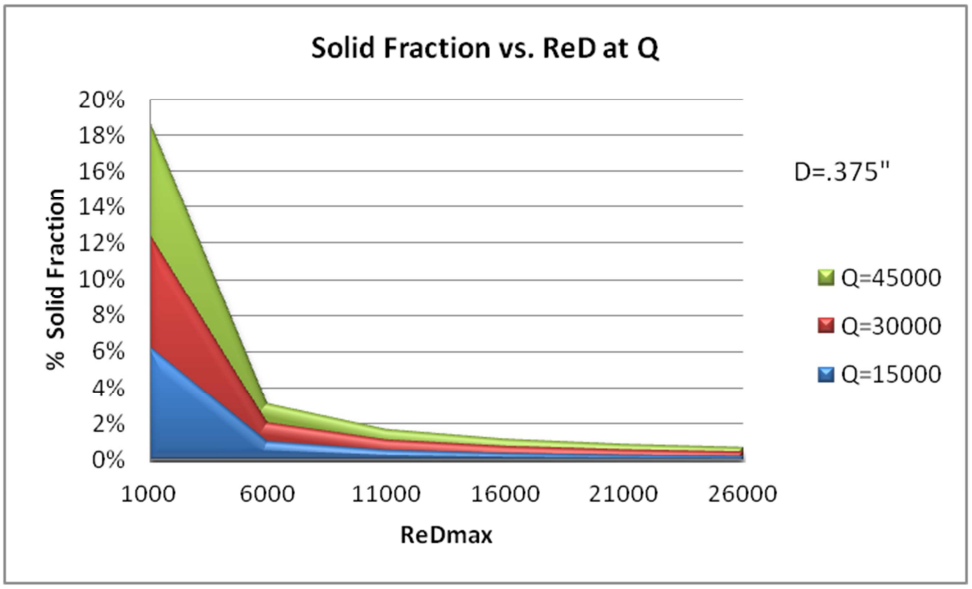

Figure 31: Solid Fraction at Reynolds at Different Heat Rates

Appendix 4.
Experiments with Laboratory Scale Prototype

Expected Outputs

Heat transfer coefficient (Ufreezesalt) as a function ofsolidification at near solification temperature
Heat transfer coefficient (Ufreezesalt) as a function of salt flow and heat transfer temperature difference

Heat transfer coeffieicent correlation from liquid molten salt

Pumpability of freezing mixture
Experience with handling high temperature molten salts near freezing point

Study Parameters	
Temperature of oil	various
Temperature of salt	high, medium, low
Flow rate of salt	high, low
Flow Rate of Oil	high, medium, low

Design of Experiment

Output	Oil Temperature, C	Oil Flow Rate	Salt temperature above freeze point	Salt Flow rate
liq to liq heat transfer coeff	320	high	high	high
liq to liq heat transfer coeff	320	medium	high	high
liq to liq heat transfer coeff	320	low	high	high
liq to liq heat transfer coeff	320	medium	high	low
liq to liq heat transfer coeff	311	low	high	low
solidification heat transfer coeff	311	medium	medium	low
solidification heat transfer coeff	305	medium	medium	low
solidification heat transfer coeff	300	medium	medium	low
solidification heat transfer coeff	280	medium	medium	low
solidification heat transfer coeff	270	medium	medium	low
solidification heat transfer coeff	260	medium	medium	low
solidification heat transfer coeff	260	medium	low	low
solidification heat transfer coeff	250	medium	low	high
solidification heat transfer coeff	250	medium	medium	low
solidification heat transfer coeff	320	medium	high	low
shut down mode	320	medium	heaters off	pump off
shut down mode	fan on	pump off	heaters off	pump off

Label (activity-date)	expt no.	What / Why	How	What should be observed and what data should be recorded Data	Experiment Parameters
Shakedown Tests					
Pre-20110202	1	Melting of Salt	Add using premelter and direct to tank	Time for initial melt of salt. Precautions during adding salt. Note all incidents. Record all temperatures	Salt addition rate. Mixing of salt.
Pre-201102xx	2	Salt Loop fidelity test and pump/ flow characteristics	Salt pump ON. Bypass heat exchanger. Pump salt through the loop; keep all heaters on. Salt temperature should be at least 25C above melting point	Record flow rate, pump speed, salt temperaturesand loop salt temps every 2 minutes. Record visual observations and interpretations in data book	Vary pump speed
Pre-201102xx	3	Salt Loop fidelity test and pump/ flow characteristics	Salt pump ON. Heat exchanger in loop. Pump salt through the loop; keep all heaters on. Salt temperature should be 25C above melting point	Record flow rate, pump speed, salt temperaturesand loop salt temps every 2 minutes. Record visual observations and interpretations in data book	Vary pump speed
Pre-201102xx	4	Therminol loop fidelity tests	Therminol pump ON. By pass heat exchanger.	Test for leaks and flow rate / pressure characteristics without Heat Exchanger	
Pre-201102xx	5	Therminol loop fidelity tests	Therminol pump ON. Salt Pump OFF With heat exchanger.	Test for leaks and flow rate / pressure characteristics without Heat Exchanger	
Pre-201102xx	6	Experiment loop fidelity	Both pumps ON with heat exchanger	Check heat exchanger for leaks or reactions with salt and oil (hope not). Confirm flow rates.	Keep temperatures of salt and therminol same about 350C or greater

Liquid Molten Salt (~350C) Heat Transfer Tests					
LMS-201102xx	7-x	Heat transfer for MOLTEN salt (liquid).		Record flow rates, temperature, pump power, pump speed, all data whatever available every minute. Observation records in excel notebook every 5 minutes.	Fixed salt temperature. pick 3 delta T and four flow rates for salt with therminol at ~90%but constant therminol flow. Vary delta T between therminol and salt temperature starting at expt 6 conditions and gradually reducing Temp. Vary salt flow rates
LMS-201102xx	8-x	Heat transfer for MOLTEN salt (liquid). Repeat 7 with different salt temp		Record flow rates, temperature, pump power, pump speed, all data whatever available every minute. Observation records in excel notebook every 5 minutes.	Approximately fixed salt temperature. pick 3 delta T and four flow rates for salt with therminol at ~90%but constant therminol flow. Vary delta T between therminol and salt temperature starting at expt 6 conditions and gradually reducing Temp. Vary salt flow rates
LMS-201102xx	9	Discover melting temperature	Gradually drop tmperatures everywhere till the salt temperature drops to near melting.	Observe pump flow charactierstics, heat transfer rates (coeff). (note: when you begin to see noticeable change then some freezing may be happening!)	

Appendix 5.
State-of-the-Art Power Tower System Analysis

Simulation Results for a Central Receiver and Energy Storage System

Gyan Hajela,
Pratt & Whitney Rocketdyne (PWR)

In order to properly perform system analyses and to perform trade studies, a computer program is developed to model the central receiver including the field of heliostats, the molten salt cooling loop to transfer energy from the receiver to the thermal storage tank and the phase change circulating loop.

A concentrated solar power (CSP) computer program is used to model the details of the field of heliostats and the central receiver. This includes the size of the field, number and size of heliostats, heliostat optical properties, heliostat locations, location of the field (latitude and longitude), field slope (if any), height of the receiver tower, diameter and the length of the receiver section, etc. This model is used to compute incident power on the receiver as a function of the time of the day and the day of the year.

A molten salt system (MSS) model is used to compute the energy absorbed by the circulating molten salt as it flows through the receiver panels and the energy transferred to the phase change fluid through the sensible heat exchanger, HX-3, and the latent heat exchanger, HX-4. This model will also compute pump power required to circulate the molten salt. The model will also perform detailed thermal, stress and strain calculations to ensure that the receiver panels and tubes can safely sustain the operating conditions.

A thermal storage tank (TST) model is used to perform to compute the energy received from the molten salt loop, energy transferred to the steam generation loop via the super-heater heat exchanger, HX-1, and the vaporizer heat exchanger, HX-2, and the amount of energy stored.

These three models are linked to each other so that their inputs and outputs are properly exchanged. The chained model is run in a time-marching fashion so that the system mass and energy balances can be performed over a period of several hours or days while satisfying load for the steam generator subsystem.

The CSP model can also be used to design the field of heliostats, perform optimization studies to establish critical parameters, such as diameter to length ratio of the receiver, height of receiver tower, heliostat focal lengths, field offset ratio, etc.

The MSS model will also provide parameters that are used design the heat exchangers, fluid pump and the piping system. The CSP and the MSS models are used to develop morning start-up and evening shut down procedures for the molten salt system. The molten salt loop can not circulate through the receiver when the solar incident power is very low or absent. These models will also be used to develop safety procedures in the event of circulating pump failure (to protect receiver tubes from getting too hot) and a cloud cover over the field of heliostats (molten salt freezing in the receiver tubes), etc.

The TST model provides parameters that are used to design heat exchangers (super-heater and the vaporizer), to size the storage tank , and the piping system.

The current scope of this model excludes the water system, though it may be added later on. At this stage the water system are modeled as a thermal load only.

Figure 1 shows the inputs and outputs for these models and how these models interface with each other.

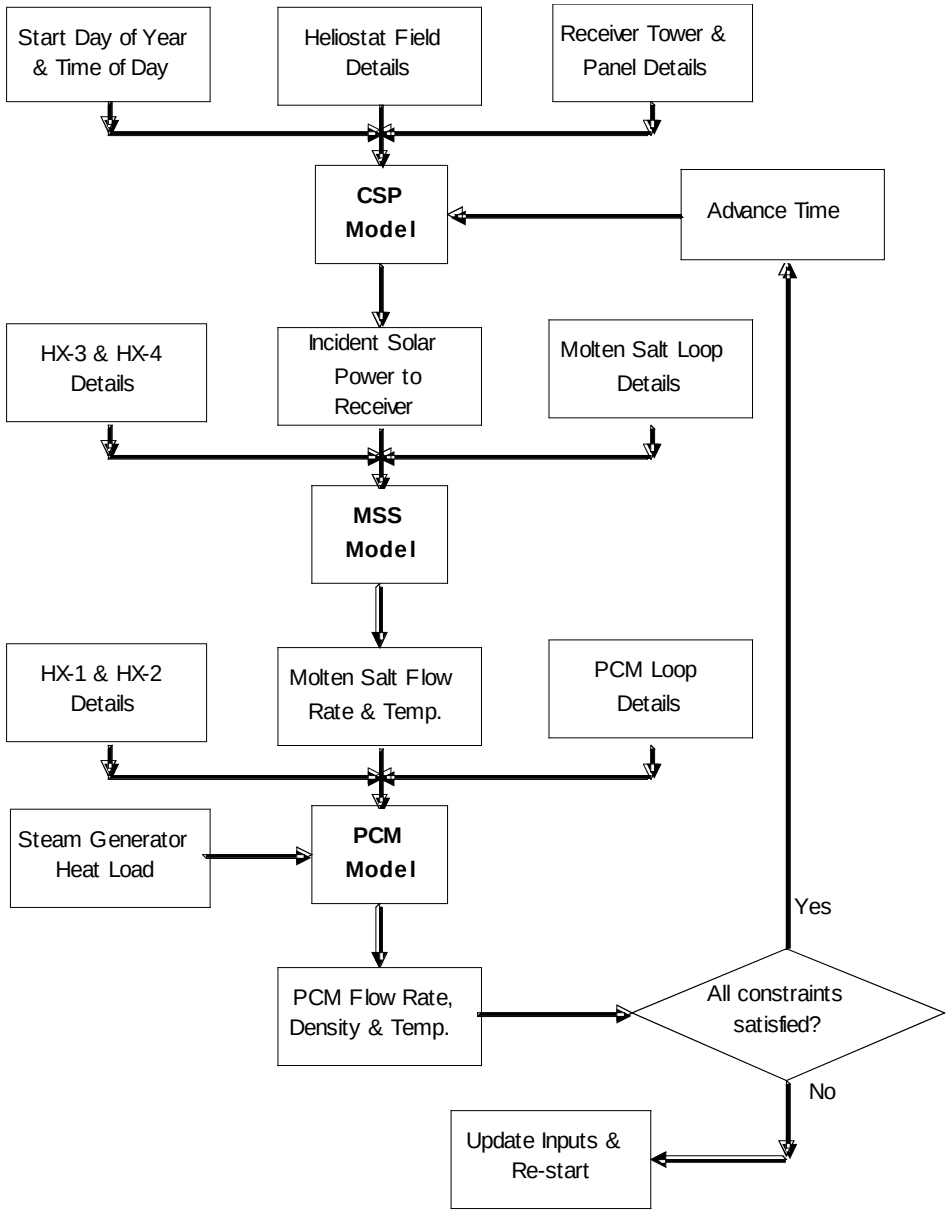

Figure 1. Model Process Diagram

Concentrated Solar Power Model Parameters

To demonstrate the process an existing model was used with the following inputs:

Field of Heliostats:		
Location		Cinco Casas
Latitude, deg	deg	39
Site elevation, km	km	0.65
Atmospheric visibility, km	km	23
Number of heliostats		17,170
Exclusion zone radius, m	m	122
Total land area available (circular field), km^2	sq km	6.3
Number of row of mirrors on heliostat		5
Number of columns of mirrors on heliostat		5
Effective vertical dimension of heliostat, m	m	7.35
Effective horizontal dimension of heliostat, m	m	8.5
Heliostats canted in x-axis		yes
Heliostats canted in y-axis		yes
Heliostat focal lengths, m	m	550, 1050 &
		1500
Average reflectivity of mirror surface		0.92
Standard deviation of the normal error distribution of		
elevation and azimuthal angles, mrad	mrad	1.5
Standard deviation of the normal error distribution of		
reflective surface in horizontal & vertical directions, mrad	mrad	1.5
Standard deviation of the normal error distribution caused		
by wind in horizontal and vertical directions, mrad	mrad	1.5

Receiver Tower:		
Height of the center of receiver above heliostat axis, m	m	175.5
Receiver effective height, m	m	18.3
Receiver effective diameter, m	m	15.1

For the configuration specified above, the solar incident power on the receiver is shown in Figure 2.

For the operation of the molten salt system, the day is the period when the sun elevation is greater than 15 degree above the horizon. Molten salt system flow rate is gradually started, in the morning, as the receiver panels start to heat and is shut down slowly, in the evening, as the incident power starts to drop.

The model can be applied to other site conditions and receiver designs.

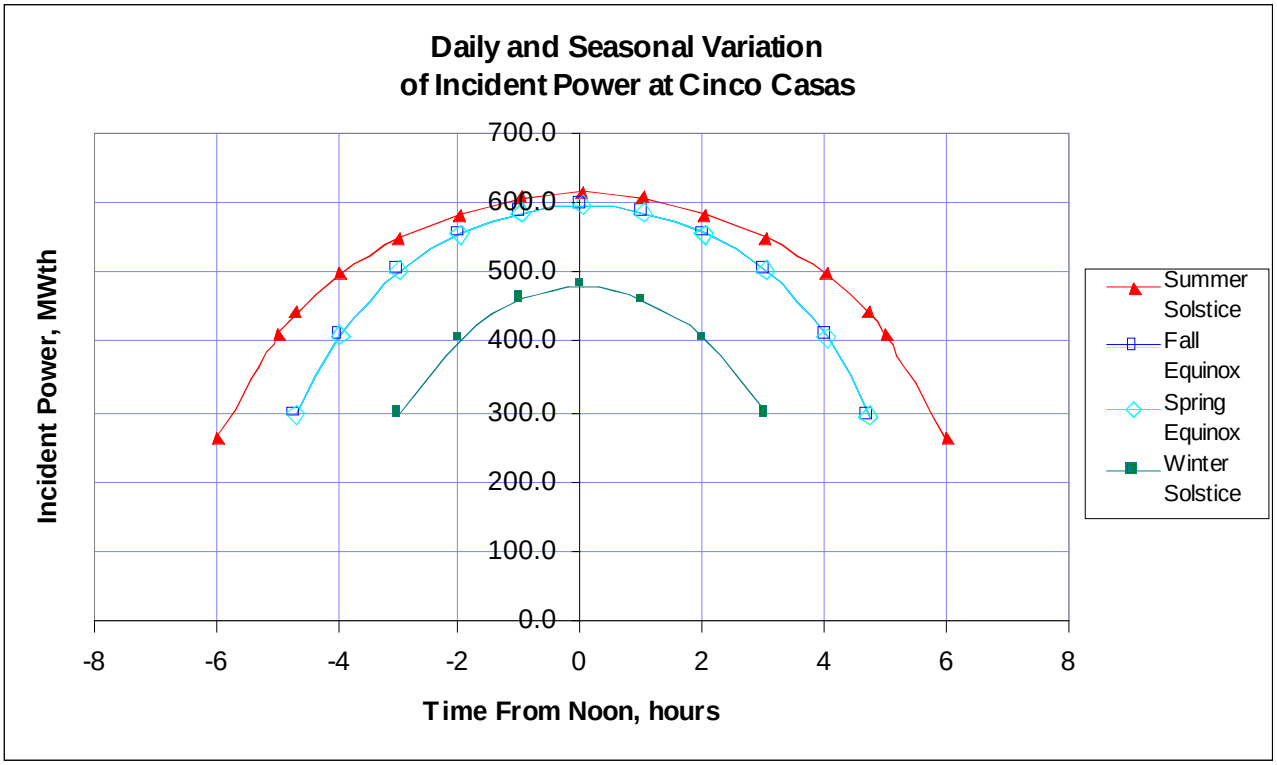

Figure 2. Incident Power Predictions

Heat Transfer Fluid (Low Melting Molten Salt) Subsystem Model Parameters

To demonstrate the process an existing model are used with the following design inputs:

Molten salt composition 60% $NaNO_3$ + 40% KNO_3
Salt temperature at receiver panel inlet, ˚C 288 (550 ˚F)
Salt temperature at receiver panel outlet, ˚C 566 (1050 ˚F)
Number of receiver panels 14
Number of flow circuits in the receiver 2
Panel height, m 18.3 (60 ft)
Panel width, m 3.35 (11 ft)
Ambient temperature around the receiver, ˚C 16 (60 ˚F)
Wind velocity, km/hr 18 (11 mph)
Panel surface reflectivity 0.060
Panel surface emissivity 0.89

For the configuration defined above, the molten salt flow rate is shown in Figure 3.

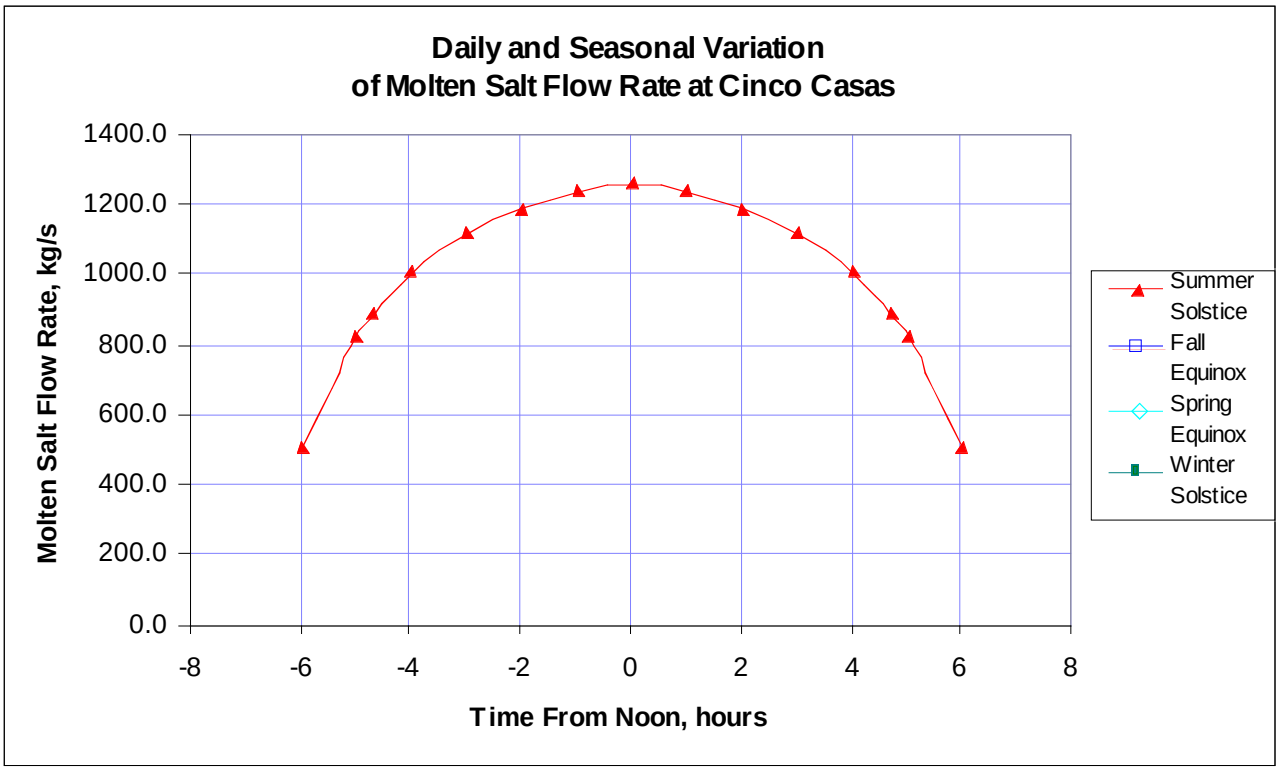

Figure 3. Molten Salt Flow Rate Predictions

Normal Operation

Normal operation is defined as an operation that enables molten salt outlet (from receiver) at the design value (1050 F) and molten salt flow rate greater than 20% of the rated flow rate. Molten salt flow rate can not be maintained at a value below 20% of the rated flow rate. The outlet temperature must be

maintained close to the design value to ensure that the PCM outlet temperature stays close to its design value, which, in turn, is essential to ensure that the superheated steam temperature stays close to its design value.

There are times when the operating conditions do not meet the criteria described above, such as, start-up, shut-down and transient cloud cover. During these conditions the HX-3 is bypassed and the receiver fluid is directed to bottom of tank heat exchanger HX-4 to melt the salt in the tank**.**

Special cases

The models describe above can be used to assess special cases. One such case is described and assessed below. These case provides a model for thermal efficiency as function of outlet temperature.

Case 1. Receiver Thermal Efficiency as a Function of HTF Outlet Temperature

The receiver absorbed the solar flux reflected to the receiver by the field of heliostats. The receiver performance may be defined as:

Receiver Thermal Efficiency = Heat Rate added to HTF molten salt / Incident solar power

Some of the incident solar power is lost by radiation and convection from the receiver panel surfaces. This heat loss is a function of receiver panel surface temperature. The panel surface temperature is directly controlled by the desired molten salt outlet temperature.

The molten salt model is run for a fixed day and time with different molten salt outlet temperatures. For this assessment, the molten salt model is run for the spring equinox (day 81) noon, when the incident power on the receiver was 597 MWth (Figure 4).

The model is run for three molten salt temperatures, 566, 510 and 454 ºC (1050, 950 and 850 ºF). The molten salt inlet temperature was fixed at 288 ºC (550 F). The receiver efficiency vs. molten salt outlet temperature is shown in the table below:

Outlet Temperature		Salt Flow Rate		Receiver
F	C	lb/s	kg/s	Efficiency, %
1050	566	2677	1217	85.9%
950	510	3392	1542	87.0%
850	454	4576	2080	88.0%

As expected, the receiver efficiency is reduced at higher operating temperatures.

Typical Solar Power Tower P/ T / F Fluid Conditions

Solar Thermal Power Plant

Heat Balance Data

#	Description		Case #1	Case #2
-	Ambient Conditions	Ambient DB Temperature (F)	110.0	
-	Ambient Conditions	Ambient WB Temperature (F)	70.0	
-	Ambient Conditions	Ambient WB Pressure (psia)	13.50	
-	System Performance	Gross Power Output (kW)	154,834	
-	System Performance	Aux Loads (kW)	4,966	
-	System Performance	Net Output (kW)	149,868	
-	System Performance	Steam Cycle Efficiency	38.2%	
1	Molten Salt from Hot Tank	Flow (lb/hr)		
		Temp (F)		
		Press (psia)		
		Enthalpy (BTU/lb)		
2	Hot Salt Pump Discharge	Flow (lb/hr)		
		Temp (F)		
		Press (psia)		
		Enthalpy (BTU/lb)		
3	Molten Salt to Superheater	Flow (lb/hr)		
		Temp (F)		
		Press (psia)		
		Enthalpy (BTU/lb)		
4	Molten Salt to Reheater	Flow (lb/hr)		
		Temp (F)		
		Press (psia)		
		Enthalpy (BTU/lb)		
5	Molten Salt from Superheater	Flow (lb/hr)		
		Temp (F)		
		Press (psia)		
		Enthalpy (BTU/lb)		
6	Molten Salt from Reheater	Flow (lb/hr)		
		Temp (F)		
		Press (psia)		
		Enthalpy (BTU/lb)		
7	Molten Salt Supply to Boiler	Flow (lb/hr)		
		Temp (F)		
		Press (psia)		
		Enthalpy (BTU/lb)		
8	Molten Salt to Economizer	Flow (lb/hr)		

		Temp (F)		
		Press (psia)		
		Enthalpy (BTU/lb)		
9	Molten Salt to IP Evaporator	Flow (lb/hr)		
		Temp (F)		
		Press (psia)		
		Enthalpy (BTU/lb)		
10	Molten Salt to Cold Tank	Flow (lb/hr)		
		Temp (F)		
		Press (psia)		
		Enthalpy (BTU/lb)		
11	HP Steam to STG	Flow (lb/hr)	1,093,894	
		Temp (F)	1,000	
		Press (psia)	1,813	
		Enthalpy (BTU/lb)	1,481	
12	CRH from STG	Flow (lb/hr)	1,093,894	
		Temp (F)	716	
		Press (psia)	590	
		Enthalpy (BTU/lb)	1,361	
13	CRH to Reheater	Flow (lb/hr)	1,093,894	
		Temp (F)	716	
		Press (psia)	590	
		Enthalpy (BTU/lb)	1,361	
14	HRH to STG	Flow (lb/hr)	1,093,894	
		Temp (F)	1,000	
		Press (psia)	578	
		Enthalpy (BTU/lb)	1,519	
15	IPT to LPT	Flow (lb/hr)	912,826	
		Temp (F)	558	
		Press (psia)	96	
		Enthalpy (BTU/lb)	1,309	
16	STG Exhaust	Flow (lb/hr)	810,715	
		Temp (F)	141	
		Press (psia)	3	
		Enthalpy (BTU/lb)	1,081	
17	Condenser Hotwell	Flow (lb/hr)	810,715	
		Temp (F)	135	
		Press (psia)	3	
		Enthalpy (BTU/lb)	103	
18	Condensate Pump Discharge to FWH1	Flow (lb/hr)	810,715	
		Temp (F)	135	
		Press (psia)	35	
		Enthalpy (BTU/lb)	103	
19	Condensate to FWH2	Flow (lb/hr)	864,850	
		Temp (F)	186	
		Press (psia)	35	

		Enthalpy (BTU/lb)	154	
20	Condensate to Deaerator	Flow (lb/hr)	864,850	
		Temp (F)	200	
		Press (psia)	34	
		Enthalpy (BTU/lb)	168	
21	Boiler Feed Pump Suction	Flow (lb/hr)	1,093,894	
		Temp (F)	257	
		Press (psia)	34	
		Enthalpy (BTU/lb)	226	
22	Feedwater to FWH3	Flow (lb/hr)	1,093,894	
		Temp (F)	261.1	
		Press (psia)	1,965.6	
		Enthalpy (BTU/lb)	233.9	
23	Feedwater to FWH4	Flow (lb/hr)	1,093,894	
		Temp (F)	351.5	
		Press (psia)	1,926.3	
		Enthalpy (BTU/lb)	326.1	
24	Feedwater to Economizer	Flow (lb/hr)	1,093,894	
		Temp (F)	446.3	
		Press (psia)	1,887.8	
		Enthalpy (BTU/lb)	427.0	
25	Economizer to Steam Drum	Flow (lb/hr)	1,093,894	
		Temp (F)	604.9	
		Press (psia)	1,850.0	
		Enthalpy (BTU/lb)	622.4	
26	Steam Drum to Recirc Pump	Flow (lb/hr)	1,455,649	
		Temp (F)	624.9	
		Press (psia)	1,850.0	
		Enthalpy (BTU/lb)	654.2	
27	Recirc Pump to Boiler	Flow (lb/hr)	1,455,649	
		Temp (F)	625.9	
		Press (psia)	1,887.8	
		Enthalpy (BTU/lb)	655.5	
28	Boiler to Steam Drum	Flow (lb/hr)	1,455,649	
		Temp (F)	624.9	
		Press (psia)	1,850.0	
		Enthalpy (BTU/lb)	1,048.7	
29	HP Steam to Superheater	Flow (lb/hr)	1,093,894	
		Temp (F)	624.9	
		Press (psia)	1,850.0	
		Enthalpy (BTU/lb)	1,147.3	
30	Feedwater to Throttle Valve	Flow (lb/hr)	0	
		Temp (F)	261.1	
		Press (psia)	1,965.6	
		Enthalpy (BTU/lb)	233.9	

31	Feedwater to IP Evaporator	Flow (lb/hr)	0	
		Temp (F)	263.9	
		Press (psia)	590.3	
		Enthalpy (BTU/lb)	233.9	
32	IP Steam to Reheater	Flow (lb/hr)	0	
		Temp (F)	263.9	
		Press (psia)	590.3	
		Enthalpy (BTU/lb)	233.9	
33	IP Extraction Steam to FWH4	Flow (lb/hr)	97,382	
		Temp (F)	913.6	
		Press (psia)	415.0	
		Enthalpy (BTU/lb)	1,477.1	
34	IP Extraction Steam to FWH3	Flow (lb/hr)	83,686	
		Temp (F)	642.0	
		Press (psia)	140.0	
		Enthalpy (BTU/lb)	1,347.9	
35	LP Extraction Steam to Deaerator	Flow (lb/hr)	47,976	
		Temp (F)	366.5	
		Press (psia)	34.6	
		Enthalpy (BTU/lb)	1,221.0	
36	LP Steam Extraction to FWH2	Flow (lb/hr)	11,658	
		Temp (F)	311.5	
		Press (psia)	25.0	
		Enthalpy (BTU/lb)	1,196.0	
37	LP Steam Extraction to FWH1	Flow (lb/hr)	42,477	
		Temp (F)	195.5	
		Press (psia)	10.5	
		Enthalpy (BTU/lb)	1,136.9	
38	Drain from FWH4	Flow (lb/hr)	97,382	
		Temp (F)	360.5	
		Press (psia)	406.7	
		Enthalpy (BTU/lb)	333.2	
39	Drain from FWH3	Flow (lb/hr)	181,068	
		Temp (F)	270.1	
		Press (psia)	137.2	
		Enthalpy (BTU/lb)	239.3	
40	Drain from FWH2	Flow (lb/hr)	11,658	
		Temp (F)	195.1	
		Press (psia)	11.5	
		Enthalpy (BTU/lb)	163.2	
41	Drain from FWH1	Flow (lb/hr)	54,135	
		Temp (F)	144.1	
		Press (psia)	10.3	
		Enthalpy (BTU/lb)	112.0	
42	FWH1 Drain Pump Discharge	Flow (lb/hr)	54,135	

		Temp (F)	144.1	
		Press (psia)	34.5	
		Enthalpy (BTU/lb)	112.1	
43	Cooling Water to Condensor	Flow (lb/hr)	39,748,338	
		Temp (F)	116.3	
		Press (psia)	25.0	
		Enthalpy (BTU/lb)	84.4	
44	Cooling Water to Cooling Tower	Flow (lb/hr)	39,748,338	
		Temp (F)	136.3	
		Press (psia)	15.1	
		Enthalpy (BTU/lb)	104.4	
45	Cooling Water to Cooling Water Pump	Flow (lb/hr)	39,748,338	
		Temp (F)	116.3	
		Press (psia)	14.8	
		Enthalpy (BTU/lb)	84.4	